POLITECNICO DI MILANO
Department of Chemistry, Materials and Chemical Engineering "Giulio Natta"
Doctoral Program in Materials Engineering

Characterization of Cs-Sb cathodes for high charge RF photoinjectors

Doctoral Dissertation of:
Irene Martini

Supervisor:
Dr. Christoph Hessler (CERN)

Tutor:
Prof. Marco Beghi (Politecnico di Milano)

The Chair of the Doctoral Program:
Prof. Chiara Castiglioni (Politecnico di Milano)

Year 2015 - Cycle XXVIII

"Dans la vie, rien n'est á craindre, tout est á comprendre."
(Marie Sklodovska Curie)

Abstract

Future accelerators such as CLIC (Compact LInear Collider), require high brightness electron beams that could be produced with a photoinjector (laser-driven electron source). Cs_2Te photocathodes in combination with ultra-violet (UV) laser beams are currently used in many photoinjector facilities, but requirements to the electron sources for future accelerators like CLIC are more demanding. The main challenge for the CLIC drive beam photoinjector is to achieve high bunch charges (8.4 nC), high bunch repetition rates (500 MHz) within long trains (140 μs) and with sufficiently long cathode lifetimes. In particular the laser pulse energy in UV, for such long pulse trains, is currently limited due to a degradation of the beam quality during the 4^{th} harmonic frequency conversion process. Using the 2^{nd} harmonic (green laser beam), provided it is matched with a low photoemission threshold photocathode material, would overcome this limitation. Cesium antimonide (Cs_3Sb), being a photoemissive material in the visible range, could be a good candidate for this purpose.

The main goal of this PhD thesis is to provide a comprehensive experimental investigation of the use of this delicate material for photoinjector applications. The experimental activities, devoted to asses the feasibility of producing high quality Cs_3Sb cathodes, include production by thin film deposition and characterization of the photoemissive properties in a DC gun beam line. The performance of Cs-Sb photocathodes was tested in a high charge RF photoinjector setup allowing to measure their main features. X-ray photoelectron spectroscopy analyses were used to correlate the measured photoemissive properties with the cathode composition as well as to investigate the cathode deterioration observed during operation. A close comparison with the Cs_2Te cathodes performance is also discussed.

This study represents a step forward in the development of photocathodes for applications in high charge RF photoinjectors, providing a valuable characterization of the Cs-Sb photocathode performance.

Abstract

Acceleratori di particelle di nuova generazione, come CLIC (Compact LInear Collider), necessitano di fasci di elettroni ad elevata brillanza che potrebbero essere generati attraverso l'uso di un fotoiniettore (sorgente di fotoelettroni attivata da un fascio laser). Fotocatodi di Cs_2Te illuminati con fasci laser nell'ultravioletto (UV) sono attualmente utilizzati in diversi fotoiniettori, ma le specifiche tecniche delle sorgenti di elettroni per acceleratori innovativi come CLIC sono significativamente piú difficili da realizzare. In particolare, il requisito piú stringente per il *drive beam* di CLIC é quello di riuscire ad ottenere allo stesso tempo impulsi di elettroni ad elevata carica (8.4 nC) ed alta frequenza di ripetizione (500 MHz), treni di impulsi di lunga durata (140 μs) e fotocatodi con una vita utile ragionevolmente estesa. In particolare l'energia del treno di impulsi laser nel UV, per una tale estesione temporale, é al momento limitata a causa del deterioramento del fascio laser durante il processo di generazione di quarta armonica. L'utilizzo della seconda armonica (fascio laser nel verde), a condizione che questa sia accoppiata ad un fotocatodo con una soglia di fotoemissione bassa, rappresenterebbe una soluzione a questa limitazione. L'antimoniuro di Cesio (Cs_3Sb), essendo un materiale con buone proprietá fotoemissive nelle lunghezze d'onda del visibile, risulta essere un materiale di interesse in questo ambito.

L'obiettivo principale di questa tesi di dottorato é quello di fornire uno studio sperimentale approfondito dell'uso di tale materiale per applicazioni in fotoiniettori. Le attivitá sperimentali volte a studiare la possibilitá di produrre catodi Cs_3Sb di elevata qualitá, comprendono la produzione, attraverso tecniche di deposizione di film sottili, e la caratterizzazione delle proprietá fotoemissive in una linea di accelerazione DC. Le prestazioni dei fotocatodi di Cs-Sb sono state studiate all'interno di un fotoiniettore a radio

frequenza, permettendo cosí di caratterizzarne le funzionalitá piú rilevanti per queste applicazioni. Analisi di spettroscopia di fotoemissione a raggi x (XPS) sono state svolte per correlare le proprietá fotoemissive osservate alla composizione chimica dei fotocatodi e per studiare i processi di deterioramento del catodo, a cui esso é soggetto durante il funzionamento del fotoiniettore. Inoltre, é stato condotto un confronto con le prestazioni raggiunte da catodi di Cs_2Te.

Questo lavoro di tesi fornisce una dettagliata caratterizzazione delle prestazioni di fotocatodi in Cs-Sb e rappresenta perció un importante contributo allo sviluppo di fotocatodi per applicazioni in fotoiniettori a radiofrequenza ed elevata carica.

Contents

Chapter 1

Introduction

1.1 CLIC at CERN

CLIC (Compact LInear Collider) is a study project, conducted by an a international collaboration (1), for a future electron-positron room temperature linear collider. This collider is conceived for a fine characterization of the LHC (Large Hadron Collider (2)) discoveries. CLIC is designed to be built in stages of increasing collision energy: starting from 360 GeV, increasing to around 1.4 TeV, and up to a final energy of 3 TeV. Colliding electrons with their anti-matter partners, i.e. positrons, at such extreme energies will give an insight into fundamental physics beyond that available from LHC or the low-energies colliders. At these high energies, however, electrons and positrons would lose a huge fraction of their energy by emission of synchrotron radiation in a circular collider like the LHC. One possible solution is to accelerate the particles in two linear accelerators facing each other as shown in Fig. 1.1.

In order to reach a collision energy of 3 TeV in a realistic and cost efficient scenario in a linear collider, the accelerating gradient has to be very high. CLIC aims at an acceleration gradient of 100 MV/m, 20 times higher than the LHC (2) and 3 times higher than ILC (International Linear Collider (4)), which is based on superconducting technology. Assuming such accelerating gradient, the estimated length of each linac is about 21 km. Such high gradient can be achieved only for high frequency accelerating cavities (12 GHz). One way to generate this high frequency is the dedicated two beam accelerations scheme sketched in Fig. 1.2: a drive beam (high current and low energy) is conceived to supply the main beam (high energy and low current) accelerating

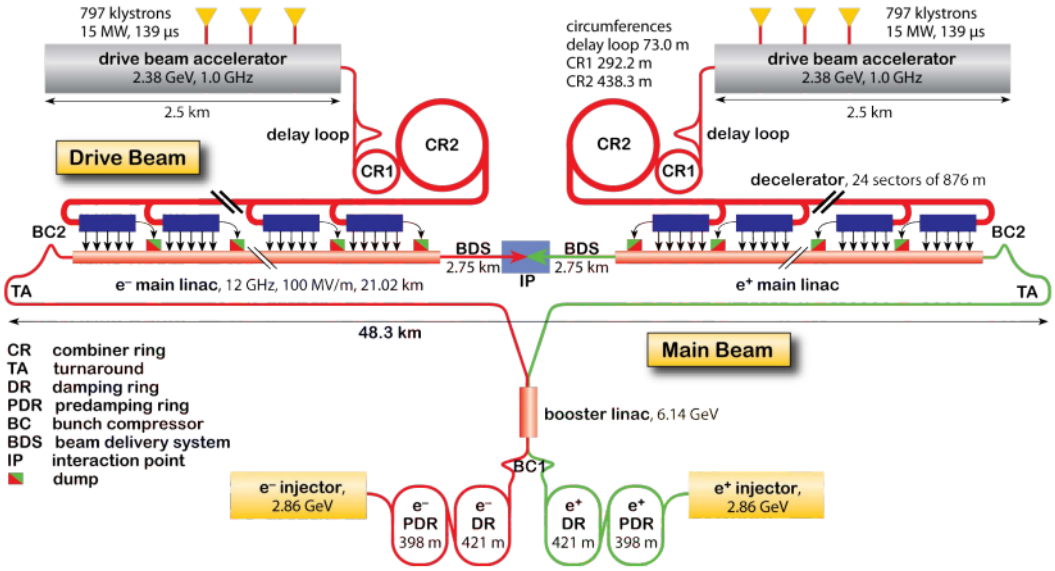

Figure 1.1: CLIC layout (3).

structures with the RF (Radio Frequency) power. Initially, long electron pulse train with 500 MHz bunch repetition rate are accelerated in the 1 GHz normal-conducting drive beam linac. Subsequently, the pulse trains are transformed to shorter trains with the desired 12 GHz time structure by interleaving segments of the trains with each other in a delay loop and two combiner rings. The drive beam is then decelerated in the power extraction and transfer structures (PETS) and thereby the generated RF power is transferred to the accelerating structures of the main beam (more details can be found elsewhere (3)).

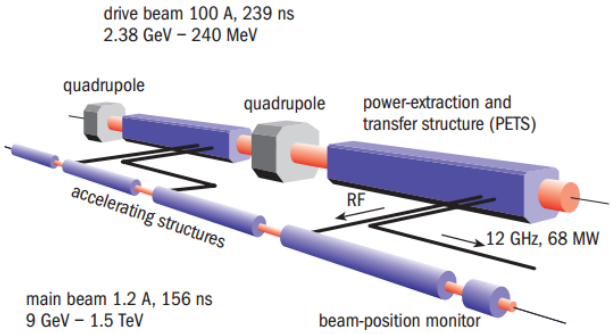

Figure 1.2: The CLIC two beams accelerating method (3).

The CLIC Test Facility was built at CERN to develop and test the technology for CLIC. The CTF3 (CLIC Test Facility 3) has successfully demonstrated the production of the CLIC RF power and the two-beam acceleration up to a gradient of 145 MV/m, as documented in the CLIC Design Report (3).

The drive beam of CTF3 is currently produced using a thermionic gun and a sub-harmonic bunching system, which creates the required time structure for the CTF3 beam combination (5). However this solution generates parasitic satellite bunches, which can cause beam losses and radiation issues.

The high charge RF PHIN photoinjector (more details in Chap. 4) has been originally developed at CERN as an alternative option to the thermionic gun setup for CTF3. Practically satellite-free beam production with the required time structure has been demonstrated at PHIN using a laser based phase coding (6).

The PHIN photoinjector is now being used, as an off-line test stand at CTF3, to perform feasibility studies of a laser driven electron source for the CLIC drive beam.

1.2 Drive beam photoinjector and photocathodes

The CLIC drive beam parameters are very demanding, as shown in Table 1.1. In particular the combination of a high bunch charge of 8.4 nC, 2 ns bunch spacing, 140 μm long pulse trains and 50 Hz macro-pulse repetition rate is beyond any existing photoinjector. This set of parameters is challenging for the cathode and also for the laser setup.

To deliver high-charge picosecond electron bunches the RF photoinjector requires appropriate trains of picosecond laser pulses synchronized with the driving RF pulse in the photoinjector cavity. Assuming a cathode quantum efficiency (QE) of $\sim 2\%$, the laser setup must deliver 2 μJ/pulse, which corresponds to 1 kW of mean power within the train and 7 W average UV power for a train repetition rate of 50 Hz. Moreover, train envelope decay or distortion should be minimized, i.e. the bunch-to-bunch and train-to-train fluctuations in terms of energy and beam quality must not exceed 0.1%. The PHIN photoinjector laser system (7) consists of a commercial passively mode-locked Nd:YLF oscillator synchronized with the 1.5 GHz RF reference signal, a preamplifier, two diode pumped Nd:YLF amplifier stages and frequency conversion stages for green (2^{nd} harmonic) and UV generation (4^{th} harmonic).

Table 1.1: The CLIC drive beam design parameters and the PHIN photoinjector nominal parameters

Parameter	**CLIC**	**PHIN**
Charge/bunch [nC]	8.4	2.3
Bunch length [ps]	10	10
Bunch spacing [ns]	2	0.66
Bunch rep. rate [GHz]	0.5	1.5
Number of bunches	70000	1800
Train length [μs]	140	1.2
Macro-pulse rep. rate [Hz]	50	5
Charge/train [μC]	590	4.1
Beam current/train [A]	4.2	3.4
Charge stability	<0.1%	<0.25%
Cathode lifetime [h] QE>3% (Cs_2Te) QE>0.5% (Cs_3Sb)	>150	>50
Norm. emittance [μm]	<100	<25

The feasibility of high average power and long train UV beam production by 4^{th} harmonic generation was investigated with this laser system (8). During the fourth harmonic generation, an accumulation of partly recoverable UV two-photons induced optical defects in a BBO (Beta Barium Borate) crystal has been observed during the 140 μs train, even for a relatively low peak pulse power of about 100 MW/cm^2. The accumulated defects lead to linear absorption of green and UV co-propagating pulses and since the train consists of about 70000 pulses and the decay time of induced defects is greater than the train duration, a degradation of the UV beam and train envelope was observed. Since the 2^{nd} harmonic conversion process to produce green light is not affected by this problem (8), a potential solution is to use photocathodes with a reasonable QE in the green light wavelength range, such as Cs_3Sb, instead of Cs_2Te cathodes.

This PhD work is devoted to the studies of Cs-Sb cathodes for high charge RF photoinjector applications, in particular for the CLIC drive beam photoinjector. In Chap. 2 the main photocathode features are listed and an overview on different photocathode materials used in photoinjectors facilities is given. In Chap. 3 the CERN cathodes

preparation chamber and the production process are presented in detail together with the photocathodes photoemissive properties as characterized in the available DC gun setup. Chapter 4 presents the experimental investigation of the Cs_3Sb cathodes performance in both the DC gun beam line and the PHIN RF photoinjector, having as a basis for comparison the tests performed with Cs_2Te cathodes. The correlation between the photoemissive properties and the cathodes surface composition is studied in Chap. 5. The XPS (X-ray Photoelectron Spectroscopy) analyses detailed in this chapter were performed on both cesium antimonide and cesium telluride cathodes, as newly produced and after usage either in the DC gun setup or in the PHIN RF photoinjector.

Chapter 2

Photocathodes for photoinjector applications

Since the discovery of the photoelectric effect by A. Einstein, which earned him the Nobel Prize in the 1921, photoemissive materials have been widely studied. The photoelectric conversion can be classified in external photoelectric effect, in which photoelectrons are emitted into the vacuum from a material, and internal photoelectric effect when the electrons are excited to the conduction band. The former is the effect exploited by photocathodes while the latter is known as photoconductive or photovoltaic effect. In the seventies a huge variety of photoemissive materials was known and has had found already application in specific technologies such as radiation detectors (photodiodes, photomultipliers) and imaging tubes, as reported by Sommer (9).

In the last decades, together with the development of laser based electron sources, photocathode materials has become of interest also for particle accelerator applications. The range of output currents exploited by the former uses is, however, well below the design average currents of high brightness electron sources. As a comparison, the current flowing through the photocathode of a photomultiplier tube in normal operation is in the order of picoamperes (10) while the nominal PHIN average current in the macro-pulse is 3.4 A, therefore 12 orders of magnitude higher.

In this chapter, after introducing the main photocathode features, a brief literary review on photocathodes used for laser-based electron sources will be presented, highlighting the main differences between metals and semiconductors.

2.1 Photocathode main features

Photocathodes are materials that emit electrons when illuminated with light. The physical phenomenon which is exploited in the applications of photocathodes is the photoemission process. The photoemission can be seen as a three steps process, as explained by the Spicer's model (11, 12), consisting of (Fig. 2.1):

1. Absorption of a photon with a consequent excitation of an electron,
2. motion of the electron towards the surface of the solid, during which the electron loses energy through electron-electron or electron-phonon scattering,
3. the escape of the electron into the vacuum, if the final electron energy is high enough to overcome the surface barrier.

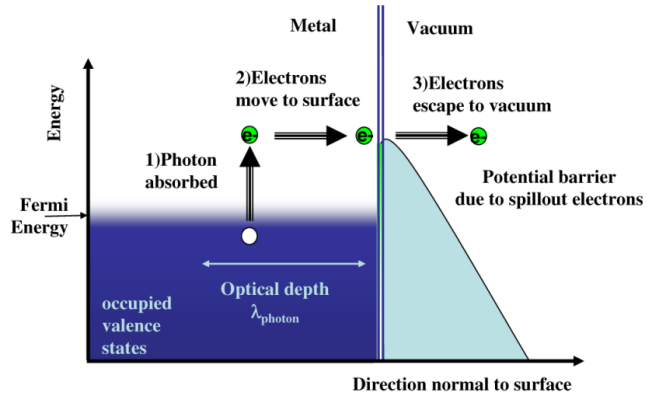

Figure 2.1: Schematic representation of the Three Steps Model for photoemission from a metal (13)

In a photoinjector (Fig. 2.2), electron bunches are generated by a pulsed laser beam, which illuminate a photocathode installed inside an accelerating structure. Depending on the applications, different setups (combination of cathode, laser and gun) can be chosen. The main advantage of using an RF photoinjector, instead of a thermionic gun, is that the electron beam is generated already with the desired time structure (14). The initial electron beam quality and shape are determined by the incident laser beam and the rapid acceleration in the RF field, which is synchronized with the laser, preserves the beam characteristic. Unfortunately, there exist no photocathode versatile enough

to fulfil all the requirements and various compromises are made depending on the particular application (15).

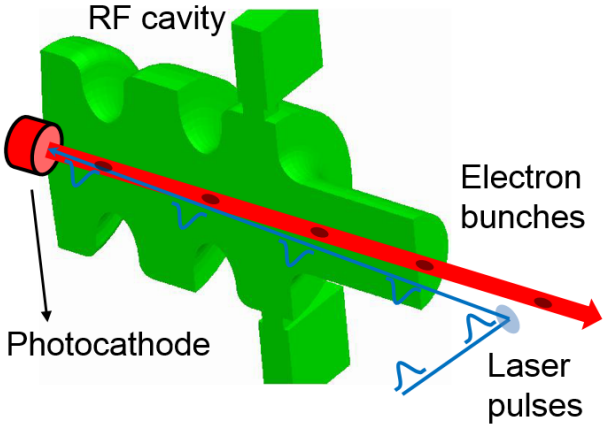

Figure 2.2: Schematic layout of an RF photoinjector

The photocathode features, which are relevant for photoinjector applications are: quantum efficiency, time response, cathode lifetime, thermal emittance and dark current.

Quantum Efficiency

The quality of a photocathode is measured with the Quantum Efficiency (QE):

$$QE = \frac{number\ of\ emitted\ electrons}{number\ of\ incident\ photons} \tag{2.1}$$

In practical units (and for a pulsed laser) QE is expressed as

$$QE[\%] = \frac{124 \cdot Q[nC]}{\lambda[nm] \cdot E[\mu J]} \tag{2.2}$$

where Q is the bunch charge, λ is the laser light wavelength, E is the laser pulse energy at the photocathode. The dependence of the QE on the laser wavelength is not linear. Figure 2.3 shows, as an example, the spectral response for Cs_3Sb photocathodes, where the photoemissive yield corresponds to the QE.

It is evident that the photoemission threshold defines which laser wavelengths can be used in combination with the specific cathode material, while the QE sets the re-

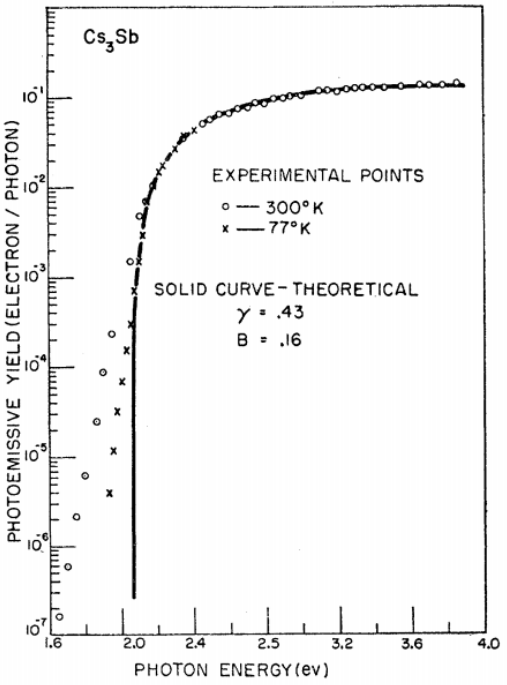

Figure 2.3: Spectral response of a high quantum efficiency Cs_3Sb cathode (11)

quirements to the laser pulse energy. Consequently, high charge photoinjectors require high quantum efficiency cathodes.

Time response

Known also as relaxation time, this parameter indicates the time to convert and extract all the electrons produced by photons (16). The time response is strongly related to the dominating collision process that the electrons undergo after being excited by photons and it is directly related to the material's QE (12). In Table 2.1 theoretical estimates of the response time (t), based on the Three Steps Model, are given for both semiconductors and metals.

Material	**Mode of scattering**	**Estimated t[sec]**	**QE values** (1eV above threshold)
Metals	Electron-electron	10^{-15} to 10^{-14}	10^{-5} to 10^{-4}
Semiconductors	Electron-lattice	10^{-13} to 10^{-12}	10^{-2} to 10^{-1}

Table 2.1: Estimated value of response time and QE based on the Three Steps Model (12).

As highlighted in Table 2.1, a faster time response is associated with decreased QE (more details in Sec. 2.2.1). For metals, the electron-electron scattering dominates so that only electrons excited close to the surface can escape (9). This leads to the fastest response.
Depending on the time profile (bunch length, repetition rate) of the electron beam required by the specific application, a faster relaxation time may be needed to preserve the laser beam temporal structure.

Cathode lifetime

The photocathode performance, therefore the QE, deteriorates over time due to many degrading phenomena which will be discussed in more details in the following chapters. There are different mathematical definitions of the lifetime, the most used is the 1/e lifetime (τ) which takes into account the exponential-like decay of the QE over time:

$$QE(t) = QE(t_0)exp(-t/\tau) \tag{2.3}$$

Sometimes one can also refer to the **charge lifetime**, which is defined as the amount of charge that can be extracted before the QE falls to 1/e of its initial value (17). Particular care has to be taken while comparing lifetime values found in literature. Some authors may refer to the so called **vacuum lifetime**, i.e. the QE degradation while storing the cathodes in a UHV (Ultra High Vacuum) chamber. Some lifetime values pertain to the period over which the photoinjector daily operation was possible with the same cathode. Some other authors may even refer to QE values measured by powering both the laser and the DC (Direct Current) or RF gun from time to time.

Hereafter the **operational lifetime** will be related to the QE decrease during continuous photoinjector operation at fixed electron beam parameters.
Increasing the cathodes lifetime is one of the main goals of the research and development on photoinjectors. For an operational electron source, the minimum lifetime must be longer than the total time needed to produce and exchange the cathode, including the transport and the pumping-down time. However, for minimizing the photoinjector downtime, much longer lifetime are desired.

Thermal emittance

Many applications involving electron sources (free electron lasers, linear colliders, 4^{th} generation light sources) require high brightness electron beams usually produced by photoinjectors (15). The brightness B_n is the ability of the beam to be focused in all dimensions:

$$B_n \left[\frac{A}{m^2 \cdot rad^2} \right] = \frac{2 \cdot I}{\epsilon_{nx} \cdot \epsilon_{ny}} \tag{2.4}$$

where I is the peak current and ϵ_{nx}, ϵ_{ny} are the normalised transverse emittances in the plane x and y, respectively[1]. The brightness value at the injector of a linear accelerator can only be deteriorated along the accelerator (20). The thermal (intrinsic) emittance determines the lower limit of the normalized emittance of electron beams in injectors (21).

Assuming isotropic emission into the hemisphere in front of the cathode surface, the thermal emittance ϵ_{th} is related to the average kinetic energy of emitted electrons E_k through Equation 2.5:

$$\epsilon_{th} = \sigma_l \sqrt{\frac{2E_k}{3m_0c^2}} \tag{2.5}$$

where the σ_l is the laser spot size (assuming Gaussian beam profile) and m_0c^2 is the electron rest mass. The average kinetic energy of the emitted electrons depends on the incident photons energy $h\omega$, on first approximation, as:

$$2E_k = h\omega - \phi \tag{2.6}$$

where ϕ is the work function for a metal, and the sum of energy gap and electron affinity for semiconductors. Equation 2.5 is an approximation valid under certain assumptions. For example the effect of Schottky reduction of the barrier in presence of the electric field is ignored, the temperature is considered to be zero so that the Fermi-Dirac distribution becomes the Heaviside step function for metals and only prompt electrons are considered for the semiconductor case. A more detailed explanation can be found in literature (22).

[1]The emittance is an important characteristic of propagating charged particle beams. The emittance measures the spread (area) of particles in phase space. The normalized emittance is a convenient way to express the same concept with a quantity which is conserved during acceleration. More details on emittance can be found elsewhere (18, 19).

It has to be pointed out that the effective intrinsic emittance depends also on several effects such as a non uniform QE of the cathode, surface impurities and the surface roughness (22, 23, 24). The cathode roughness, in fact, leads to an additional uncorrelated divergence of the emitted electrons and therefore to an increased thermal emittance (25).

The CLIC drive beam emittance requirements are less demanding than what is normally required for a standard photoinjector. The drive beam, in fact, is conceived only to supply with the RF power the main beam accelerating structures. The emittance studies are out of the scope of this work. Extensive emittance simulations and measurements in the PHIN photoinjector, that demonstrated the feasibility of the beam emittance parameters set by design, can be found elsewhere (6, 26).

Dark current

The field emitted electrons generated in an accelerating structure creates the so-called dark current, which parasitically absorbs radio frequency energy (in RF cavities), causes radiation issues, backgrounds, noise in instruments and possibly wakefield (27). Moreover the dark current, together with local outgassing and plasma formation, seems to be the precursor of RF breakdown[1] which in turn limits the operation of accelerators and can cause irreversible damage to their physical structure. Dark current, which is produced at every RF pulse, is therefore a crucial point in operating photoinjector facilities. The dark current measured in a photoinjector consists of two fractions: one part originating from the gun body and one part emitted from the cathode itself. The second contribution can change from cathode to cathode (31). By improving cleaning and handling of cathodes, the dark current component depending on the cathode itself can be reduced. Dark current studies were performed in the framework of this study and will be presented in Chap. 4.

[1]RF breakdowns produce a very fast and localized dissipation of stored energy inside accelerating cavities. Although such phenomena have been extensively studied (28, 29), a consistent theory associated with them has not been established. RF breakdowns are accompanied with the emission of electron bursts, acoustic waves, visible light and vacuum activity (pressure bursts) (28). They normally occur in areas of both high surface electric or magnetic field as well as in areas with local defects or large particles contamination. In accelerating cavities, RF breakdowns limit the working power and in certain cases produce irreversible surface damage (30).

2.2 Photocathodes overview

The Three Steps Model for the photoemission allows to explain the differences between photoemission from metals and from semiconductors from a qualitative point of view (9). In this brief literary review, some examples of the state-of-the-art of photocathodes development will be also presented. It is important to keep in mind, when comparing the experimental results, that different setups have been used (electron gun or simpler electrodes configuration) and different instruments were measuring the produced charge (beam instrumentation devices or picoammeters).

2.2.1 Metallic cathodes

For metals the reflectivity of the light spectrum in the visible region, including near infrared and near ultraviolet, is usually high (optical reflectivity $\sim 60\%$ (32)). As a consequence, the absorption of a photon, i.e. the first step of the photoemission, is seen as an unlikely process in metals (9). Moreover, as previously mentioned, the excited electron loses energy by inelastic scattering during its motion towards the surface. In metals, the most probable loss process is the electron-electron scattering, which may cause a big decrease in the energy so that the final energy of the electron is not enough to escape the surface barrier (the mean free path can be as low as 1 nm (12)). In metals, the surface barrier is given by the work function ϕ, which is the minimum energy needed to remove an electron from a solid to a point immediately outside the solid surface. In Table 2.2 the work function values of some commonly used metallic photoemitters are listed. Those values are higher than 3.5 eV, which corresponds to the near UV wavelength range.

Metals	**Workfunction [eV]**
Cu	4.6 (9)
Mg	3.6 (33)
Pb	4.0 (9)
Nb	4.38 (9)

Table 2.2: Work function of some metallic photoemitters

Following all these arguments, metallic photocathodes result in low QE (from 10^{-5} to 10^{-4}) and the need of using UV light, which limit their relevance to applications

requiring low average current (∼mA) (22). Metals are nonetheless used in many photoinjector facilities (22) as they are easy to produce, they can be transported in air and they have a very fast relaxation time (Sec. 2.1). Moreover, they are more tolerant to vacuum contamination than the semiconductor cathodes and have therefore a potentially longer lifetime (15).

2.2.2 Semiconductor cathodes

In semiconductors, instead, the absorption coefficient for photon energies above the band gap energy (i.e. the difference in energy between the top of the valence band and the bottom of the conduction band) is often very high (optical reflectivity $\sim 10\%$ (32)). As a consequence, the conversion of photon into electron energy is more efficient for semiconductors than for metals, provided the photon energy is higher than the band gap. Moreover, the second step of the photoemission process is dominated by different phenomena in the semiconductor. The electron-electron scattering is indeed negligible compared to the energy loss by phonon scattering, i.e. interaction with the lattice (9). In the latter process, the energy loss per interaction is much smaller than in electron-electron scattering and the excited electron can reach the surface even if it was originated deeper in the solid (the mean free path for electron-phonon can be as large as $\sim$ 10 nm (32)). To better understand the role of the surface barrier in the semiconducting materials one has to consider the band model diagram.

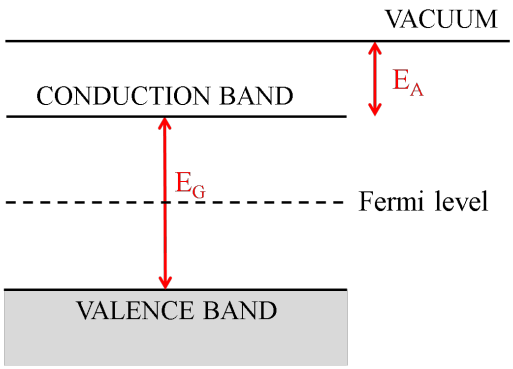

Figure 2.4: Idealized energy band model of an intrinsic semiconductor.

Figure 2.4 shows an idealized case, which ignores the shape of the bands as determined by the density of the states, the presence of defects levels in the forbidden

gap and any band-bending effects near the surface. A photon which is absorbed by a semiconductor can raise an electron from the valence band to the conduction band if the energy is above the energy gap E_G. However, in order to escape into the vacuum, the electron must have enough energy to overcome the electron affinity E_A. Therefore the minimum energy a photon must have to make the photoemission process possible in a semiconductor is E_G+E_A, but semiconductors normally show a higher QE than metals (9). To be sensitive to visible light this sum must be lower than 3 eV (less than 1.7 eV to cover the whole visible region). This condition is fulfilled for some complex semiconductors: Table 2.3 show a list of the possible candidates for photoinjector applications.

Type	**Cathode**	**E_G+E_A[eV]**	**Threshold [nm]**
Mono-alkali	Cs_2Te	3.3+0.2 (34)	350
	Cs_3Sb	1.6+0.45 (9)	604
	K_3Sb	1.1+1.6 (9)	458
	Na_3Sb	1.1+2.44 (9)	350
Multi-alkali	Na_2KSb	1+1 (9)	618
	(Cs)Na_3KSb	1+0.55 (9)	798
	K_2CsSb	1+1.1 (9)	589
NEA	GaAs(Cs,F)	1.4 ±0.1 (9)	884

Table 2.3: Most commonly used semiconductor photocathodes (22)

Cesium telluride

Cesium telluride cathodes are widely studied (35, 36, 37) and effectively used in many photoinjector facilities (Los Alamos Advanced FEL (38), FLASH and PITZ at Desy (21), ELBE at HZDR (39)).

At CERN there is a long history of Cs_2Te photocathodes (40) and excellent QE values, up to QE$\sim$ 24%, were obtained for co-deposited cathodes (more details in Chap. 3), probed with a laser beam at λ=266 nm (photoemission threshold $\sim$3.5 eV, as shown in Table 2.3). A detailed investigation of the performance of Cs_2Te photocathodes was conducted in the PHIN RF photoinjector to study the lifetime dependence on the beam parameters and on the vacuum level (41). These photocathodes showed a 1/e lifetime of 250 hours (for 2.3 nC and 350 ns train length), after the vacuum setup upgrade, and

allowed the production of a record bunch charge of 9.2 nC. Their performance will be further discussed in the following chapters as comparison with the cesium antimonide photocathodes.

Alkali-antimonide cathodes

Alkali-antimonide cathodes were used for many decades in building photoemissive devices (9). For these applications, they showed high quantum efficiencies in the visible range, as displayed in Fig. 2.5, and good stability over many years, but their feasibility in the much more demanding environment as the RF gun of a photoinjector is not completely demonstrated.

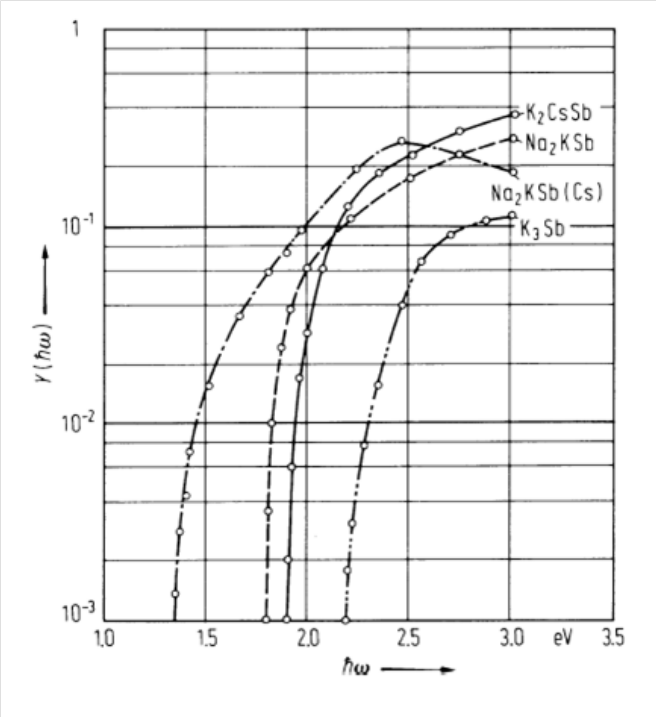

Figure 2.5: Spectral response of some alkali-antimonides (11)

Since the earlier investigations of alkali antimonides, extensive experimental works have been carried out. The crystal structure of the $(K_{1-x}Cs_x)_3Sb$ ($0 \leq x \leq 1$) series of compounds was determined (42) as well as their electronic structure (43, 44) and their photoemissive properties (45).

The two alkali-antimony compounds that have been more investigated for photoinjector development are Cs_3Sb (this thesis) and K_2CsSb.

Cs_3Sb

A sketch of the simplified band structure of the compound Cs_3Sb at room temperature is shown in Fig. 2.6 (45). Detailed theoretical work on its electronic band structure, density of states, linear optical properties and a more recent photoemission model can be found in literature (44, 46). However, this material was not extensively studied in the frame of photoinjectors development.

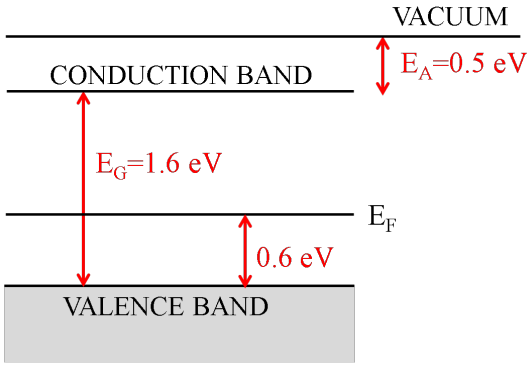

Figure 2.6: The simplified band structure of Cs_3Sb

Cesium antimonide photocathodes produced at LASA Laboratory (INFN (47)) following a recipe adapted by the one from Sommer (9), i.e. a subsequent layers deposition, showed a maximum QE of 9%, as measured in the preparation chamber with an electrodes setup, for the cathode deposited on a copper substrate. This type of photocathode material was also studied in the frame of the LANL (Los Alamos National Laboratory) photoinjector program (48). They reported average QE of 4 % for λ= 527 nm, but a very short lifetime ($T_{\frac{1}{2}}$=4 hour, i.e. time during which the QE decreased to half of its initial value) in an RF gun setup (49).

Cs_3Sb was chosen as the candidate for this study for its low photoemission threshold, which allows the use of a green laser beam for producing photoelectrons, and also because it is a two components material. This feature permitted to use the same preparation setup (shown in Chap. 3) that is used for cesium telluride photocathodes, taking advantage of the experience acquired with high quality co-deposited Cs_2Te cathodes.

K_2CsSb

The compound K_2CsSb was discovered by Sommer (50) and its production and characteristics were investigated by several authors (14, 47, 51, 52). Slightly different fabrication processes were studied, but usually K_2CsSb photocathodes are produced by the sequential evaporative deposition (refer to Sec. 3.3) of Sb, K and Cs onto a metal (molybdenum, copper or stainless steel) while heating the substrate to temperatures above 120°C (14, 53, 54). The Cs deposition stage, and sometimes also the deposition of the K, is normally controlled in order to reach a maximum in the photoemission current, which is monitored during the deposition.

The impact of the different substrates on K_2CsSb photocathodes was investigated by some authors (52, 53). Performing Auger depth profiling on such photocathodes, Bona et al. (52) observed a continuous photoemissive film on a stainless steel substrate, whereas island formation has been observed for deposition onto molybdenum. Better results for stainless steel substrate are also reported by Smedley et al. (53). The photocathodes showed a QE one order of magnitude higher than the ones deposited onto copper. Some authors (14, 55) reported that, with the multilayer production technique, K_2CsSb photocathodes can routinely reach a QE$\sim$10% when illuminated with λ=532 nm.

The 1/e lifetime of K_2CsSb cathodes can be as high as 10000 hours (vacuum lifetime) when stored in the preparation chamber UHV system at 25°C, but it drops drastically (few hours of operational lifetime (14)) when operated in the RF gun injector. Dowell et al. attributed the cathode degradation during operation mainly to the water vapour contamination, whereas the heating, by either the laser or the RF fields, which could cause the evaporation of Cs from the cathode surface, is negligible. They moreover successfully applied rejuvenation of used K_2CsSb photocathodes by heating it at 120°C in a clean vacuum environment in order to remove the water molecules without affecting the photoemissive film. The same authors proposed to operate the RF gun at 120° to increase the operational lifetime, assuming that the benefit of reducing the absorbed water vapour greatly offsets the disadvantage of Cs evaporation.

Also di Bona et al. ascribed the very short lifetime shown during operation of K_2CsSb cathodes in an RF photoinjector to the poor vacuum condition (52). Such photocathodes are effectively sensitive to residual gas exposure, as tested by Michelato et al. (56, 57) and Bona et al. (52). The worst poisoning effect, in terms of QE

degradation, has been observed for controlled exposure to CO_2 and to O_2, while K_2CsSb photocathodes are rather insensitive to CH_4,N_2 and CO. Controlled exposure to a small quantity of O_2, instead, may lead to a QE increasing thanks to the reduction of the surface barrier due to the formation of a Cs-O surface dipole layer. However, above a certain exposure value the superficial oxidation changes the electronic structure of the photocathode reducing its photoemission yield (52).

There is still a lot of work ongoing intended to improve the production process of bi-alkali antimonide cathodes (58, 59). In-situ characterization by material analysis techniques (x-ray diffraction and x-ray photoemission spectroscopy) is used to correlate the growth recipe and the microscopic structure and eventually the photocathode performance.

The knowledge gained from the studies of K_2CsSb cathodes might be useful for the development of Cs_3Sb cathodes, which are believed to have similar performance.

NEA cathode: GaAs

Gallium arsenide has been extensively studied and routinely used in the past years for high brightness electron source applications (e.g. the ALICE photoinjector gun at the Daresbury Laboratory (60), the Jefferson Lab in the US (61) and the MAMI facility of the University of Mainz (62)). GaAs cathodes (Fig. 2.7 (60, 63, 64)) can be activated to a Negative Electron Affinity (NEA) state by depositing cesium and an oxidant layers (O_2 or NF_3) onto their highly p-doped surfaces (65). For NEA materials, the vacuum energy level is located below the conduction band minimum and electrons with a range of energies excited into the conduction band can easily escape after tunneling through the potential wall.

GaAs cathodes are used in combination with a DC gun setup as high brightness source of highly polarized (66) or un-polarized electron beams (60). This type of photocathode shows, for un-polarized electron beam, high QE over a wide part of the visible spectrum: generally achieved QE higher than 3% for 355 nm (67) and a record QE= 35% for 635 nm (68). The main disadvantage of GaAs photocathodes is that they require extremely good vacuum condition. As a matter of fact, their QE is substantially reduced under exposure to oxygen, carbon monoxide and carbon dioxide (65). For this reason, they could not be used in an RF gun setup, where the vacuum level is always worse than a DC gun.

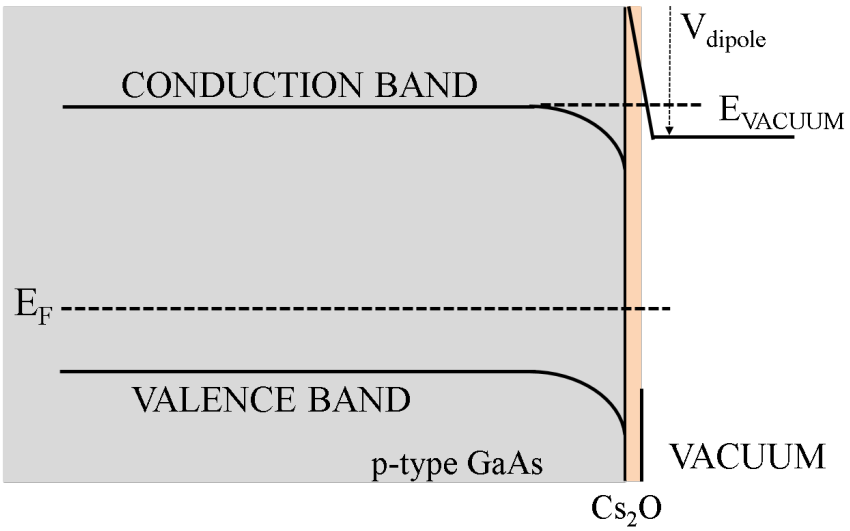

Figure 2.7: Schematic energy diagram for an intrinsic GaAs surface deposited with Cs and O layers showing a negative electron affinity (NEA) state.

2.2.3 Other electron emission processes

Photoemission is not the only phenomenon which leads to the emission of electrons from a solid surface. Other processes like thermionic emission, field emission and multiphoton processes can occur together with photoemission, which will be briefly discussed in this section.

Thermionic emission

The thermionic effect is exploited in the so called thermionic gun. This type of electron source is actually foreseen to be, in combination with a sub-harmonic bunching system, the drive beam source in the CLIC baseline design (5). For metals the thermionic work function corresponds exactly to what was called work function, which is also the photoemission threshold. For intrinsic semiconductors, instead, the thermionic work function is given by E_G+E_A (Fig. 2.4). Figure 2.8 represents the thermionic process as for a metal: the Fermi distribution inside the solid has a very long tail towards high energy states because of the thermal excitation enabling some electrons to cross the potential barrier and escape into vacuum (69).

One should be aware of the thermal excitation effect (already at ambient tempera-

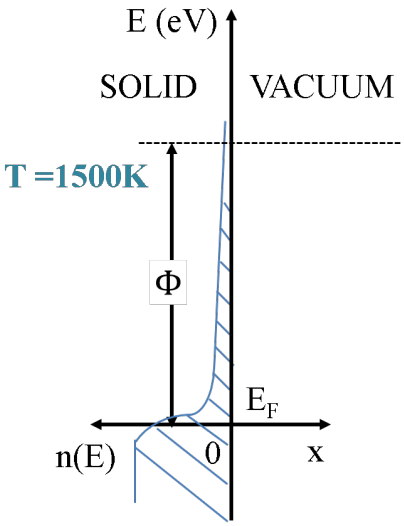

Figure 2.8: Energy diagrams of the thermionic emission: T is the temperature of the solid, E the energy, n(E) the electron distribution in the solid, ϕ the work function, E_F the Fermi level

ture, i.e. 300 K) which may in turn affect the photoemission process by, for example, occupying the inter-gap levels in the extrinsic semiconductors (9).

Field emission

The electric field also affects the surface potential of a solid and may lead to field emission. To understand this process, one can consider a metal-vacuum interface (Fig. 2.9). As already mentioned, without the field the surface barrier seen by an electron in a metal has a height equal to the work function ϕ. The electric field lowers the surface barrier by a factor of $\Delta\phi = \sqrt{\frac{E \cdot e^3}{4\pi \cdot \epsilon_0}}$, where E is the electric field, e is the electron charge, ϵ_0 is the vacuum permittivity. The surface barrier lowering can be as big as to allow the electrons to escape the solid: **Schottky Effect or Field emmission**. Particularly the Schottky-enabled photoemission may occur. As shown in Fig. 2.9, a photon with energy lower than the photoemission threshold can cause the escape of an electron from the surface (70). In photoinjector applications, the electric field seen by the cathode surface can be very high (in the range of 10 MeV/m) and therefore can contribute to the electron emission process (field assisted photoemission but also dark current). As environment dependent, however, this effect has to be considered separately for every specific application.

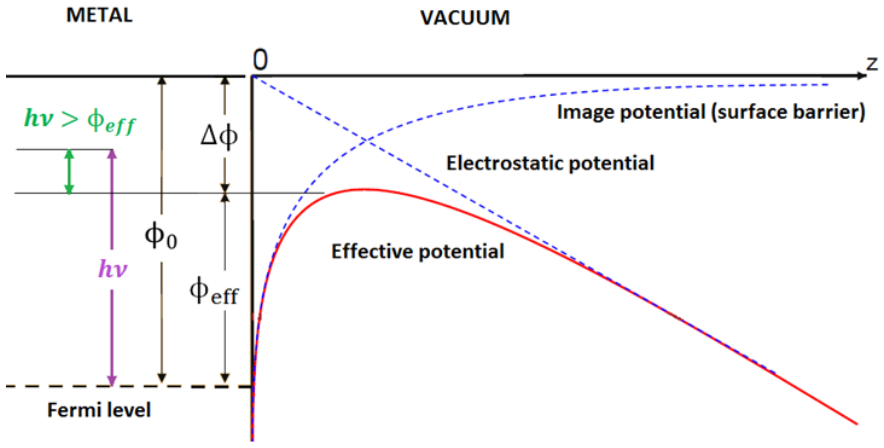

Figure 2.9: Schematic representation of the Schottky-enabled photoemission process from a metal: ϕ is the nominal work function, $\Delta\phi$ is the work function lowering due to the electric field, $\phi_{eff} = \phi - \Delta\phi$ is the effective work function, $h\nu$ is the photon energy

Multiphoton process

One should note that also **multiphoton process** may occur. Two or more photons with energy lower than the photoemission threshold may be capable of exciting the same electron. Although this possibility exists, such effect becomes relevant only at very high light intensity and its contribution is much lower than the one photon photoemission (71). Therefore the multiphoton effect will be neglected in this work.

Chapter 3

Photocathodes production at CERN

Photocathodes are normally produced by thin-film (i.e. a layer of material ranging from fractions of a nanometer to several micrometers in thickness) vapour deposition. Vapour phase deposition techniques are classified in Physical Vapour Deposition (PVD) and chemical vapour deposition depending on the mechanism of production of depositing species: physical or chemical reactions. There are many PVD techniques, all characterized by three steps: creation of a vapour-phase, transport from source to substrate and film growth on the substrate. In the photocathode literature, only some of these techniques are described as commonly used: evaporative deposition, pulsed laser deposition and sputtering deposition.

- **Evaporative deposition** was used since the very first applications of photoemissive materials (9) and it is still the most common photocathode production technique. It consists of pumping a vacuum chamber to pressures of less than 10^{-5} mbar and heating a material (evaporative source) to produce a flux of vapour in order to deposit the material onto a surface. The material to be vaporized is typically heated until its vapour pressure is high enough to produce an evaporation rate of several Angstroms per second by using an electrically resistive heater or by bombarding it with a high voltage beam (electron beam evaporation). A sufficiently high vacuum level is important both to allow the vapour to reach the substrate, without reacting with or scattering against other gas-phase atoms in the chamber, and to reduce the incorporation of impurities from the residual gas

in the vacuum chamber. The energy of depositing species (atoms and ions) is generally low (tenths of eV), but the deposition rate can be high (up to hundreds of nm/min).

- **Pulsed Laser Deposition** (PLD) is for many reasons a versatile technique. Films are prepared by the ablation of one or more targets illuminated by a focused pulsed-laser beam. PLD is a technique particularly suited for the production of thin films since it provides good adherence between film and substrate due to the high kinetic energy of the deposited species (atoms, ions and clusters): up to 100 eV.

  Metallic photocathodes based on thin films prepared with PLD has been extensively studied (72). Mg films grown by PLD gave promising results in term of achievable QE and uniformity of emission (73).

- **Sputter deposition**: a target is bombarded with energetic ions (typically argon) in a high vacuum environment, the ejected atoms are then deposited onto the substrate. Atoms and ions can be deposited at different energies up to hundreds of eV, but at a generally low deposition rate. Sputtered films have generally a better adhesion on the substrate than evaporated films, but the sputtering process is quite complex to control. Sputter deposition setups often employ magnetrons (74) that confine an Ar plasma close to the surface of the sputter target by means of a strong electromagnetic fields to enhance the deposition rate.

  Sputter growth of alkali antimonide photocathodes was recently investigated as an alternative to the sequential evaporative deposition towards smoother surface (75). Despite the fact that the resulting surface roughness is decreased, the measured QE is low, suggesting the process is far from being optimized.

At CERN photocathodes are produced by co-deposition (a special evaporative deposition) on copper substrates. The substrate preparation and the production process will be detailed in the following sections, as well as the photocathodes characterization in the DC gun beam line.

3.1 The CERN photoemission laboratory

Photocathodes are produced and characterized in the **photoemission laboratory** (40). As schematically shown in Fig. 3.1, the photoemission laboratory setup is made of a UHV preparation chamber and a UHV beam line equipped with a 70 kV DC electron gun.

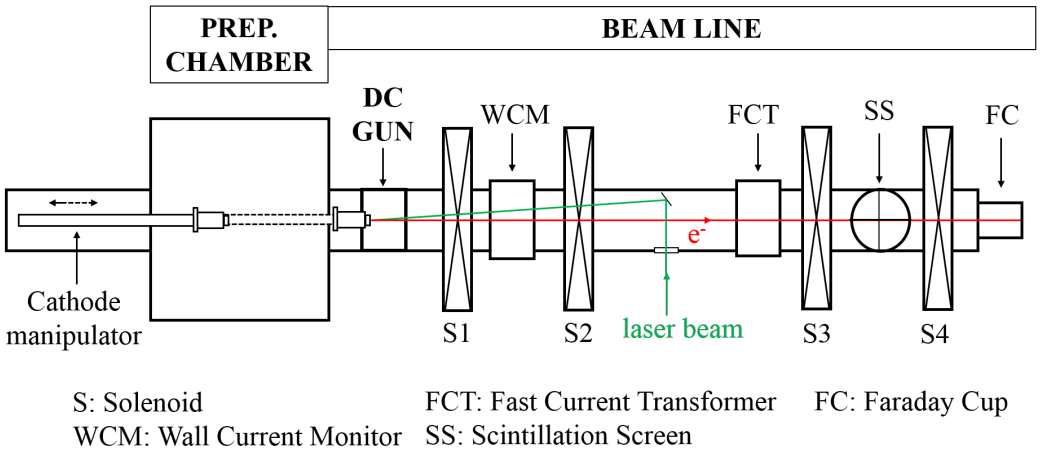

Figure 3.1: The photoemission laboratory setup

The photocathodes grown in the preparation chamber following the co-deposition process (detailed in Sec. 3.3) are afterwards transferred under vacuum to the DC gun using the manipulator setup (76), for characterization of their photoemissive properties (Sec. 3.4). The photoemissive surface is probed with a pulsed laser beam, which enters the vacuum system through a viewport and is deflected by a mirror, installed inside the vacuum chamber, onto the photocathode surface. As a result, a pulsed electron beam (indicated as "e^-" in Fig. 3.1) is produced and accelerated to 70 keV in the DC gun. The electron beam transport in the beam line is optimized using the four focusing solenoids (S1, S2, S3, S4), while the electron pulse charge can be measured with various beam instrumentation devices: the wall current monitor (WCM), the fast current transformer (FCT) and the Faraday cup (FC) placed at different distance downstream the DC gun, as displayed in Fig. 3.1. In addition, a profile monitor based on a CsI scintillation screen (SS) coupled with a CCD camera (more details can be found elsewhere (77)) is installed for a direct observation of the beam. The WCM is used to measure the longitudinal beam profile. By integrating the WCM signal is

possible to compute the bunch charge extracted from the DC gun. The other devices, also used for monitoring the longitudinal beam profile, are positioned in such a way that they suffer from the losses which the beam undergoes during the transport in the line. The mentioned devices are characterized by different principle of operation and performance.

- In a **WCM** a resistor is connected across a gap made in the wall of the vacuum pipe (78) and the image current, which accompanies the beam along the inside of the vacuum pipe, is forced to pass through the resistor developing a voltage across it. Each real WCM has a limited bandwidth and the particular design of the WCM installed in the photoemission laboratory setup, results in a working region between 1 MHz-10GHz (79). Therefore, it is not suitable for measuring pulses longer than tens of ns.

- The **FCT** is used to measure the bunch intensity. In a FCT the electron beam can be considered as the single turn primary winding of a transformer, with its equivalent current transformed to the secondary winding output (80). The FCT installed in the photoemission laboratory beam line (FCT-LD-50:1, Bergoz Instrumentation) has a large bandwidth (0.32 kHz-650 MHz), which makes it suitable for intensity measurements of pulse length up to the μs range without distortion of the signal.

- The **FC** is basically a device for destructive measurements: it collects the total beam charge by an electrode. The FC is suitable also for low intensity beam measurements.

The UHV level ($P<10^{-10}$ mbar) is maintained in the whole system due to various pumping devices (not shown in Fig. 3.1), such as sputter-ion pumps and titanium sublimation pumps, also known as evaporable getters, installed either in the preparation chamber (1 ion sputter-pump and 1 titanium sublimation pump) and in the beam line (5 sputter-ion pumps and 3 titanium sublimation pumps). Different vacuum gauges (Bayard-Alpert and Penning gauges (81)) are used to monitor the pressure level and a Residual Gas Analyzer (RGA) (82) is able to reveal the gas composition in the preparation chamber.

Two different laser setups are available in the photoemission laboratory:

- A Q-switched Nd:YAG laser (Spectron model SL802), operated at 10 Hz and 5 ns pulse duration, which is used for the production process and the photocathodes characterization (Sec. 3.4);
- A Q-switched high repetition rate (up to 2 kHz) Nd:YAG laser (Quantronix model 532 DP-1), used for lifetime measurements in the DC gun setup (Sec. 4.1).

The laser beam is matched with the type of photocathode being probed: for Cs_3Sb cathodes the 2^{nd} harmonic (λ=532 nm) is used while Cs_2Te cathodes require the 4^{th} harmonic (λ=266 nm).

3.2 Substrate preparation

The substrates used for photocathodes production are CERN-made OFE (Oxygen- Free Electronic grade with oxygen content$<$ 0.0005%) copper samples with a cylindrical shape (Fig. 3.2). Different substrate materials were considered in the past at CERN in the framework of Cs_2Te cathode studies (35, 83) and the copper was eventually chosen given the best results in terms of QE and lifetime.

Figure 3.2: Picture of the CERN copper substrate

The photoemissive layer is deposited onto the top circular surface over a 16 mm diameter area as a result of the electron collector, used for on-line QE measurement (Sec. 3.3), shading the vapour flow .

3.2.1 Surface finishing

The quality of the substrate finishing is of prior importance, reasonably assuming that the subsequently deposited thin photoemissive layer (10-100 nm thickness) does not smooth the surface. As introduced in Sec. 2.1 and detailed later in Sec. 4.2.4, the field enhancement factors, related to a high roughness surface, can have a negative impact on the operation in a high voltage gun (dark current, breakdowns). A low roughness substrate surface was taken therefore as a prerequisite to have a smooth final cathode surface[1]. To fulfil such requirement, roughness constraints on the top surface were set by design (R_a <0.02 μm) and two different surface finishing techniques were investigated at CERN:

- **Diamond turning**, a multi-stage process used to remove surface layers for precision elements. A diamond-tipped lathe tool is used in the final stages of the manufacturing process to achieve sub-nanometer level surface finishes and sub-micrometer form accuracies. Nonetheless, following such machining, concentric circular traces are visible, also by naked eyes, on the copper surface as shown in Fig. 3.3 (a).

- **Diamond powder polishing** is a gentle form of grinding (abrasive cutting). Fine hand polishing is required to remove surface blemish and to get a mirror-like surface. It was performed as a second step after the diamond turning. As reported by Dowell, polishing the substrate is important for lowering the dark current (14). With the performed diamond powder machining, however, scratches can be found on the substrate top surface (Fig. 3.3 (b)).

3.2.2 Cleaning procedure

For vacuum components, appropriate chemical cleaning processes are needed, which depend on the material itself and on the pressure regime required (85). The CERN standard cleaning procedure, optimized for vacuum compatibility, is used for the copper substrates. Such chemical cleaning scheme can be detailed as follow:

[1] Although the photocathodes roughness might also influence the electron beam emittance (84), such topic will not be treated, considering the relaxed emittance requirement for the specific application that motivated these studies (Sec. 1.2)

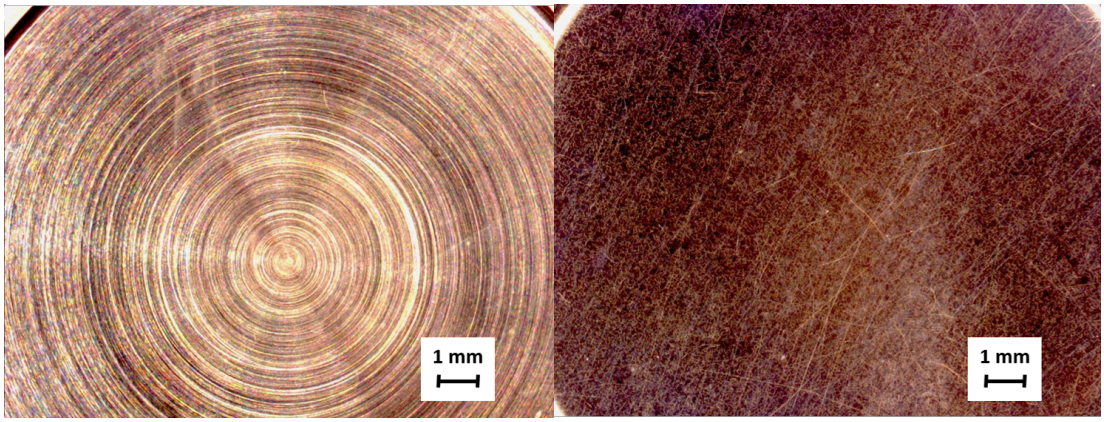

Figure 3.3: Optical microscope images of two different copper substrates: (a)diamond turned surface, (b)diamond powder polished surface

- **Degreasing** is done by ultrasonic cleaning with detergent (NGL 17.40 spec. ALU III, 50-60 °C, for 30-60 minutes).
- After having rinsed with water, in order to remove the oxides a **pickling** is done with hydrochloric acid (concentration 50%, room temperature, for 10-30 seconds).
- The copper samples then undergo **passivation** with chromic acid (H_2CrO_4 70-80 g/l, H_2SO_4 3ml/l, room temperature, for 10-20 seconds), which serves to prevent the adsorption of contaminants into the surface or prevent the permeation of gas from the bulk material into the vacuum system. After rinsing with water, the samples are dried with clean compressed air.

After the substrates insertion into the preparation chamber done under atmospheric pressure, the whole system is pumped and baked at a minimum temperature of 150° C for almost two days. As a result, the copper substrates are following a **vacuum annealing** treatment, but at a temperature which might be too low to effectively remove the eventual residual contamination (85).

3.2.3 Roughness requirements

As already mentioned, roughness requirements of the copper substrate top surface has been set by design as R_a <0.02 µm. The arithmetic average roughness R_a is defined as the average absolute deviation of the roughness irregularities from the mean line over one sampling length as shown in Fig. 3.4 (86).

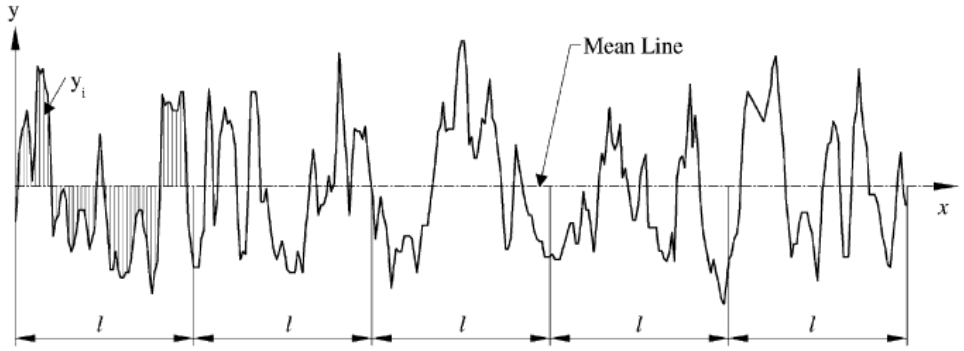

Figure 3.4: Definition of the arithmetic average roughness.

The mathematical definition and the digital implementation of the arithmetic average roughness are, respectively, as follow:

$$R_a = \frac{1}{l}\int_0^l \mid y(x) \mid \, \mathrm{d}x \tag{3.1}$$

$$R_a = \frac{1}{n}\sum_{i=1}^{n} \mid y_i \mid \tag{3.2}$$

To investigate the quality of the two different finishings, roughness measurements of several coppers substrates were performed by the CERN Metrology team using an optical profilometer (VEECO-NT 3300). The analysis of this data, performed within the scope of this thesis, underlined that the R_a requirement is not fulfilled for many diamond turned substrate surfaces. A more detailed investigation highlighted that some turned surfaces for which the constraint on the average roughness parameter is respected, present the previously mentioned concentric ring structure, which is obviously not associated to a very smooth surface. The morphology of the diamond powder polished surfaces, instead, respect the roughness requirement but can be influenced negatively by a too strong acid treatment during the subsequent cleaning procedure as displayed in Fig. 3.5. Therefore, additional care should be taken during the standard cleaning procedure to avoid a strong etching of the surfaces.
Moreover, the average roughness, which is easy to define and easy to measure, does not give any information about the long wavelength component of a measured surface profile and it is not sensitive to small changes in the profile (86). Relying only on this parameter could give misleading interpretation of the surface condition, as in the

case of turned substrates. Therefore, further investigations are needed to include additional roughness requirements in the technical drawing of the copper substrate (such as constraints on the root mean square roughness) to improve the quality of the surface finishing.

As a guideline, a compromise between cleanliness and roughness should be reached taking into account the cost in terms of money and time of high quality machining techniques.

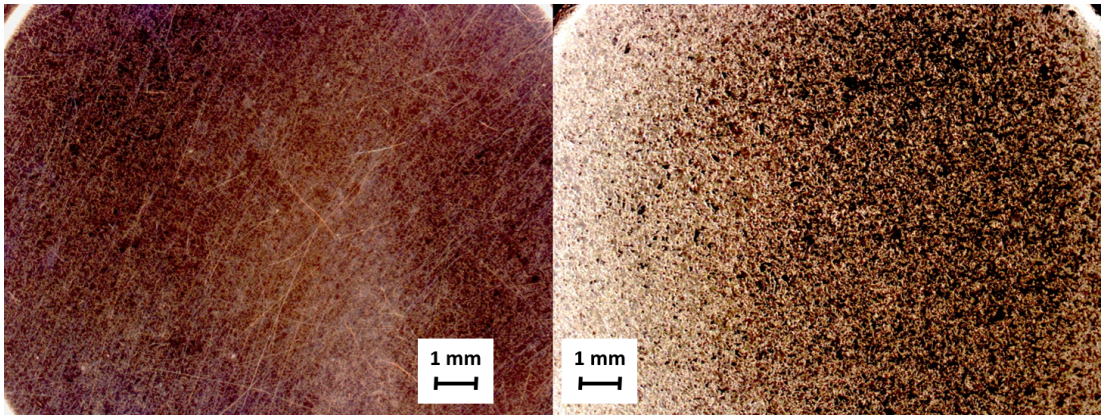

Figure 3.5: Optical microscope images of a polished copper substrate (6A34): (a)before the cleaning procedure (R_a ~0.007 µm), (b)after the chemical cleaning procedure (strong acid treatment) (R_a ~0.4 µm)

3.2.4 Experimental investigations of alternative surface cleaning procedures

Within the scope of this thesis, experimental investigation of two different copper surface cleaning procedures was performed at Daresbury Laboratory in collaboration with the ASTeC/STFC Vacuum Science Group (87). Four different diamond powder polished OFE copper samples from CERN were probed in a VG ESCALAB Mk II instrument, which was modified to achieve UHV conditions (88) and equipped for vacuum annealing and for X-ray Photoelectron Spectroscopy analysis (more details on XPS technique in Chap. 5). Two of them (#007,#009) have followed the CERN standard cleaning procedure (Sec. 3.2.2) and two of them (#001,#003) were treated at Daresbury Laboratory with a **oxygen plasma cleaning** setup (Henniker Plasma HPT 200). During the plasma cleaning, the positive oxygen ions from the plasma are accelerated

towards the sample surface and can scrub the surface to remove contaminants. Moreover, the oxygen ions (O^+,O_2^+) can react with the contaminants present on the surface, such as carbon, forming volatile reaction products (CO and CO_2). After the contamination removals, a well ordered oxide layer is promoted on top of the clean surface. This oxide surface provides a protective layer during the transfer under atmospheric conditions and a subsequent vacuum annealing process (250°C for 1 hour) dissolves the oxide layer into the bulk.
Also samples cleaned at CERN were annealed to remove the residual oxygen and carbon content. The impact of the two different procedures was investigated with XPS, for evaluating the cleanliness, and with white light interferometry, for measuring the roughness. The surface relative elemental composition for the different copper samples, at different stages of the treatment, are listed in the following tables (Table 3.1, Table 3.2, Table 3.3, Table 3.4).

#001	**Cu [%]**	**O [%]**	**C [%]**
as received	3.8	75.9	20.3
O_2 plasma cleaning	13.9	36.5	49.6
annealed	58.3	16.6	25.1

Table 3.1: Surface elemental composition of copper sample #001 at different stages of the cleaning procedure

#003	**Cu [%]**	**O [%]**	**C [%]**
as received	3.9	17.4	78.7
O_2 plasma cleaning	32.1	47.5	20.4
annealed	72.8	16.5	10.7

Table 3.2: Surface elemental composition of copper sample #003 at different stages of the cleaning procedure

On both not cleaned samples as received (Table 3.2 and Table 3.1), a strong contamination of oxygen and carbon (probably associated to hydrocarbons) was shown by the XPS analysis. This is likely due to the storage condition, as they were kept for a long time in a non-protected environment and they were transported in plastic bags. Sample #001 was additionally affected by an incautious handling after the oxy-

gen plasma cleaning, which explains the carbon content $\sim$ 50%. In both cases, the annealing was effective in reducing the oxygen content down to the 16%.

#007	**Cu** [%]	**O** [%]	**C** [%]
CERN cleaning	18.4	40.4	41.2
annealed	58.3	22.5	49.2

Table 3.3: Surface elemental composition of copper sample #007 at different stages of the cleaning procedure

#009	**Cu** [%]	**O** [%]	**C** [%]
CERN cleaning	30.1	27.1	42.8
annealed(2 cycles)	78.3	16.6	5.1

Table 3.4: Surface elemental composition of copper sample #009 at different stages of the cleaning procedure

As shown in Table 3.3 and Table 3.4, also the copper samples which followed the CERN chemical cleaning presented surface contamination. Nonetheless, the annealing procedure allowed to reduce the carbon contamination (down to 5% in case of two cycles of annealing) and to reach similar oxygen content as for the two samples treated with the oxygen plasma cleaning.

The roughness measurements taken with the white light interferometry showed that neither the oxygen plasma cleaning, performed at 0.4 mbar gas pressure, nor the annealing process are affecting the smoothness of the copper surface. As already mentioned, the storage and handling have an impact on the surface state. Therefore, each sample has its own life history. As a general guideline for future development of the substrate treatment, a vacuum annealing process should be included, possibly at higher temperature (450° C) to reduce the residual contamination. The oxygen plasma cleaning, used in combination with the annealing, result in similar contamination levels than the CERN chemical cleaning followed by annealing and it does not affect the surface roughness. Therefore the oxygen plasma cleaning, which is a fast and more reproducible technique, could be considered as an alternative to the CERN chemical cleaning.

Aiming to improve the substrate finishing, a special technique which polishes and cleans the surface at the same moment was also considered: the **electropolishing**, an

electrochemical treatment that removes material from metal objects surface (89). The metal is immersed in an electrolyte and subjected to direct current. The metal part to be treated is made anodic and under certain conditions, a controlled dissolution of the metal is achieved. If the working parameters are properly chosen, the electropolishing allows to smoothen, polish, deburr and clean metal surfaces. Differently than the mechanical based polishing, this technique does not produce either direction lines or stress on the surface. Moreover, the final surface does not need further chemical treatment as the surface contamination is removed during the treatment. However, preliminary trials did not show satisfactory results as the substrate top surface presented deep scratches. In order to follow up this option, further studies are required to optimize the process parameters together with the substrate dimension requirements, as in the stationary regime this technique will lead to material removal on the edges of the electropolished piece.

3.3 Photocathodes production by co-deposition

As an alternative to the sequential layers evaporative deposition, which relies on the inter-diffusion of the subsequent deposited cesium layer into the tellurium film for the compound formation, the co-deposition (or co- evaporation) process was proposed at CERN by G. Suberlucq back in 2001, during the development of cesium telluride photocathodes (40, 90). Evaporating the two elements (Cesium and Tellurium) at the same time allows them to mix together in the vapour phase. Since the very first investigations, the co-deposited Cs_2Te photocathodes showed improved quantum yields and lifetimes with respect to ones produced with the classical evaporation process (15, 90) and excellent results were obtained in the following years (QE up to $\sim$20% (40)). Therefore, the same process was chosen for producing cesium antimonide photocathodes. The deposition setup is shown in Fig. 3.6.

CERN-made Sb (and Te) dispensers, fabricated on molybdenum crucibles, and commercial Cs dispensers (SAES Getters S.p.A.) are used as evaporative sources. The evaporators setup, shown in Fig. 3.6(b), allows to resistively heat each dispenser independently due to the dedicated power supplies. This mechanical design permits to accommodate two sets of dispensers. During the deposition, the OFE copper substrate (presented in Sec. 3.2) is located inside the RF oven (shown in Fig. 3.6(a)), which allows

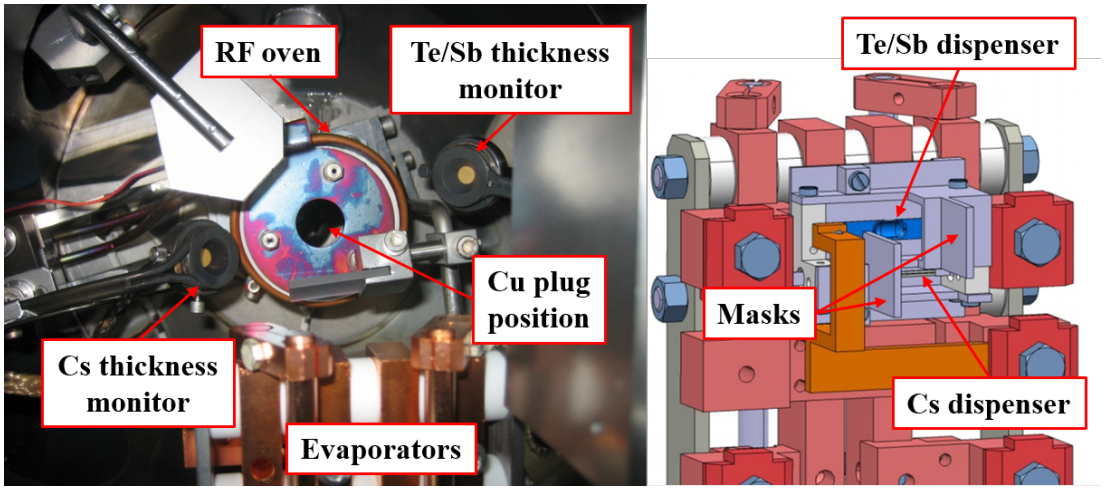

Figure 3.6: The co-deposition setup:(a) picture of the inside of the preparation chamber, (b) 3D drawing of the evaporators setup which is facing the RF oven during the deposition.

the heating of the substrate by means of an induction system (91)[1]. The heating of the substrate up to 130°C should accelerate the reaction of compound formation as well as prevent metallic cesium from condensing on cold part of the substrate. The heating temperature is limited due to the decomposition of the Cs_3Sb compound which start around 200°C (9). Since 2006, the chamber is equipped with two thickness monitors (Quarz microbalances) which can measure the deposition rate of the two evaporated elements separately[2] due to two shielding masks shown in Fig. 3.6(b). The co-deposition process is optimized in order to reach a maximum of the QE (as detailed in the following paragraphs), whose evolution is monitored in real time during deposition by illuminating the cathode with a pulsed green laser beam (or UV laser beam for cesium telluride) and collecting the photoemitted electrons with a circular anode.

The preparation chamber, which is separated by a vacuum valve from the beam line, is not equipped with a load-lock system for substrates insertion from air to the UHV sector. Each time a new set of 3 substrates (which is the number of available

[1]Cs and Te are instead deposited while keeping the substrate at room temperature as experimental evidences showed that good quality cesium telluride cathodes can be obtained on cold substrate (40)

[2]Ideally, the evaporators power can be adjusted to produce a vapour mix with the desired stoichiometric ratio (40). In reality, the calibration procedure of the thickness monitor dedicated to the alkali metal vapour is an extremely complex task. The lack of alternative thickness measurements, compatible with the delicate handling of the metallic cesium in air, has not yet allowed to optimize this configuration.

storage positions inside the preparation chamber (76)) is loaded into the system, the whole preparation chamber needs to be baked and pumped limiting therefore the time availability for photocathodes production. The procedure of opening the chamber includes also the replacement of dispensers, as the evaporators arm is part of the same vacuum sector as the preparation chamber. As a consequence, the dispensers cannot be exchanged without venting the whole preparation chamber. This feature limits the reliable photocathodes production, mainly because of the little availability of cesium, which is set by the Cs dispenser capacity. Solutions to overcome these limitations were studied in parallel works, as discussed in Chap. 6.

3.3.1 Analysis of production data

Within the scope of this thesis, the data acquired during several deposition processes was thoroughly analyzed, trying to find a correlation between the final quantum efficiency and the production parameters (92).

A software interface allows to monitor the time evolution of the substrate temperature, the deposition rate and the deposited thickness of the two different elements, the evaporators power and the photocurrent. The deposition process is not automated (40), the evaporators power, and therefore the deposition rates, are manually controlled.

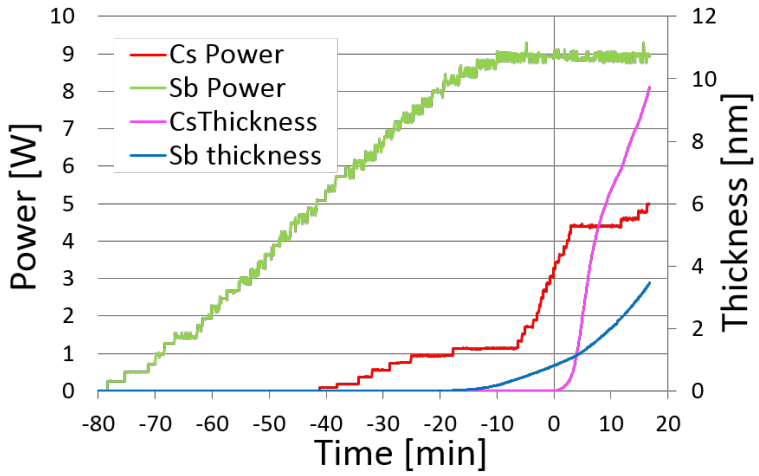

Figure 3.7: The time evolution of the deposited thickness and evaporator power for cesium and antimony during the production of cathode #192 (Cs_3Sb)

Figure 3.7 shows, as an example, the evolution of the evaporators power and the

deposited thickness (as measured by the quarz microbalances), for the growth of cathode #192. The production process starts by slowly increasing the antimony evaporator power while the substrate temperature, as measured by a thermocouple, is already at the target temperature (within 120°-140° C). At a later stage, also the cesium evaporator power is increased in small steps of 0.2 W. In Fig. 3.7, the origin of the time scale is set on the starting of the film deposition, triggered by a consistent vapour flow as seen by the Cs thickness monitor. The fine tuning of the evaporation rates is then performed by the operator while checking the photocurrent trend.

Figure 3.8 shows the typical behaviour of the vapour stoichiometric ratio during the evaporation in relation with the QE trend over time (same time axis origin as Fig. 3.7). The stoichiometric ratio of the vapour mixture is estimated from the deposition rates

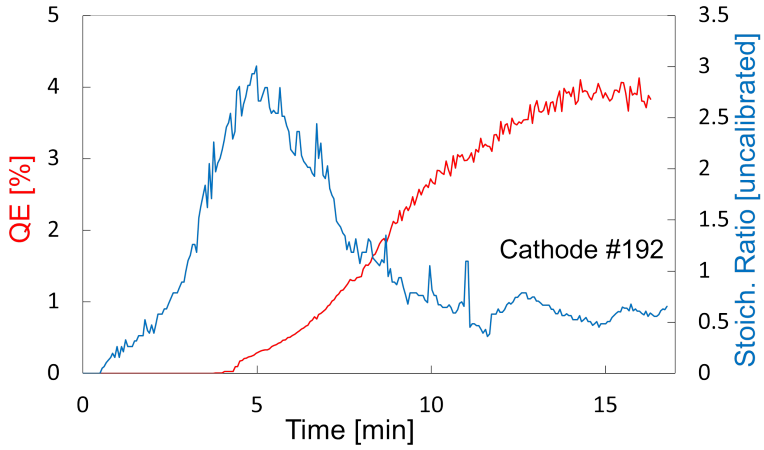

Figure 3.8: QE and vapour stoichiometric ratio evolution during the the co-deposition process of cathode #192 (Cs_3Sb)

measured by the quarz microbalances. Following the consideration done on the calibration of the thickness monitors for the cesium vapour rate measurement, it is evident why the stoichiometric ratio is indicated as "uncalibrated". The photocurrent is measured during the evaporation collecting the electrons on an anode, biased at 1 kV, but the QE values plotted in Fig. 3.8 are normalized to the yield measured in the DC gun setup right after the production process.

During the evaporation, the total pressure inside the preparation chamber ranges between 10^{-9} mbar to 10^{-7} mbar (measured with a Bayard Alpert gauge). The main desorbed gases during the evaporation process, as measured by the RGA, are hydrogen

and carbon monoxide, which are associated with the gas evolution of the cesium dispenser (93). The high vacuum level is maintained with a cold trap, which is activated only during the film growth, in addition to the previously mentioned sputter-ion pump and the titanium sublimation pump. The sputter-ion pump, which is a gas binding pump working in a wide range of pressure (10^{-4}-10^{-10} mbar), is effective in pumping CO, CO_2, N_2, O_2, H_2 but also the eventually present noble gases (94). The titanium sublimation pump, which instead has a smaller working range (10^{-7}-10^{-11} mbar), is particularly suitable for pumping H_2O, CO and CO_2. The cold trap, which walls are cooled by immersion in liquid nitrogen, can assist in the pumping of H_2O and CO_2.

After the photoemissive film growth, the cathode is transferred into the 70 keV DC gun setup and illuminated with the pulsed laser beam produced by the Spectron laser (laser spot centred on the cathode, σ ~2 mm). The electron pulse charge and the laser pulse energy are measured with the WCM and a laser energy meter (Polytec Laser Probe model Rjp-735), respectively. From these values, the QE is computed. An increase of the photoemissive yield during the first hours of electron beam generation, is a relevant effect for cesium antimonide photocathodes (Fig. 3.9 as an example). This behaviour can lead to an improvement of almost a factor two of the initial QE value.

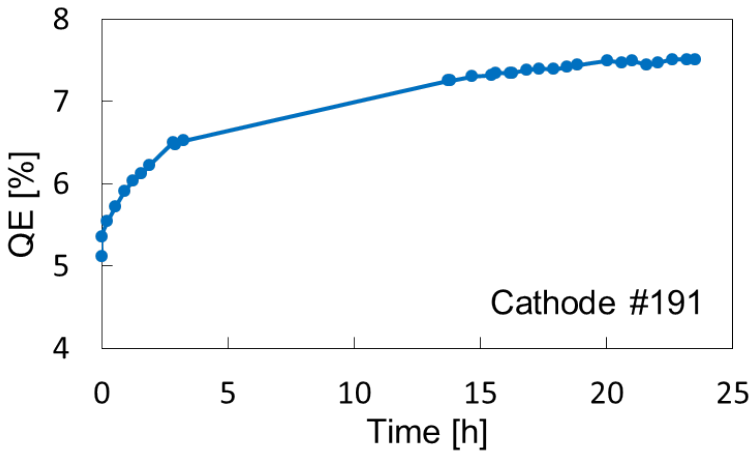

Figure 3.9: QE improvement during the first hours of beam production with cathode #191 (Cs_3Sb)

The laser influence could be related to a surface cleaning effect, otherwise the laser beam could behave as catalyst of the compound formation still ongoing. The lack of an in-situ material analysis setup did not permit to confirm neither hypotheses.

Table 3.5: Cs_3Sb photocathodes produced at CERN by co-deposition. For each cathode several information are displayed: The cathode reference number, the substrate surface finishing, the initial QE, the final maximum QE (after the first hours of beam production), the thickness (*not calibrated) of the two evaporated elements

No.	Subs. treat.	In. QE [%]	Max QE [%]	Ev. Cs [nm*]	Ev. Sb[nm*]
178	none	0.3	0.5	120	18.4
179	none	1.4	2.3	156	24.5
180	none	0.6	1.0	52	14.4
187	Polishing	0.3	0.4	67.6	4.7
188	Polishing	1.3	2.2	152	17.8
189	Polishing	2.3	4.4	64	15
191	Turning	5.4	7.5	156	14
192	Polishing	2.0	2.7	9.7	3.5
193	Turning	4.2	5.8	10.8	7.6
194	Polishing	2.7	4.5	18.7	20.7
199	Polishing	3.5	5.2	270	22.7
200	Polishing	3.4	5.5	83.3	23.5
202	Polishing	2.9	4.0	75.9	4.2

A summary of the Cs_3Sb cathodes produced at CERN by co-deposition is shown in Table 3.5. The first attempts (cathodes produced at CERN are numbered in chronological order) did not result in high quality Cs_3Sb. However, for the latest produced cathodes high QE values (up to 7.5%) were obtained.

However, the data shown in Table 3.5 does not show an obvious correlation between the photoemissive layer thickness, the evaporated ratio and the final photoemissive yield. Both for thick layers (#191) as well as very thin layers (#193), good photoemissive yield could be achieved. Cathode #199 (evaporated Cs/Sb ratio $\sim$12) has a QE close to the one of cathode #200, which is characterized by a much smaller Cs/Sb ratio ($\sim$3.5). Moreover, similar QE values were obtained for film deposited onto turned (#193) and polished (#200) substrate. It is known that the optimum thickness represents a compromise between the light absorption, which is reduced if the film is too thin, and the loss of electrons, which increases with the thickness of the layer. As a results, the thickness of the photoemissive layer seems not to affect critically the photoemissive properties, as already noted by Sommer (9). Regarding the robustness

of the deposited film, however, the thickness and the substrate finishing could have an influence. These features will be investigated in Chap. 4. The variability of the final quantum efficiency value and the film thickness is a consequence of the not automated procedure and suggests that the production process is not fully reproducible for Cs_3Sb cathodes. This limitation will be further discussed in Chap. 5, where the XPS analyses on a cathode as grown will be presented.

3.4 Photoemissive properties characterization

The photocathode characterization in the DC gun setup follows each deposition process and includes QE measurement with the laser illuminating the cathode center, the QE mapping and the continuous electron beam productions, during which the yield improvement is observed until a plateau is reached (around 24 hours).
The QE maps (Fig. 3.10) are obtained scanning the photocathode surface with a small spot size laser beam (σ ~1 mm), while the produced charge is measured with the WCM. A precise stepping motor controller and an automated acquisition system were commissioned in 2012 for this purpose. This setup allows to probe the photocathodes in a fast and reliable way at different stages of its life to study the evolution of its photoemissive properties, as shown in the following chapters.

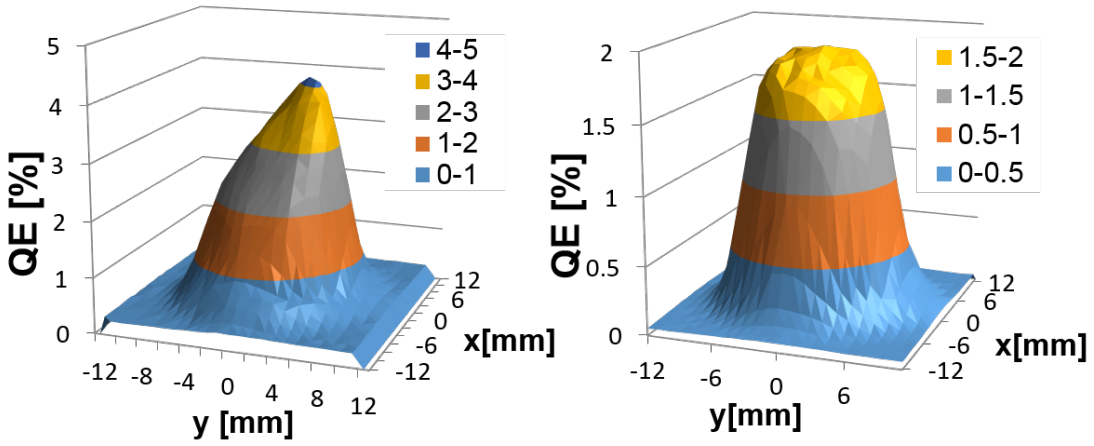

Figure 3.10: QE maps of two different Cs_3Sb cathodes as grown (note the different scale): (a) Cathode #191, (b) Cathode #192. The QE map is a peculiarity of each photocathode: cathode #191, for example, has a less uniform profile than cathode #192 probably related to a slightly bent dispenser.

Chapter 4

Cathode studies in the DC gun setup and in the PHIN RF photoinjector

As mentioned in Chap. 2, the quantum efficiency is not the only important cathode feature when dealing with photoinjector applications. The lifetime and dark current are also relevant parameters for assessing the cathode feasibility for the specific application. Several studies were performed in the PHIN photoinjector to test the Cs_3Sb cathodes performance in an RF gun under the high peak gradient and for different beam parameters. The available DC gun beam line and the high repetition rate laser setup, permit to perform lifetime measurements for average current comparable with the test done in PHIN at 1 μA as well as for high integrated produced charge (∼120 μA average current). The results and discussion of these measurements will be presented in this chapter, also comparing with Cs_2Te cathodes performance.

4.1 Lifetime measurements in the DC gun setup

The lifetime measurements were performed during continuous beam production in the DC gun beam line described in Sec. 3.1. During these tests, the laser power was adjusted to keep the electron beam current at a chosen constant value: 1 μA (low average current) and 120 μA (high average current) (92).

The high repetition rate Quantronix laser system was used for producing electron

beam at average current >1 μA. To reach a similar current value with the 10 Hz rep. rate Spectron laser, in fact, a bunch charge higher than 100 nC would be needed. The charge extraction from the gun, however, is limited by the space charge effect[1] which becomes relevant already at 63 nC/bunch even for a laser spot size of $\sigma \sim 2$ mm (Fig. 4.1).

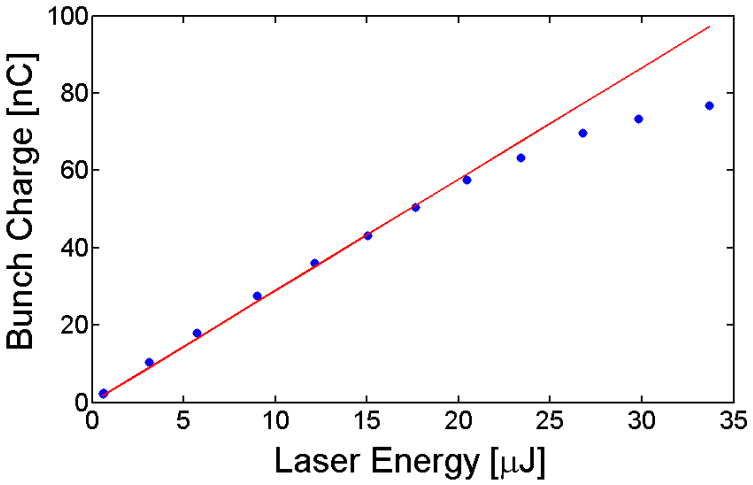

Figure 4.1: Saturation of the extracted charge from the DC gun operated at 70 kV

Therefore, the lifetime studies were performed using the second harmonic (λ=532 nm) of the Quantronix laser, operated at 100 ns pulse length and 1 kHz repetition rate, for low average current test, or 2 kHz repetition rate, for high average current measurements. Given the long pulse duration, the bunch charge is measured with the FCT instead of the WCM (considering the devices bandwidth, Sec. 3.1), while the laser power is quantified with a power meter.

Cathode #188 generated a total charge of 321 mC at an average current of 1 μA over almost 4 days. Since this cathode was previously used for electron production, its QE at the beginning of the lifetime measurement was much lower than the fresh cathode QE listed in Table 3.5.

The pressure in the DC gun was below the detection limit of the vacuum gauge (P<10^{-11} mbar) for the whole duration of the experiment. Fig. 4.2 shows the QE decay for cathode #188 at 1 nC bunch charge. The QE dropped from 0.57% to 0.50%

[1]The Coulomb force interacting between same charge particles lead to beam emittance growth and associated beam losses as well as the saturation of the extracted charge from a photocathode gun. More details on space charge effects can be found elsewhere (95)

in 90 hours, leading to a 1/e cathode lifetime of 530(± 40) hours. The extrapolated lifetime is much higher than the lifetime measured at the PHIN photoinjector, with a different Cs_3Sb cathode, at the same average current, as detailed in Sec. 4.2.3.

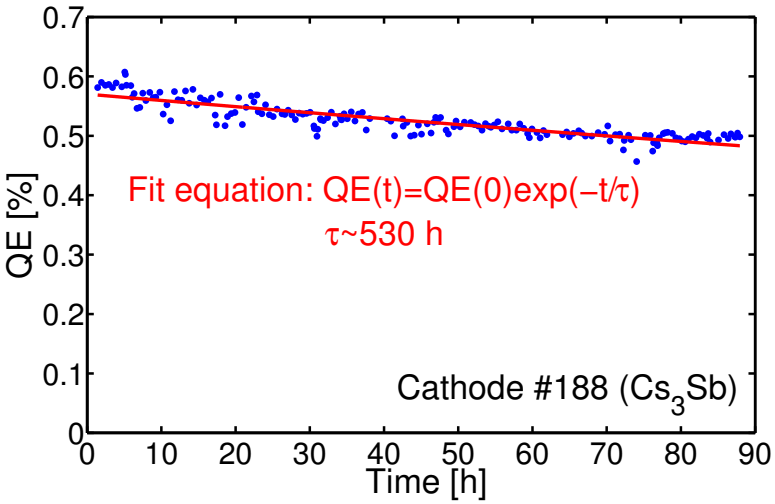

Figure 4.2: Cathode #188 (Cs_3Sb) tested at 1 μA average current

Cathode #192 was tested at high average current(120 μA) using a large beam size ($\sigma \sim$1.5 mm).

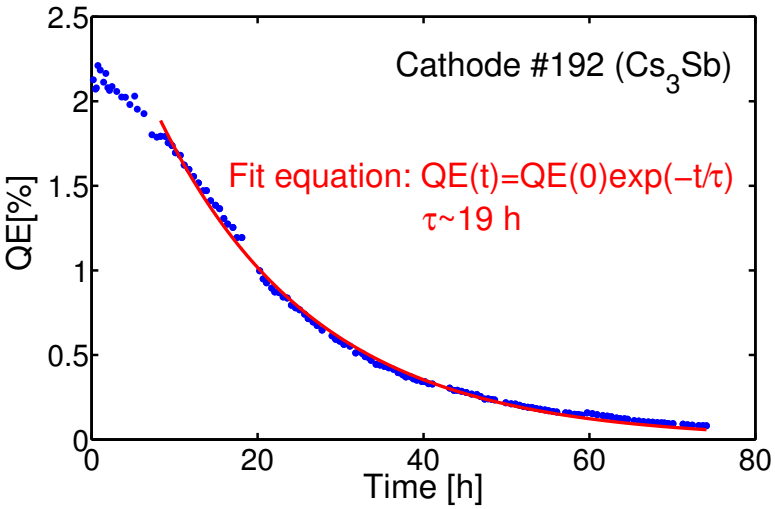

Figure 4.3: Cathode #192 (Cs_3Sb) tested at 120 μA average current

The total extracted charge is 33 C over 3 days. Despite few peaks due to break-

downs[1], the pressure in the gun stayed below 8×10^{-11} mbar during the experiment. Figure 4.3 shows the rapid QE decrease from 2.07% to 0.09% in 75 hours. The 1/e lifetime is ∼18.8 (±0.2) h.

The QE of cathode #202 (Fig. 4.4), instead, decreased from 3.4% to 0.5% in 70 hours of beam production, delivering 35 C of total charge. This cathode was probed for the same beam parameters (120 μA) as cathode #192, but showed a lifetime two times longer (42 ±0.3 hours). The vacuum level was comparable with the former test at high average current measurements: P∼5×10^{-11} mbar with few pressure bursts.

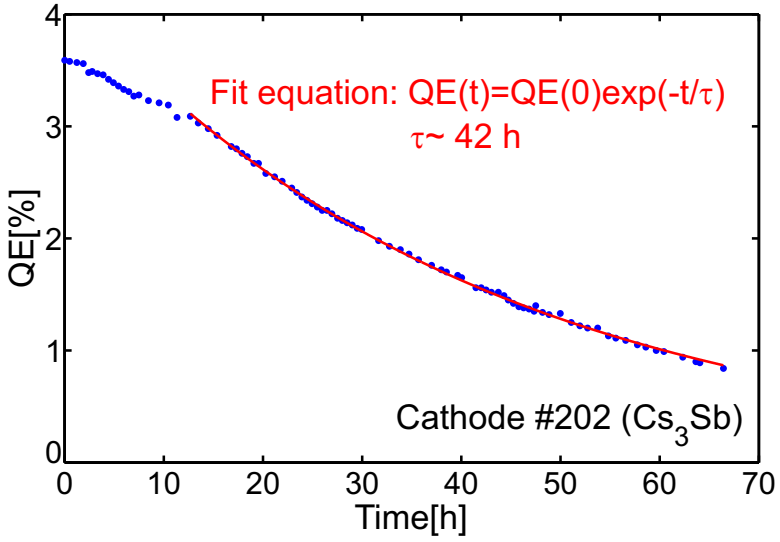

Figure 4.4: Cathode #202 (Cs_3Sb) tested at 120 μA

The photocathode deteriorating processes (Fig. 4.5) can be divided in two families: chemical poisoning (residual gas contamination) and "radiation damage" (ions and electrons bombardment).

- The first category is associated with chemical reaction of the photocathode surface with the residual gases, creating mainly oxides, but also other compounds (as shown in Chap. 5), which in turn reduce the photoemissive yield. In addition to a good static vacuum (background pressure), the dynamic vacuum level, i.e. during operation, should be controlled as much as possible. There are many

[1]Breakdowns can happen also in high voltage DC applications (30), but the phenomenon is less frequent than for the RF cavities.

phenomena that can originate pressure bursts such as field emitted electron stimulated desorption (ESD) and desorption induced by beam losses, i.e. interaction of the beam with the inner walls of the vacuum chambers. The ESD process, mainly located inside the photocathode gun, is due to field emission induced by the high peak gradient and it is therefore strongly related to the dark current, discussed in Sec. 4.2.4.

- The "radiation damage" processes include both the impact of ions and electrons. The ions back bombardment is associated to the ionization of the residual gases by the electrons (mainly the electron beam) within the gun. The ions can then be accelerated towards the cathode at high energy (depending on the gun peak gradient) by the electric field and impact onto the cathode surface (96, 97). In addition, field emitted electrons in the RF cavity can potentially hit the cathode (97, 98, 99).

CHEMICAL POISONING	RADIATION DAMAGE
➢ Static vacuum level	➢ Electrons (from field emission) back bombardment
➢ Electrons (from field emission) stimulated desorption	➢ Ions back bombardment
➢ Electrons (from beam losses) stimulated desorption	

Figure 4.5: Photocathode deteriorating processes (blue: beam independent processes, red: beam dependent processes)

Whereas the detrimental reactions due to the background vacuum level and the field emission related processes are independent of the beam properties, contamination related to beam losses induced desorption and damage for ions back bombardment are, in first approximation, proportional to the beam current (100) and therefore strongly dependent on the beam parameters. The beam losses can be minimized optimizing the beam transport, but the ionization of residual gases by the beam can only be partially mitigated by reducing the residual gases with a vacuum setup upgrade.

The much shorter lifetimes of cathodes #192 and #202, compared with the low average current measurement, are attributed to beam induced high dynamic vacuum level. The influence of ions back bombardment, instead, is believed to be negligible as the QE maps (Fig. 4.6 and Fig. 4.7) showed only an overall QE reduction, with respect to the fresh cathodes, and not localized damages, which instead were observed for the cathodes tested in the PHIN RF photoinjector (Sec. 4.2.6).

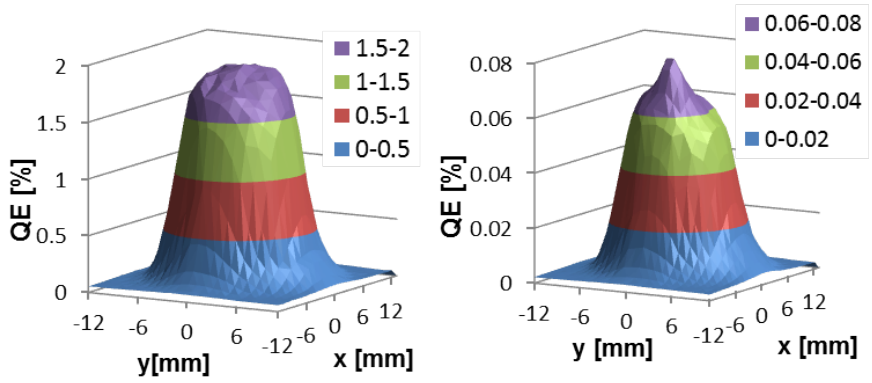

Figure 4.6: QE maps of cathode #192: (a)as newly produced, (b)after lifetime measurement at high average current in the DC gun setup

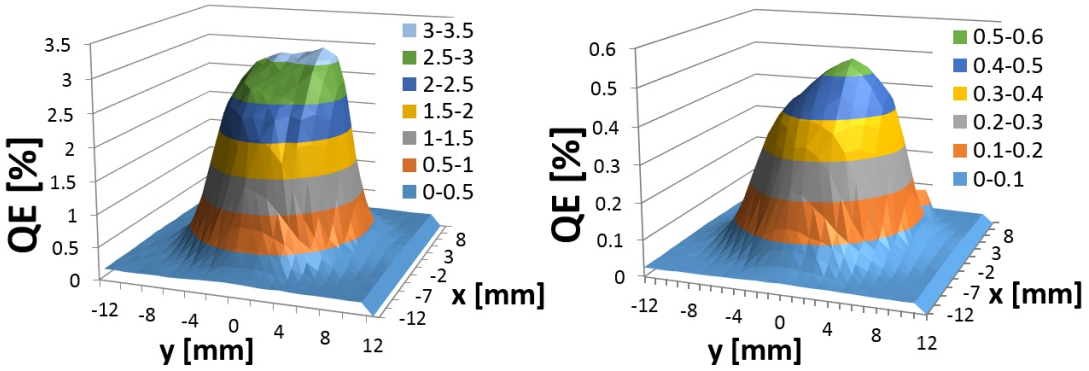

Figure 4.7: QE maps of cathode #202: (a)as newly produced, (b)after lifetime measurement at high average current in the DC gun setup

The better performance of cathode #202, instead, are probably related to the thicker photoemissive layer (Table 3.5) which seems to result in a more robust photocathode.

Cathode #192 (Fig. 4.6(b)), moreover, exhibits a peak with QE=0.08% in the middle, where the laser beam hits the surface, with transversal dimensions comparable with the estimated laser beam spot size. One possible explanation of this peak might be a laser cleaning process, which is in competition with the QE degradation. The same behaviour was already observed during high current electron beam production with Cs_2Te and UV laser beam in the same setup (101). The same feature is not evident in the QE map of cathode #202 as used (Fig. 4.7(b)), probably because the cathode as newly produced (Fig. 4.7(a)) did not show a flat top QE surface .

4.2 Tests in the PHIN RF photoinjector

The high charge PHIN RF photoinjector (102) is used as an off-line test stand for feasibility studies for the CLIC drive beam photoinjector. Being designed as a source for the CTF3 drive beam, the nominal parameters of PHIN (Table 1.1) are high bunch charge of 2.3 nC bunch charge, long pulse trains of 1200 ns and a short bunch spacing of 666 ps. Several Cs_3Sb cathodes were studied in the PHIN photoinjector to characterize their fundamental properties such as QE, operational lifetime and dark current, as detailed in the following sections.

4.2.1 PHIN photoinjector setup

Fig. 4.8 and Fig. 4.9 show a sketch and the 3D drawing of the PHIN RF photoinjector setup, respectively.

The electron gun is a 2.5 cell copper cavity with resonance frequency 3 GHz (S-band). The cathode is inserted into the backplane of the cavity which is surrounded by two solenoids. The main solenoid (2^{nd} solenoid in Fig. 4.8) is used for focusing the electron beam in order to compensate the space charge induced emittance growth. The bucking coil (1^{st} solenoid in Fig. 4.8), instead, compensate the magnetic field of the main solenoid in order to ensure that the electron bunch leaves the magnetic focusing region without any remaining average angular moment.

The PHIN gun is coupled to a klystron (RF power source) which is shared with another CTF3 probe beam photoinjector CALIFES (3). Therefore the PHIN photoinjector can only be operated during the shut down period of the CLIC Test Facility. The RF gun is water cooled at 33.5°C: as the thermo-mechanical deformations could lead to

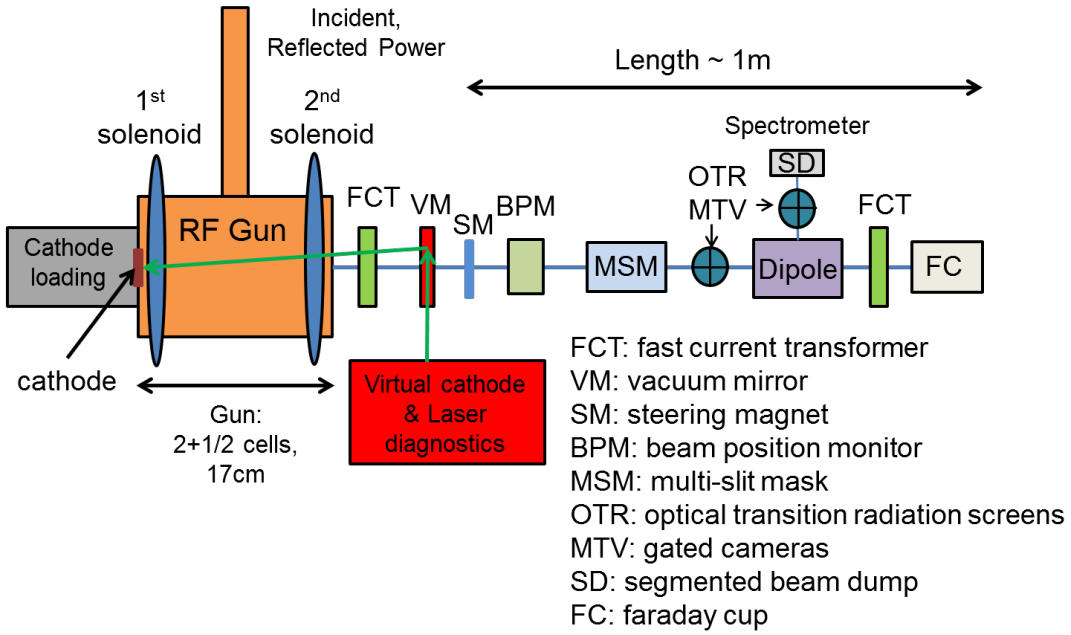

Figure 4.8: The PHIN RF photoinjector layout as in 2014

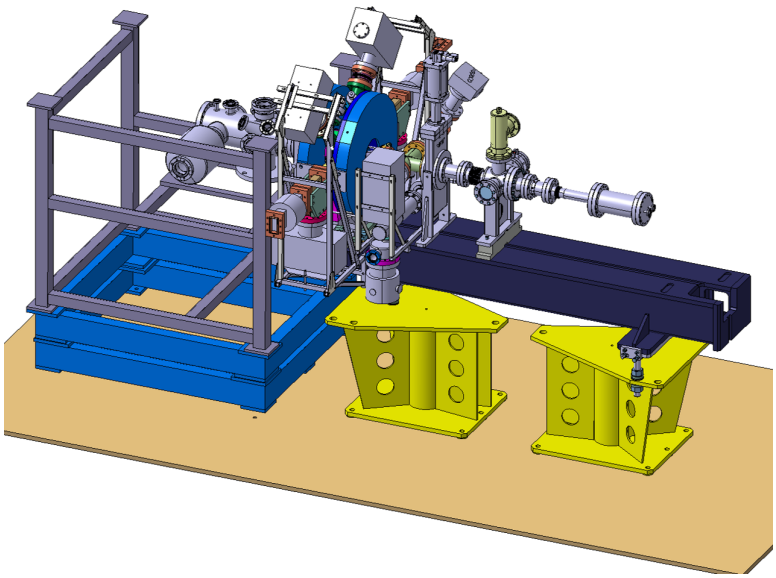

Figure 4.9: The PHIN RF photoinjector (3D drawing)

resonance frequency shift, this temperature was chosen for an optimized cavity tuning. The nominal peak gradient is 86 MV/m, even if up to 100 MV/m can be reached. As already mentioned in Chap. 2.1, RF breakdowns are a common phenomenon limiting the operation of high gradient RF accelerating cavities. The conditioning, established as a standard procedure for all the high field accelerating structures, is performed by increasing slowly the pulse length at low power level and then by increasing the power up to the maximum value (more details can be found elsewhere (30)). During this procedure, which causes controlled RF breakdowns, the nucleation sites left from machining and thermal treatments are vaporised. Each time the cathode is exchanged in the PHIN gun, a conditioning is required during which the operational RF peak gradient and pulse time duration are reached step by step.

PHIN laser system

The laser beam defines the temporal and transversal profiles of the electron beam. As already mentioned, the PHIN laser system (7) consists of a commercial (from High Q Laser GmbH) passively mode-locked Nd:YLF oscillator synchronized with the 1.5 GHz RF reference signal, a preamplifier, two diode pumped Nd:YLF amplifier stages and frequency conversion stages for green (2^{nd} harmonic) and UV generation (4^{th} harmonic). The oscillator and the preamplifier provide a continuous 1.5 GHz train of 10 ps pulses, while the two amplifiers are operated at the pulse rate of 0.8-5 Hz in correspondence with the klystron repetition rate (machine timing). The duration of the high energy trains of amplified pulses is 300-400 µs, as defined by the pulse duration of the pumping diodes. A BBO Pockels cell, driven by the machine timing, is used to cut the trains of IR pulses of desired duration (macro-pulses, up to 1.2 µs) for the generation of the 2^{nd} and the 4^{th} harmonic. During the cathodes studies presented in this thesis, the phase-switching setup (6) was not used. Aiming to stabilize the intensity within the train, a feedback stabilization system was installed in 2013 (103). The laser beam spot size, instead, is optimized for each specific electron beam parameters (Sec. 4.2.2) as well as the laser spot position on the cathode.

The laser beam is transported in air from the upstairs laser room to the table next to the photoinjector, where the optical setup for the monitoring and diagnostics of the laser beam at the "virtual cathode" is installed. The laser path continues through a vacuum viewport (with an anti-reflection coating for UV) to reach the cathode after

being deflected by a mirror installed inside the vacuum chamber. The laser macro-pulse and the RF pulse must overlap in time. It is possible to introduce a given phase difference between the RF field and the laser trigger. This leads to a difference in phase between the RF longitudinal field and the electron trains so that, for instance, the electrons see the maximum amplitude of the RF longitudinal field, when they are emitted from the cathode, if the "on-crest phase" is selected. Nonetheless the photoinjector is normally operated in "beam loading compensation" mode (Fig. 4.10). During the beam acceleration the electron beam absorbs energy from the RF field but can also deliver energy to the accelerating mode in the cavity. Beam loading compensation is achieved by changing the beam timing in order to have a flat loaded acceleration field and therefore a mono-energetic beam (104).

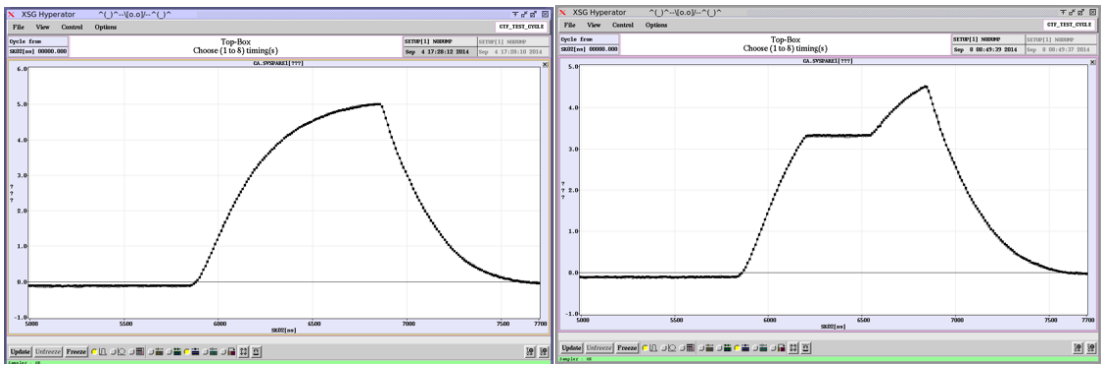

Figure 4.10: Antenna signal from the RF gun as seen on the control pc (Arbitrary unit over time): (a)without beam, (b)with beam (2.3 nC/bunch, 350 ns train length) in beam loading compensation

Beam instrumentation

The 1 meter long beam line is equipped with many devices needed to characterize the produced electron beam (Fig. 4.8). The first FCT (with a bandwidth of 1.6 kHz - 580 MHz) is used, as in the DC gun setup, to measure the electron beam charge, from which the QE is calculated. The beam is normally dumped in the FC, which is also monitoring the bunch charge. The FC measurements, as well as the ones of the second FCT (FCT-LD-50:1, Bergoz Instrumentation with a bandwidth of 0.32 kHz-650 MHz), can be used to estimate the beam losses in the beam line and eventually optimize the transport adjusting the phase, the steering magnets and the focusing solenoid.

An OTR profile monitor (Optical Transition Radiation screen coupled with a gated camera (105)) is used in combination with the steering magnets, to control both the vertical and the horizontal position, and in combination with the focusing solenoid, to optimize the beam transversal shape. Figure 4.11 shows the image produced by the OTR profile monitor when an electron beam is intercepted by the screen.

The multi-slit mask (labelled as MSM in Fig. 4.8) was designed and implemented to characterize the transverse normalized emittance. The spectrometer line is equipped with a profile monitor and a segmented beam dump. This OTR profile monitor is used to reveal the beam position in order to optimize consequently the dipole current. The beam dump, instead, is able to measure the electron beam energy and the energy spread. The experimental characterization of these instruments and the numerical studies can be found in an other PhD thesis (106) and will not be treated in this work.

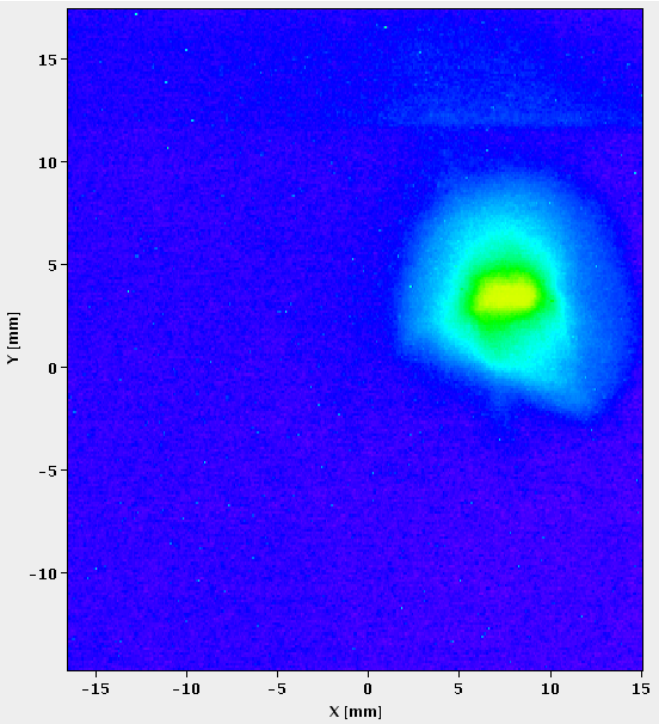

Figure 4.11: The electron beam (2 nC/bunch, 350 ns train duration) as seen by the OTR screen and the gated camera

Vacuum system

Up to 4 photocathodes can be transported from the photoemission laboratory to the PHIN photoinjector using a movable UHV transport carrier. After the transport carrier connection, the intermediate volume is then pumped before the cathode is transferred inside the RF gun.

The photocathode performance, and in turn the photoinjector one, are strongly influenced by the vacuum condition. In addition to the turbomolecular pumps, used in case of venting of the system, there are 10 sputter-ion pumps installed in the PHIN setup. The activation of the NEG (Non Evaporable Getter[1]) coating of the chamber surrounding the gun led in 2012 to an improvement of the dynamic vacuum level of almost one order of magnitude (down to 7×10^{-10} mbar). In 2013, an additional NEG cartridge (SAES getters Capacitorr D1000) was installed at the exit of the gun to further improve the vacuum level (Sec. 4.2.3). Moreover, several Bayard Alpert gauges and the combination of Pirani-Penning gauges allow to measure the vacuum level in different pressure ranges. A new RGA (Granville-Phillips 835 VQM) was installed in 2013 in the gun vacuum sector. Despite its controller electronics are placed outside the accelerator hall, this device cannot be operated during beam production as it is disturbed by the solenoids magnetic field. The impact on the vacuum of the beam operation was nonetheless measured taking the RGA spectrum right after turning off of the laser and the solenoids, as discussed later (Sec. 4.2.3).

4.2.2 Space charge effect

In a photoinjector, space charge is a relevant phenomenon at the cathode due to the combination of the almost zero electron kinetic energy and the surface charge distribution that the electrons experience as they are extracted (108). If the charge density is too high, the produced electric field can balance the accelerating RF field and limits

[1]NEGs are porous alloys that, when activated (heated in vacuum or inert gas atmosphere) show a very active metallic surface (107). The adsorbed gases diffuse into the bulk of the getter material upon heating. The getter material can be deposited directly onto the chamber walls acting as a distributed pumping system. The residual gases interact differently with the getters: hydrogen and its isotopes diffuse rapidly into the bulk, other gas molecules (as CO, CO2, O_2, N_2) are chemisorbed irreversibly, H_2O and hydrocarbons are cracked on the surface and adsorbed (hydrocarbons adbsorption is efficient at temperature$>$ 400°C) while noble gases are not adsorbed at all.

the amount of produced charge. The decelerating field E_{dec} is linked to the extracted charge Q as below (108):

$$E_{dec} = \frac{\rho}{\epsilon_0} = \frac{Q}{2\pi\epsilon_0\sigma_x^2} \tag{4.1}$$

where ρ is the peak charge density of a Gaussian distribution, ϵ_0 is the permittivity of the vacuum and σ_x is the size of the laser spot on the cathode. It has been shown that the extracted charge yield linearly increases with the accelerating field (106). In order to be able to extract electrons, the decelerating field has to be smaller than the accelerating RF field E_{acc}. In practical units, the maximum extractable charge can be estimated as below (108):

$$Q_{max}[nC] = \frac{E_{acc}[MV/m]\sigma_x^2[mm]}{18} \tag{4.2}$$

The laser spot size should be determined by a compromise between the maximum achievable charge and the minimum achievable transverse normalized emittance, which increase drastically with the laser spot size (106). When changing the beam parameters, it is normal practice to check whether the photoemitted charge is saturated, as done for the measurements in the DC gun setup (Fig. 4.1), and choose consequently the beam spot size.

4.2.3 Operational lifetime studies

In the PHIN photoinjector the QE evolution over time is measured for continuous beam operation at fixed beam parameters (train length and bunch charge) to extrapolate the cathode lifetime. The electron beam current is kept constant by adjusting the laser pulse energy to compensate the QE decrease.

Cesium telluride cathodes were extensively studied in the PHIN photoinjector in recent years (41). The correlation of non optimal vacuum conditions and short lifetime was clearly shown and the vacuum system upgrade of 2011 (NEG coating activation) led to a significant lifetime improvement: from 38 to 250 hours (41).

Cathode #198 (Cs_2Te) was used for producing an electron beam with 2.3 nC bunch charge and 350 ns macropulse duration.

The QE data, displayed in Fig. 4.12, is well represented by a double exponential decay[1] leading to a lifetime of 304 (± 20) hours. The second step of the vacuum system upgrade (addition of the NEG cartridge) led to a better dynamic level (P$\sim 2\times10^{-10}$ mbar, as shown in Fig. 4.12). Nonetheless, the lifetime value is similar to what was measured in previous tests on cesium telluride cathodes (41).

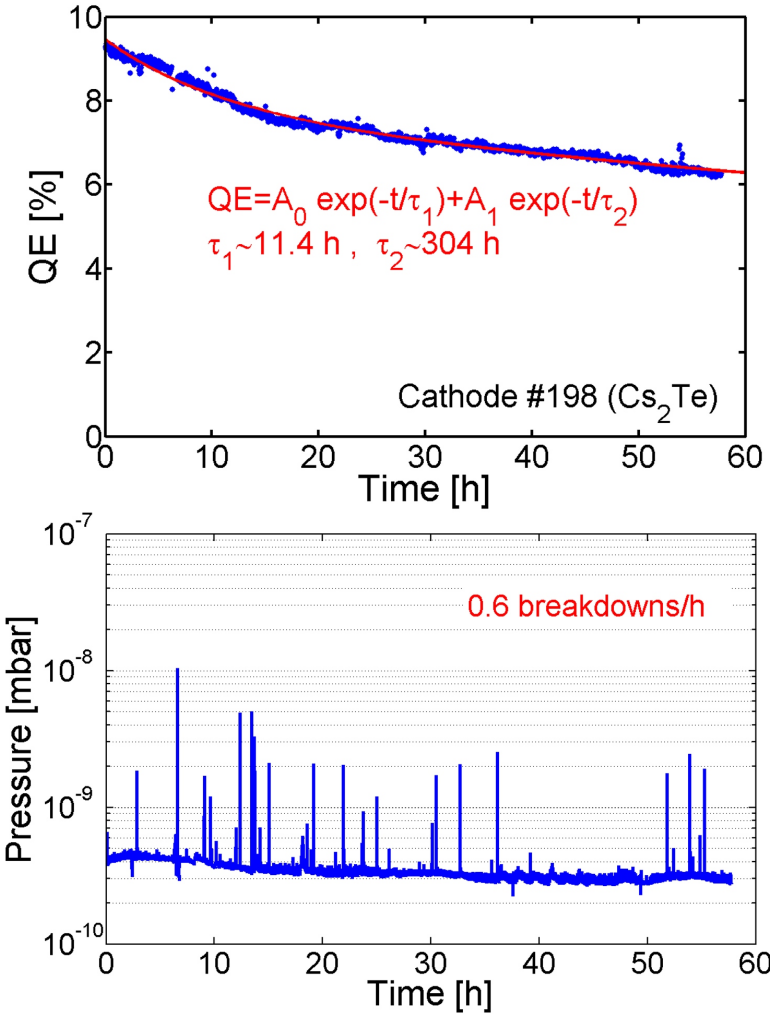

Figure 4.12: Measurements of the quantum efficiency and vacuum level as a function of time for 2.3 nC/bunch and 350 ns train length (cathode #198, Cs_2Te)

[1]Fresh Cs_2Te cathodes normally show a faster QE decay in the first hours of beam production, followed by an exponential decay dominated by a longer time constant (40). This behaviour is believed to be associated to the poisoning effect that oxygen has on this compound: after a fast drop, the QE reaches a saturation due to a sort of surface passivation (35).

Cathode #199 (Cs_3Sb) was tested for the same beam parameters as cathode #198. During the lifetime measurement on cathode #199, the vacuum level was slightly worse (P$\sim 4\times10^{-10}$ mbar) but the breakdowns rate was similar, as shown in Fig. 4.13. The QE of cathode #199 decreased rapidly from 2.8% to 0.8% in less than 50 hours (Fig. 4.13).

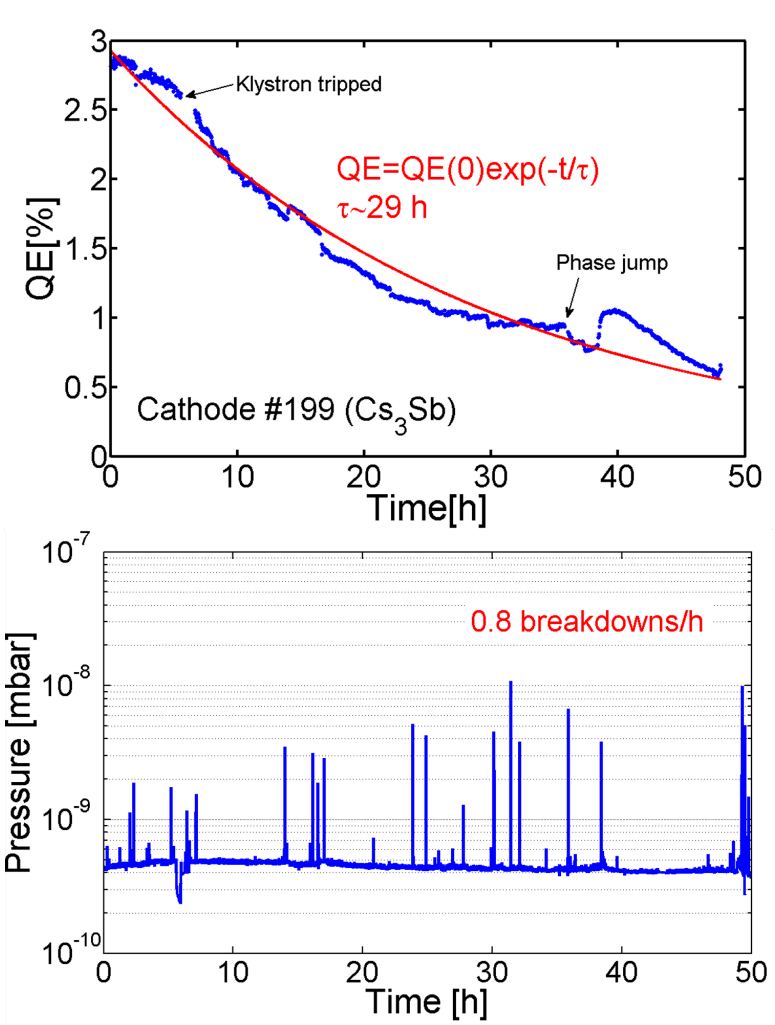

Figure 4.13: Measurements of the quantum efficiency and vacuum level as a function of time for 2.3 nC/bunch and 350 ns train length (cathode #199, Cs_3Sb)

During this lifetime measurement both a jump of the RF field phase relative to the laser timing and a sudden malfunctioning of the klystron, changed drastically the slope of the curve as indicated in Fig. 4.13. Probably due to these incidents, the data are not well fitted by an exponential decay as usual. The extrapolated 1/e lifetime, to be

used as a comparison value, is 29 hours.

For similar vacuum level and the same beam parameters, Cs_2Te cathodes showed lifetimes 10 times longer than cathode #199 (Cs_3Sb). The reason of the different performance of the two materials might be related to higher reactivity (e.g. faster oxidation) to the residual gases associated with the cesium antimonide (discussed further in Chap. 5). Moreover, also the "radiation damage" deteriorating processes (Fig. 4.5) are involved in the cathode degradation. RF breakdowns, already introduced in Sec. 2.1, are complex phenomena. During a breakdown, which are believed to be initiated by field emission, also the creation of a plasma is involved (27). Both ions and electrons associated to a breakdown, may be accelerated back-stream, depending on the phase of the RF pulse, and eventually bombard the cathode surface. A possible explanation of the much faster QE decay of cathode #199 is that the operational incidents (phase jump, klystron malfunctioning) led to stronger breakdowns, in terms of number of ions and electrons impacting on the photoacthode surface.

Another lifetime measurement was performed with the already used (Sec. 4.2.5) cathode #200 for bunch charge of 1 nC and train length of 800 ns. The QE evolution over time is shown in Fig. 4.14

After the phase jump, as in the case of cathode #199, the QE slope changed abruptly. Part of the data can be fitted with a single exponential decay, leading to a 1/e lifetime of 48 ($\pm$ 0.3) hours. The background pressure for a bunch charge of 1 nC (Fig. 4.14) is the lowest among the lifetime measurements discussed in this section. This observation is consistent with previous studies (41) that showed that the higher the bunch charge the higher the pressure, probably due to beam losses inside the gun. Although during the operation with cathode #200 the pressure bursts related to breakdowns had a higher intensity and the breakdown rate is similar, this cathode showed a slightly longer operational lifetime than cathode #199. However, a breakdown event may or may not lead to the bombardment of the photocathode and therefore even higher vacuum sparks could eventually have a less strong impact on the QE deterioration.

Both cathodes, even if characterized by a thick photoemissive film (Table 3.5), showed a rapid QE degradation. The non-optimal operational condition (phase jump incidents) could have plaid a role for example initiating stronger breakdowns. As a

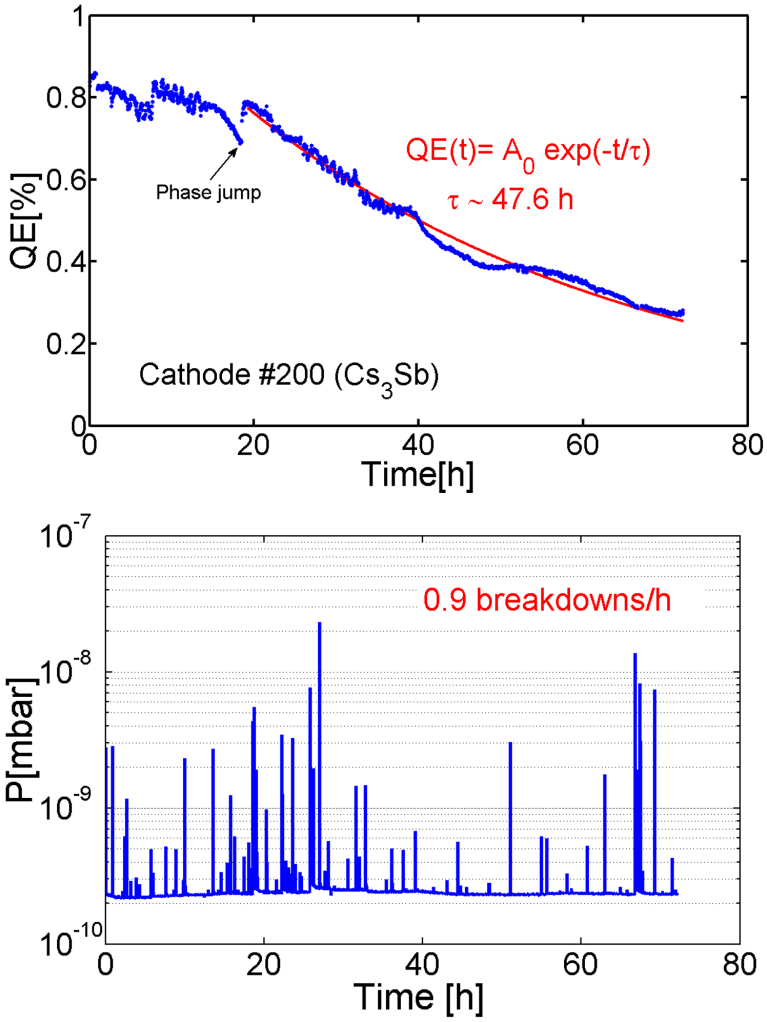

Figure 4.14: Measurements of the quantum efficiency and vacuum level as a function of time for 1 nC/bunch and 800 ns train length (cathode #200, Cs_3Sb)

result, cesium antimonide cathodes tested in the PHIN RF photoinjector showed a much shorter lifetime than cesium telluderide cathodes.

The cesium antimonide cathode tested in the DC gun beam line for the same beam average current as cathode #199 (Fig. 4.2) showed a lifetime 18 times longer. The higher dynamic vacuum level of the PHIN RF photoinjector with respect to the low pressure ($P<10^{-11}$ mbar) of the DC gun beam line has certainly a stronger impact on the cathode performance. Moreover, as shown in Fig. 4.13, the RF breakdowns are common events during the operation of the PHIN photoinjector. The pressure bursts associated to these phenomena play a role in the QE degradation. In addition, the breakdowns might result in back bombardment processes that could contribute to the cathode deterioration, damaging locally the deposited layer (as discussed in Sec. 4.2.6). The different environmental conditions of the DC gun and the RF photoinjector, therefore, might lead to different predominant deteriorating effects (97, 99), as shown by the analysis of the QE maps (Sec. 4.2.6) and further investigated in Chap. 5, where the chemical composition of the used cathode surface is analysed.

In Fig. 4.15 the RGA spectrum displayed in blue shows the composition of the residual gases inside the PHIN gun as right after turning off the laser and the solenoids. This is the available data closest to the actual gas composition during beam operation, considering that the RGA spectra are affected by the magnetic field produced by the solenoids.

In the plot, the main mass peaks of the found residual gases are labelled. The peak at 28 a.m.u. is indicated as N_2/CO because both species have the same mass to charge ratio. It is in principle possible to separate the relative contribution (109). The highlighted gases (refer to the blue line spectrum of Fig. 4.15) are the species typically found in a well baked, leak-free vacuum chamber at pressure lower than 10^{-9} mbar. Hydrogen (H_2), water (H_2O)[1], carbon monoxide (CO) and carbon dioxide (CO_2) are the most common residual gases (82). The gas sources in a generic accelerator vacuum system are mainly the thermal outgassing from surfaces and dynamic effect, i.e. beam/dark current induced desorption phenomena. The mentioned species are dissolved in the metal and continuously escape. However, also methan (CH_4) and a very small quantity of oxygen (O_2) were detected. A relevant contribution to some residual gas species can be actually produced inside the ion sources of the measuring equipment:

[1] An extreme bake-out at temperature higher than 400°C is needed to remove water completely (82).

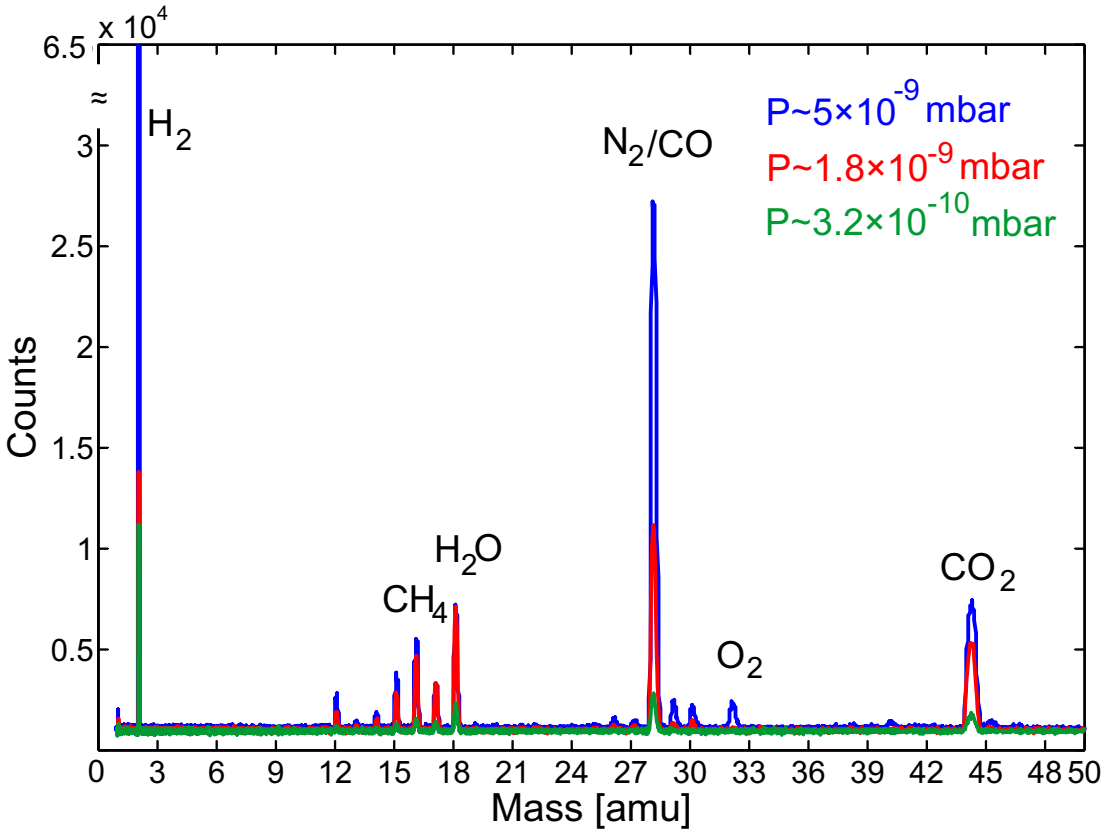

Figure 4.15: RGA spectra in the PHIN gun: right after beam production (blue line), after closing the valve to separate the gun vacuum sector from the beam line (red line), after 1 day of passive pumping (green line)

atomic hydrogen is formed on the hot tungsten filament and reacts with the carbon and oxygen (O_2) on the stainless steel electrodes surface, producing H_2O, CO_x and C_mH_n compounds (110, 111). As indicated by the legend of Fig. 4.15, the background pressure in the gun decreased right after isolating the gun sector, showing that the desorption contribution is mainly coming from the beam line. The hydrogen, oxygen and carbon monoxide peak intensity reduced rapidly (refer to the red line spectrum in Fig. 4.15). This trend is associated with the high pumping capability for H_2 and CO of the NEG coating together with the parallel action of the sputter-ion pumps. As already mentioned and further discussed in Chap. 5, these residual gases originating during the photoinjector operation can react with the cathode surface forming compounds such as oxides. After one day of passive pumping, the contribution from all the different gases was drastically reduced, as shown by the green line spectrum of Fig. 4.15.

4.2.4 Dark current measurements

As already mentioned in Chap. 1 the field emission is an non-desirable but inevitable phenomenon in both DC and RF gun. Therefore quantifying the dark current is an important matter when dealing with photoinjectors, especially for high peak gradient gun. The field emission has actually an effect on the electron beam dynamics (such as secondary electrons emission and multipacting, more details can be found elsewhere (112, 113, 114)) as well as on the cathode deterioration, as already mentioned in the previous sections.

The dark current, given by both the field emitted electrons from the cathode itself and the contribution coming from the RF gun walls, has been measured scanning the peak RF accelerating gradient from 70 MV/m to 100 MV/m (Fig. 4.16). The current intensity from field emission was measured with the Faraday cup, positioned 1 meter downstream from the gun (Fig. 4.8). For each measurement point, the solenoids and the steering magnets were tuned in order to optimize the electrons transport through the beam line .

The copper sample #6A56 as well as the substrates used for producing cathodes #199, #198 and #200 had a diamond powder polished surfaces (Sec. 3.2). As shown in Fig. 4.16, the current values measured with semiconductor cathodes are more than one order of magnitude higher than the measurements performed with the copper substrate, same material as the gun walls. This is an evidence that the main contribution to the

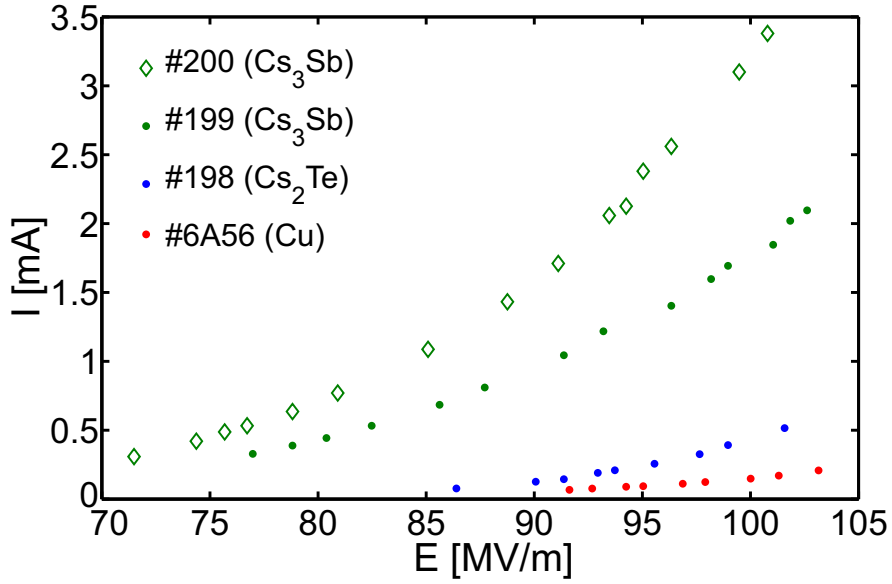

Figure 4.16: Dark current measurements in the PHIN photoinjector: current generated in the RF gun, without illuminating with the laser beam, for different values of the peak gradient and diverse cathode materials.

dark current is coming from the cathode itself and not from the gun walls. Cs_3Sb cathodes generated high current up to 3 mA for an intense accelerating gradient of 100 MV/m. For cesium telluride, instead, the maximum value of field emitted current is 0.5 mA. The different behaviour of the two materials is associated with their band diagram (Chap. 2). The smaller the potential barrier the electrons need to overcome (ϕ_{Cs_3Sb} ~2 eV, ϕ_{Cs_2Te} ~3.5 eV) the higher the contribution to the dark current.

The Fowler-Nordheim description of field emitted current for an alternating field is also proposed (27):

$$\overline{I}_F = \frac{5.7 * 10^{-12} \times 10^{4.52\phi^{-0.5}} \times A_e \left(\beta E_0\right)^{2.5}}{\phi^{1.75}} \tag{4.3}$$

where E_0 is the amplitude of the sinusoidal macroscopic surface field in V/m, β is the field enhancement factor[1], ϕ is the work function, $\overline{I}_F$ is the averaged field emitted current, integrated over an RF period, from an emitting area A_e.

[1]Several factors could locally enhance the electric field, such as the surface roughness, metallic dust, grain boundaries, molten craters after breakdown, adsorbed gases,etc..(27). However, normally, the enhanced field emission source is visualized as a microprotusion on the metallic surface.

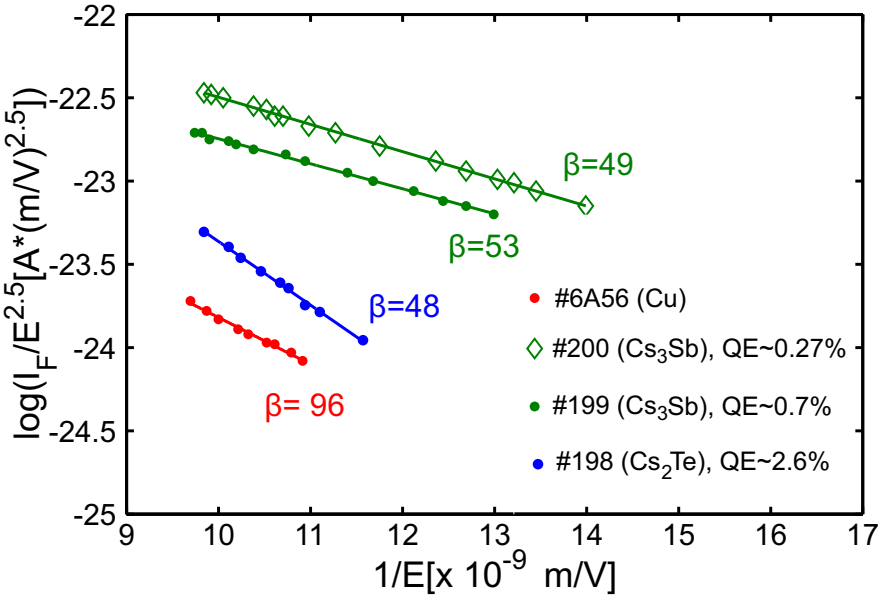

Figure 4.17: Fowler-Nordheim plot of the dark current measurements.

The extracted β value for Copper (Fig. 4.17) is consistent with the data in literature (27). For semiconductor photocathodes, the β values are extrapolated following the same procedure, but this analysis deserves a few more words. Firstly, while evaluating the β value from the slope of the curve, particular attention on the definition of work function has to be paid. As a matter of fact, the photoemission threshold, given by the energy difference from the vacuum level and the top of the valence band, was used in the calculation of the enhancement factor for consistency with the treatment of metals. Secondly, the Fowler-Nordheim theory has been formulated for metals, so the physical meaning always given to β value might not be completely justified for semiconductors. Nonetheless the Fowler-Nordheim plot (Fig. 4.17) is a useful visualisation of the dark current data.

The higher dark current originated by the cesium antimonide cathodes is not an issue for the CLIC drive beam generation since it is almost three orders of magnitude lower than the average current in the train (115). However, the higher field emission could originate more breakdowns and having, as a consequence, a negative impact on the cathode lifetime.

4.2.5 RF lifetime studies

In order to estimate the detrimental contribution related to the beam independent processes, the so called RF lifetime measurements were performed. The QE evolution of two different cathodes (#199, #200) was studied under 100 MV/m peak accelerating gradient and no continuous beam production (Fig. 4.18). The background pressure (P$\sim 3\times10^{-10}$ mbar) and the breakdown rates were similar during both measurements: 5.6 breakdowns/h for cathode #199, 7.8 breakdowns/h for cathode #200. The QE of cathode #199, tested after more than 50 hours of continuous beam production (Fig. 4.13), was rather stable over 90 hours. Each point was measured for 2.3 nC/bunch, 350 ns train length and beam loading compensated, tuning the phase for each point in order to optimize the beam transport.

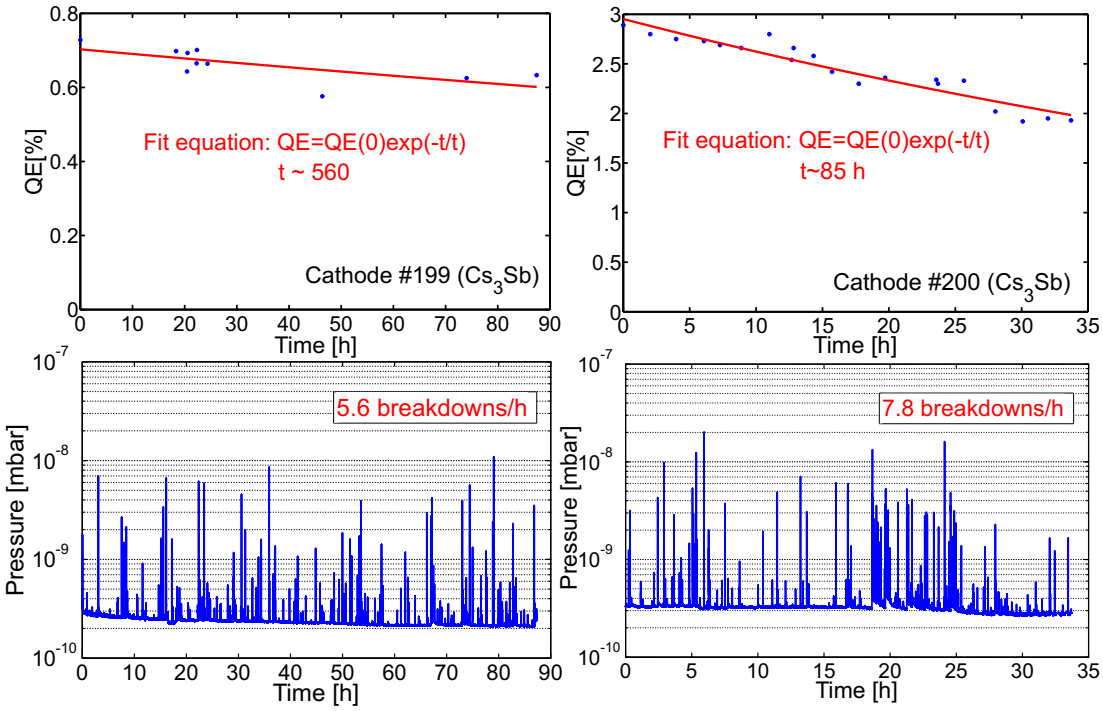

Figure 4.18: RF lifetime measurements on cesium antimonide cathodes: (a)QE and pressure level as a function of time for cathode #199, (b)QE and pressure level as a function of time for cathode #200

The fresh cathode #200 was measured in the same condition as cathode #199 but for lower charge (1.3 nC/bunch) in order to minimize the difference between unloaded and loaded gradient and try to reduce the numbers of subsequent induced breakdowns.

During RF lifetime measurements, cathode #200 showed a much faster QE decay, consistent with the usually observed behaviour for fresh cathode. Therefore, the high dark current of Cs_3Sb seems to give a remarkable contribution to the cathode deterioration, probably due to the deteriorating effects associated to the breakdowns (ions/electrons bombardment and vacuum sparks). One more argument to this explanation is found in the analysis of the QE maps in Sec. 4.2.6. It has to be pointed out that in normal operation the loaded peak gradient is lower than the unloaded gradient during the RF lifetime measurements. The maximum loaded gradient for nominal parameters is ~85 MV/m (106) leading to a minor dark current contribution (Fig. 4.16). As a matter of fact, the breakdown rates during the RF lifetime measurements were much higher than in the case of operational lifetime measurements.

4.2.6 Quantum efficiency maps analysis

Figure 4.19(b) shows the strongly deteriorated photoemissive properties of cathode #199: the original QE peak value of 5% reduced to a maximum value of 1% with valley at 0.2% after the tests in the PHIN RF photoinjector. The pronounced non-uniformity of the QE map (Fig. 4.19(b)), moreover, suggests that the impact of ions was involved in the degradation of the cathode surface. The damage produced by these phenomena is more localized than the oxidation, which is likely to be distributed over the whole cathode surface.

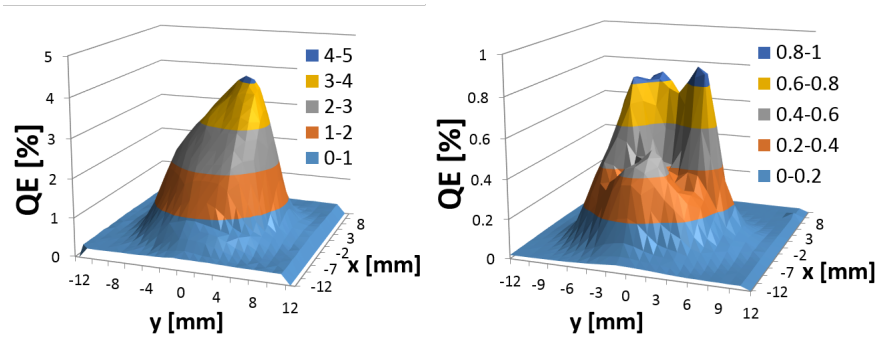

Figure 4.19: QE maps of cathode #199 (Cs_3Sb): (a)as newly produced, (b)after tests in the PHIN RF photoinjector

The ions bombardment seems to have been effective also in deteriorating the photoemissive properties of cathode #200 (Fig. 4.20) and cathode #198 (Fig. 4.21), even

if the QE maps of these used cathodes are less indented.

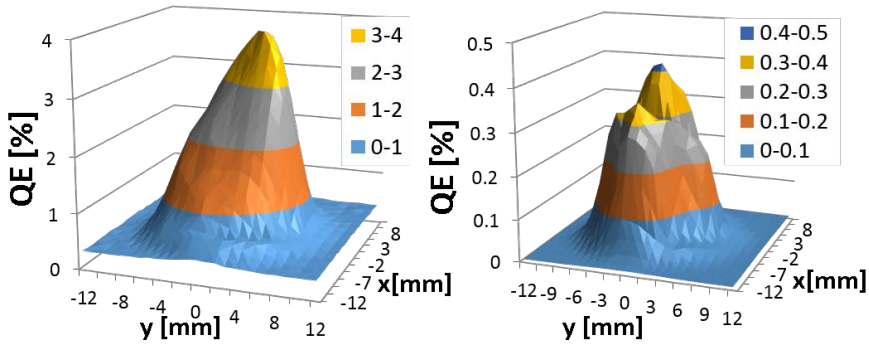

Figure 4.20: QE maps of cathode #200 (Cs_3Sb): (a)as newly produced, (b)after tests in the PHIN RF photoinjector

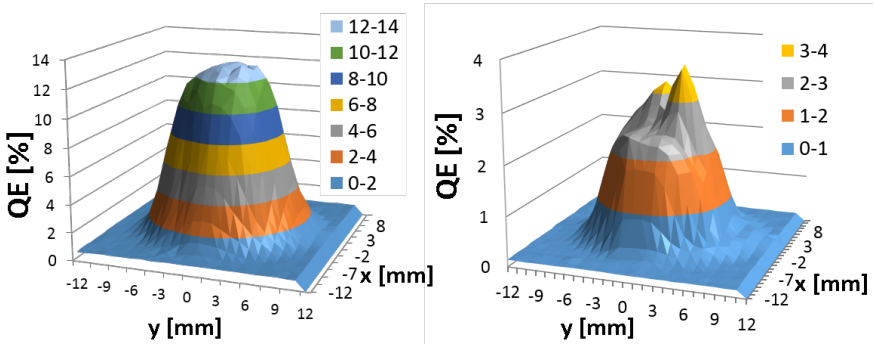

Figure 4.21: QE maps of cathode #198 (Cs_2Te): (a)as newly produced, (b)after tests in the PHIN RF photoinjector)

The appearance of these QE maps is much different than the ones shown in Fig. 4.6 and Fig. 4.7, associated with the tests in the DC gun setup. In addition to the ions (originated by the interaction of the electron beam with the residual gas) back bombardment, the breakdowns are likely to give a big contribution to the "radiation damage" processes in the PHIN RF photoinjector. The dark current increases exponentially with the electric field (Fig. 4.16), therefore under the influence of the high electric peak gradient, many field emitted electrons will be produced in the PHIN RF gun, possibly initiating breakdowns. This assumption is further supported by the high breakdown rates seen during both operational and RF lifetime measurements, whereas only few pressure sparks were observed during the operation of the DC gun beam line

with Cs_3Sb photocathodes. Therefore, the PHIN RF gun is a more challenging environment for the cathode mainly due to the frequent breakdowns that strongly limit the cathode performance.

Chapter 5

X-ray Photoelectron Spectroscopy studies of photocathodes

The X-ray Photoelectron Spectroscopy (XPS) is an excellent technique for determining the composition of the photocathode surface giving also information on the chemical state of the elements. Many XPS studies can be found in the photocathodes R&D literature (21, 35, 58, 59), where the authors probed the cathode surface at different steps of the growth process or after a controlled exposure to oxygen. In this chapter detailed studies of both Cs_3Sb and Cs_2Te cathodes as newly produced and used, in different installations (DC gun setup and PHIN RF photoinjector), will be presented. The aim of such analysis is to find a cross-correlation between the overall quantum efficiency and the chemical composition of co-deposited photocathodes as well as to investigate the material evolution during beam production and consequent cathode deterioration.

5.1 A brief introduction to the XPS technique

Since the quantum theoretical explanation of the photoelectric effect by Einstein in 1905, it was clear that the energy of the emitted photoelectron contains information of the solid from which it is emitted (116). Rutherford and coworkers, in 1914, recognized that the kinetic energy of the photoelectron is the difference between the X-ray

energy and the electron binding energy, but the first XPS spectra with high resolution was obtained far in the 1950's, after the development of precision electron spectrometers. The main features of XPS, that this technique has in common with the Auger Electron Spectroscopy (AES), are the detection of all elements except hydrogen and helium, detection of chemical bonding states and information depth in the nanometer region. The basic components are an UHV based stainless steel chamber containing the sample stage, an X-ray source (with or without a monochromator), the electron energy analyzer and the detection system. In XPS, the surface of a sample is irradiated with photons of a characteristic energy (depending on the X-ray source type). These photons interact with the core electrons of the sample atoms creating ionized states. A photoelectron is subsequently emitted with a kinetic energy approximately equal to the difference between the photon energy and the binding energy. The measured photoelectrons spectrum is a direct indication of the binding energies of the different atomic electron levels. Therefore, the XPS technique allows elemental identification. Moreover, as the differences in the chemical potential and polarizability of compounds lead to variations in the elemental binding energies, the resulting chemical shifts can be used to identify the chemical state of the materials being analysed. The information depth is limited to the nanometer region by the probability of suffering energy loss (the "inelastic mean free path" which is in the range of nanometers (117) for both conductors and semiconductors). In addition to the qualitative analysis, the XPS technique allows quantitative studies: the relative elemental composition of the sample surface can be calculated. The peak intensity I_A is, in fact, proportional to the concentration (n_A) of the element A through the equation (118):

$$I_A = \sigma_A \times \lambda_A \times K \times n_A \tag{5.1}$$

Where σ_A is the photo-ionization cross section of the element A, λ_A is the mean free path of the photoelectron in the sample and K_A includes all the setup related factors (e.g. the analyser transmission function). The determination of the Sensitivity Factor (SF=$\sigma_A \times \lambda_A \times K_A$) for each element and the specific setup configuration is normally done experimentally with pure element standards. However, it has to be pointed out that for a very accurate quantification, the sensitivity factors should be corrected in many circumstances (heterogeneous samples, transitions metals in different chemical states, etc..). More details can be found elsewhere (116, 118).

5.2 XPS studies on co-deposited cathodes

Both co-deposited Cs_3Sb cathodes and Cs_2Te, as newly produced and after usage, were analysed, within the scope of this thesis, to study the different performance from the compositional point of view.

5.2.1 Experimental setup

A UHV transfer vessel (Fig. 5.1), originally designed by LAL (Laboratoire d'Accélérateur Linéaire, Orsay) and built in a collaboration between LAL and CERN to be compatible with the CERN XPS setup, was commissioned in 2014. This UHV vessel, also called transfer arm, allows to transport one cathode per time from the preparation chamber (detailed in Chap. 3) to the XPS laboratory, providing also the needed support as sample holder during the collection of the XSP spectra. After each disconnection and connection, the intermediate volume is pumped and baked to prevent the cathode from contamination. Therefore around two weeks of time are needed to exchange the cathode to be analysed.

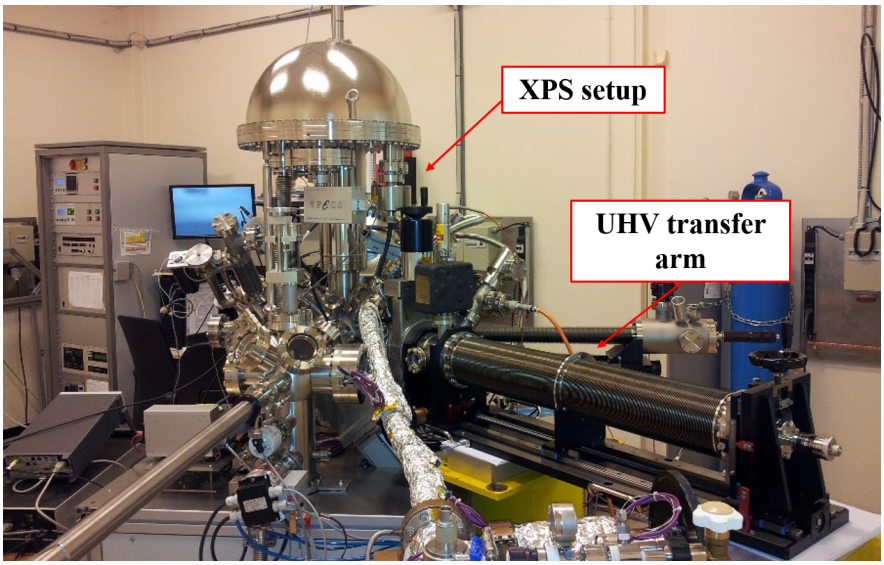

Figure 5.1: The UHV transfer arm attached to the XPS setup

The XPS spectra were collected by a commercial system (SPECS GmbH) equipped with a hemispherical energy analyser (Phoibos 150) and a monochromatized Al x-ray source. The average pressure in the XPS analysis chamber is P$\sim 5\times10^{-10}$ mbar. The

energy scale is calibrated with the position of the Cu $2p_{3/2}$ and Au $4f_{7/2}$ lines. The sensitivity factors used for quantitative analysis were taken from a Standard Reference Database published by the NIST (National Institute of Standard Technology of U.S.) and the transmission function for the specific instrument was taken into account. The correspondence with experimental data obtained by using such a procedure was checked for several pure elements (Au, Cu, C, Si, Al, Ag, Mo, Ni, Nb and Co). Moreover, an experimental calibration for the sensitivity factor of cesium was done using a pellet of CsCl. This sample was analysed with the XPS setup and, assuming a Cs to Cl ratio of 0.5, the Cs sensitivity factor was corrected accordingly[1]. As previously mentioned, in order to have an extreme accurate quantification, the sensitivity factors should be adjusted for each specific case. Nonetheless, the calculated relative elemental compositions can be useful for semi-quantitative considerations.

5.2.2 Analysis of cesium antimonide cathodes

Two different cesium antimonide cathodes were analysed with the XPS in order to find a correlation between the chemical composition and their photoemissive properties (119). XPS studies were performed on cathode #202 as newly produced and after the lifetime measurements performed in the DC gun setup (Sec. 4.1). The surface of cathode # 199, instead, was probed only after the tests performed in the PHIN RF photoinjector (Sec. 4.2) as the malfunctioning of some part of the XPS setup did not allow to perform the measurements on the cathode at the time it was produced.

Measurements on cathode #202 (Cs_3Sb) as newly produced

Figure 5.2 shows the XPS wide range spectrum taken on the surface of Cathode #202 as grown together with the relative elemental composition of the detected elements. The analysis highlighted a contamination of oxygen. Moreover, the measured Cs to Sb ratio is 2, much lower than the optimal stoichiometry. It is known that Cs_3Sb is a p-type semiconductor in which acceptor levels are due to a slight excess of antimony (11). Nonetheless, the calculated stoichiometric ratio of cathode #202 indicates a stronger deficiency of cesium which is explained by the presence of a Sb-rich phase on the cathode surface, as shown in the peaks model proposed in Fig. 5.3. There are in fact many

[1]According tot the NIST Database the sensitivity factor changes because there is a big difference in the cesium electron mean free path value as in metallic cesium or as in a cesium-based compound.

stable Cs-Sb compounds, as stressed in the binary phase diagram (120), that are likely to be produced during the deposition process (9).

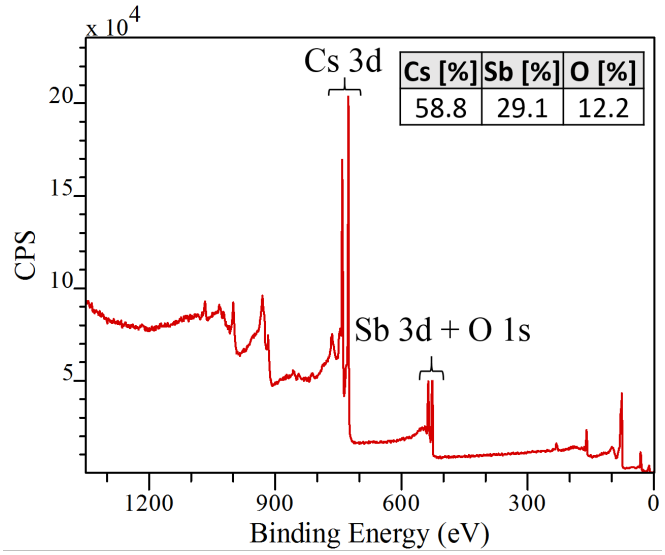

Figure 5.2: XPS measurements (Counts Per Second over Binding Energy) of cathode #202 (Cs_3Sb) as newly produced: wide range spectrum and relative elemental surface composition

A further argument to such explanation is that the maximum measured value of the QE at 532 nm is only 3.5% (Sec. 4.1, Fig. 4.7(a)), less than half compared to the best Cs_3Sb cathode produced at CERN with the same preparation setup and procedure (QE=7.5%, Table 3.5) and much lower than QE=20% obtained in photomultiplier applications (9).

The XPS measurement taken with high resolution in the energy region of the antimony 3d core levels, which exhibit the typical doublet pair structure due to the spin orbit splitting, shows the overlapping 1s core level of oxygen (Fig. 5.3). The fit of the experimental data shown in Fig. 5.3 is obtained by using Gaussian-Lorentzian peaks with fixed area ratio (1.5) between the two components of the doublet pair (Sb $3d_{5/2}$ and Sb $3d_{3/2}$) and cross-checking the resulting spin-orbit shift between each corresponding peak (about 9.3 eV). This allowed the identification of the oxygen contribution as the residual intensity. The following discussion will refer only to the most intense peak of any doublet pair for simplicity.

Two chemical states of antimony were identified (Fig. 5.3): Sb^{3-} (as in the com-

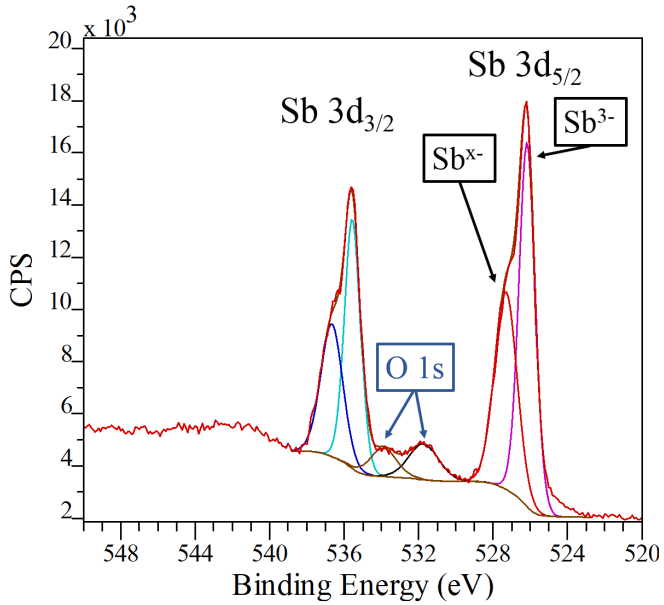

Figure 5.3: XPS measurement of cathode #202 (Cs_3Sb) as newly produced: high resolution spectrum of Sb3d + O1s region (red line: measured spectrum, brown lines: Shirley background, other colours line: fitting profiles, dark brown: overall fit-almost overlapping with the measured spectrum)

pound Cs_3Sb, peak at 526 eV) and a peak at 527.3 eV which is attributed to an alkali deficient Cs- Sb compound (labelled as Sb^{x-}, where x refers to the oxidation state which for this compound is unknown). The attribution of the peak at 526 eV is in agreement with Soriano et al. (121). A similar peak, as the Sb-rich phase one, is reported by Bates et al. (122) at 527 eV. Two oxygen peaks were identified under the broad shoulder: the peak at 531.7 eV, which was attributed to cesium sub-oxide (Cs_3O_{11}) already identified by other authors (121, 122), and a peak at 533.9 eV. Electrons from O 1s orbital of such high energy are normally related to adsorbed molecular water (123, 124). In baked UHV systems, as the ones in which the cathode was introduced, the partial pressure of water is very low. Nonetheless some molecules of water vapour can react with the alkali antimonide surface and be physisorbed.

A similar detailed study, inclusive of peaks models, of the chemical states of cesium is limited by the small chemical shifts of the core levels between Cs metal, Cs-Sb compound and Cs oxides (122). Therefore, only a qualitative analysis is proposed in this work. In Fig. 5.7 (red line), the cesium 3d levels are shifted towards lower

binding energy with respect to the free-metal (Cs $3d_{5/2}$=726.4 eV (118)), even if in the Cs-Sb compounds the alkali metal is transferring a large fraction of the electronic charge to the antimony. Such unusual behaviour was already observed in previous XPS analysis of alkali antimonide surfaces and it can be explained by the predominantly ionic character of the Cs_3Sb structure (122). The satellite broad peaks at the left of the main photoemissive peaks (Fig.5.7, red line), identified as plasmons, arise from the excitation of plasma oscillations of the valence band electrons by the motion of photoelectron in the solid. This pronounced feature was noticed to be associated with higher photosensitivity (122).

Measurements on cathode #202 (Cs_3Sb) after high average current measurement in the DC gun setup

The same cathode was probed with XPS analysis after the lifetime measurements at high average current in the DC gun setup (Sec. 4.1). Figure 5.4 shows the wide range XPS spectrum together with the elements found on the surface. Both oxygen and carbon were detected. The relative elemental composition gives a Cs to Sb ratio of 3.2, higher than the ratio measured on the new cathode surface. Nonetheless the cathode maximum QE decreased from 3.5% to 0.6% (Sec. 4.1).

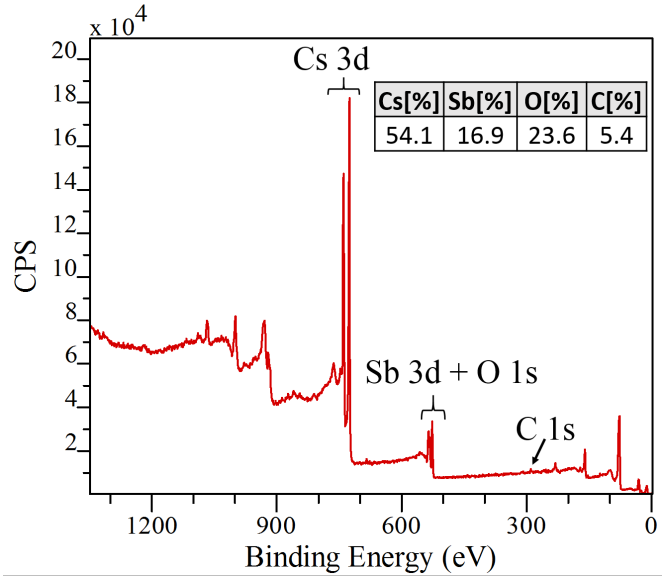

Figure 5.4: XPS measurements of cathode #202 (Cs_3Sb) as used: wide range spectrum and relative elemental surface composition

The peaks model proposed in Fig. 5.5 assumed that the same Sb compounds as found on the cathode surface as grown (Fig. 5.3) are still present on the cathode surface: the fitting peaks with the same position and the same width reproduce well the measured spectrum. The intensity of Sb 3d peaks as well as Cs 3d peaks (discussed later), instead, has decreased compared to the as grown cathode. This implies that the surface is covered with a contamination layer. Therefore, the formation of different compounds on the top layer could explain the different Cs to Sb ratio.

The carbon contribution is clearly visible from the high resolution spectra of the C 1s region displayed in Fig. 5.6, which is not the case on the as-grown cathode surface. Moreover, a huge peak associated with oxygen is visible at 532.45 eV (FWHM=2 eV) in Fig. 5.5. Degradation studies performed on multialkali antimonide cathodes under controlled exposure of CO_2, showed that this gas is effective in reducing the QE (47). A similar behaviour should be expected by Cs_3Sb cathodes. XPS spectrum of adsorbed CO_2 normally gives rise to O 1s peak at higher binding energy (533.7-535.5 eV (125)) than the position of the peak of Fig. 5.6. It is reported, instead, that some metals react to the exposure at carbon dioxide forming carbonates (126).

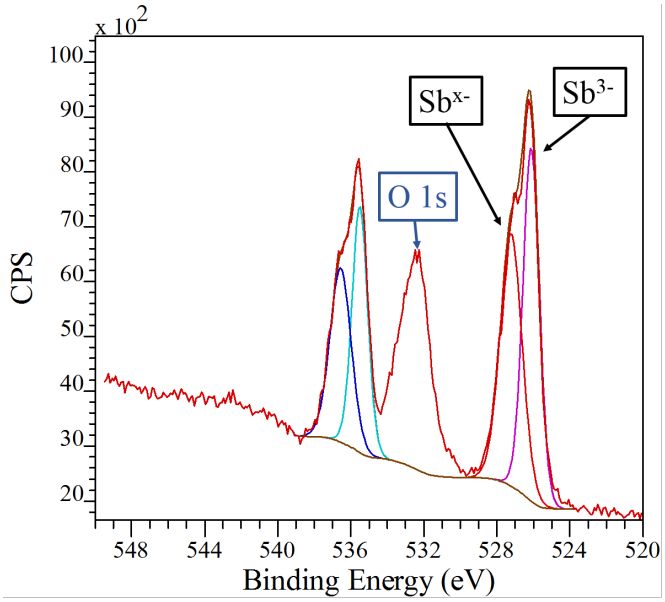

Figure 5.5: XPS measurement on used cathode #202 (Cs_3Sb): high resolution spectrum of Sb3d + O1s region with peaks model

Moreover, the position of the carbon peak (290.46 eV) is compatible with the C 1s

level of the carbonate ion (CO_3^{2-}) as found in literature (118). Therefore, it is likely that the cesium on the cathode surface has reacted with CO_2 forming cesium carbonates (Cs_2CO_3). The asymmetry of the broad peak labelled as O 1s in Fig. 5.5 suggests the coexistence of different chemical states of oxygen. Therefore, it is not excluded that, in addition to the cesium carbonate, also Cs_3O_{11} or H_2O or both compounds, as already found on the as grown-cathode surface, are present on the used cathode surface.

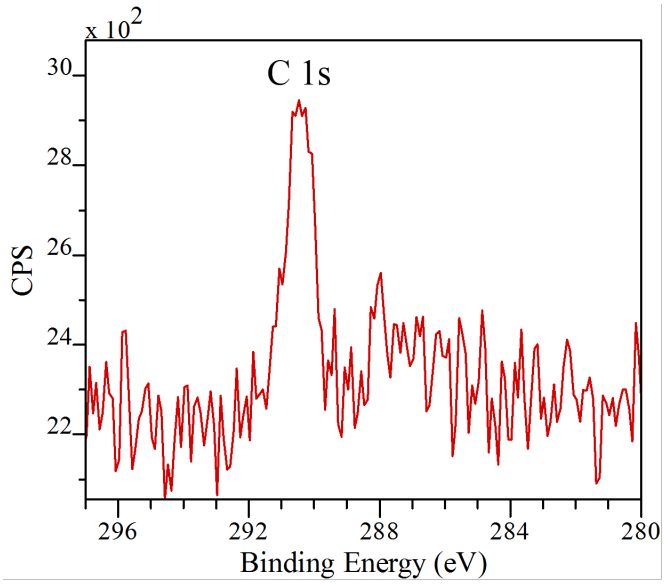

Figure 5.6: XPS high resolution spectrum of C 1s region on used cathode #202 (Cs_3Sb)

One more argument comes from the analysis of the high resolution XPS spectra of Cs 3d region displayed in Fig. 5.7 with green line. The Cs doublet pair is shifted towards higher binding energy compared to the measurements on the cathode as newly produced, shown in red in the same plot. The bigger peaks width (FWHM=2.2 eV compared to the 1.6 eV for the newly produced cathode) and the less pronounced plasmons structures are also indications of non-identical composition due to the formation of different Cs chemical states on the cathode surface. The same tendency was observed on alkali antimonide photoemitters after the heating induced degradation of their photosensitivity (122). In this study, the changes in the XPS high resolution spectra are specifically ascribed to the formation of the cesium carbonate.

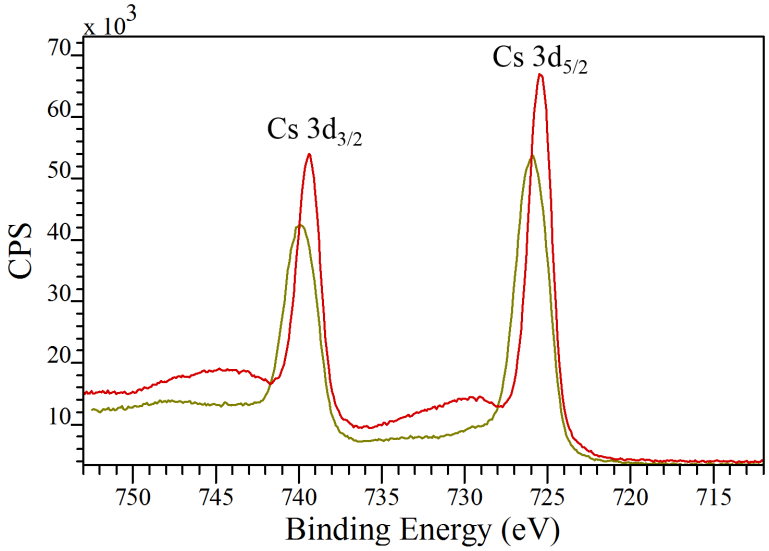

Figure 5.7: XPS high resolution spectra of Cs 3d region on cathode #202 (Cs_3Sb) as newly produced (red line) and as used (green line)

Measurements on cathode #199 (Cs_3Sb) after tests in the PHIN RF photoinjector

Cathode #199 showed an average QE of 5.2% as newly produced. After the tests performed in the PHIN RF photoinjector (Sec. 4.2), its photoemissive properties were strongly deteriorated as shown in Fig. 4.19 (b).

The wide range XPS spectrum shown in Fig. 5.8, was taken on the surface of the cathode after usage. Quantitative analysis of cathode #199 showed a strong deficiency of cesium compared to the desired compound Cs_3Sb: the Cs to Sb atomic ratio is 1.9. Moreover, oxygen contamination was detected.

The high resolution XPS spectrum in the region of Sb 3d and O 1s core levels, with the result of an accurate fitting procedure, is shown in Fig. 5.9. This peaks model is interpreted as the occurrence on the cathode surface of four different chemical states of antimony. The most reasonable assignment of the peak at lower binding energy (525.9 eV) is to Sb^{3-} species as in the compound Cs_3Sb, in agreement with the analysis done on cathode #202. The other two antimony components are attributed to an alkali-deficient Cs-Sb compound (peak at 527 eV, as already explained in the previous sections) and to metallic antimony (Sb^0 at 527.9 eV, in good agreement with literature values (118)). Part of the antimony is bound as the oxide Sb_2O_3: well apart

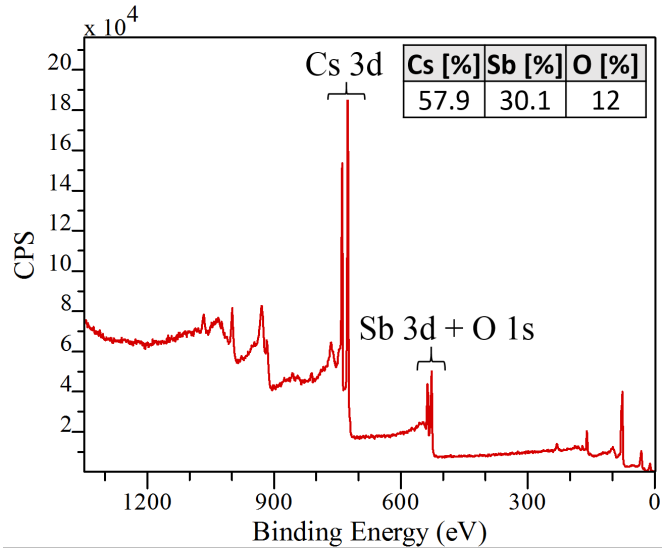

Figure 5.8: XPS measurements on used cathode #199 (Cs_3Sb): wide range spectrum and relative elemental surface composition

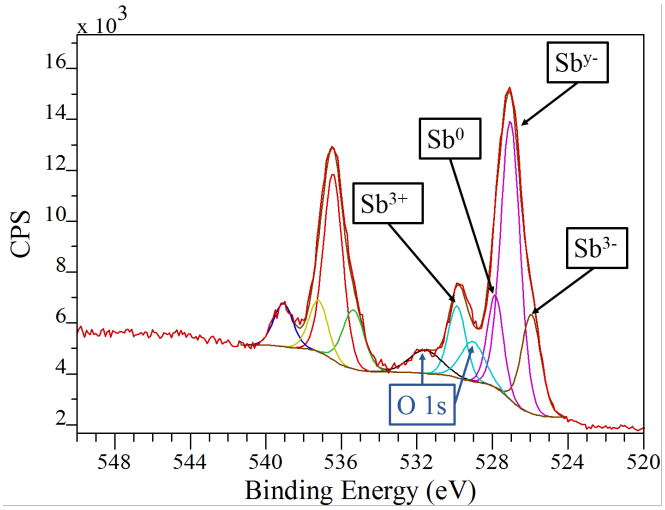

Figure 5.9: XPS measurement on used cathode #199 (Cs_3Sb): high resolution spectrum Sb 3d + O 1s region with peaks model

peak at 529.8 eV (labelled as Sb^{3+}). The same assignment was done by Soriano et al. (121) after oxidation of an alkali-deficient cesium antimonide. The residual oxygen O 1s contribution is split in two peaks: the peak at 531. 5 eV which is attributed to Cs_3O_{11} and a peak at about 529 eV. The latter, for consistency with the analysis done on the antimony peaks, is believed to be associated to the oxygen as in the compound Sb_2O_3 (127). After even little oxygen exposure of K_2CsSb surface, the cesium reacts with the oxygen to form Cs_3O_{11} and as a consequence, elemental Sb (Sb^0) is segregated on the top layer (121). A similar behavior was reported while studying the effect of oxidation on alkali antimonide (122).

As discussed in Sec. 4.2, the upgraded PHIN photoinjector vacuum system ensures a good static vacuum but the electron stimulated desorption contribution is high (pressure bursts associated with breakdowns, beam losses induced desorption). As a matter of fact, water vapour and a small quantity of molecular oxygen were detected with the RGA (Fig. 4.15). Therefore it is likely that the strong QE degradation is related to the oxidation of the cathode surface (formation of Cs_3O_{11} and Sb_2O_3) during the photoinjector operation. One possible explanation of the presence of Sb metal is its segregation at the surface subsequent to the cesium oxidation, as found in literature (121). The origin of the big contribution of the alkali-deficient component is not fully understood. According to the presented analysis, only 14% of the antimony content is in the form of Cs_3Sb, while the main contribution (27%) is attributed to an intermediate Cs-Sb phase with abundance of antimony. The depletion of cesium could be due to high energy particles (ions back bombardment) that may impinge on the cathodes surface. As discussed in Chap. 4.2, this cathode deteriorating effect can generate localized damages, which are actually shown in the QE map of used cathode #199. On the other hand, the Sb-rich phase could be produced during the deposition process if not enough cesium is available, as in the case of cathode #202. The unavailability of XPS measurements on the same cathode surface before the tests in the RF photoinjector does not allow a conclusive explanation.

The XPS spectrum taken with high resolution in the Cs 3d region (Fig. 5.10) shows two sharp peaks (FWHM=1.6 eV) and a weak plasmons structure only visible at the left of the Cs $3d_{3/2}$ peak. Such feature, which was discussed already for cathode #202, is normally associated with low photosensitivity alkali antimonide surfaces.

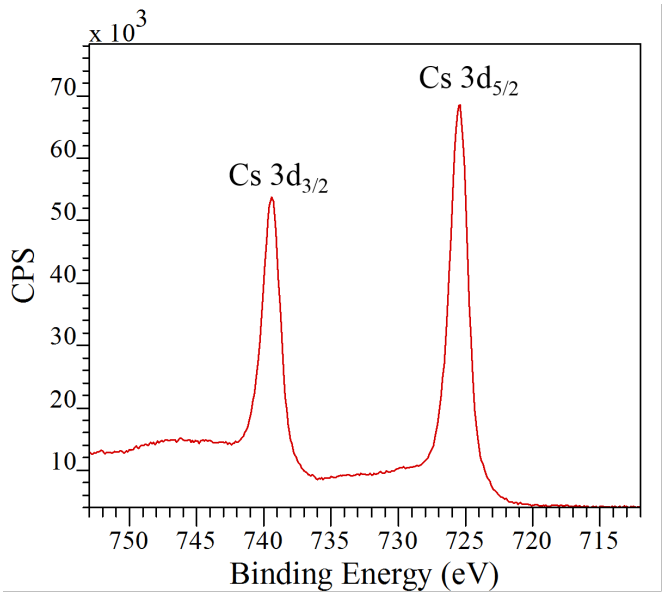

Figure 5.10: XPS measurement on used cathode #199 (Cs_3Sb): high resolution spectrum of Cs 3d region

The presented study shows that the cathodes production process is not optimized for cesium antimonide, in terms of the final stoichiometry of the deposited layer. The variability of the QE values measured on newly produced cathodes, discussed in Sec. 3.3, could be explained as different level of alkali deficiency.

The QE degradation is explained in terms of the contamination of the cathode surface and the formation of other Cs and Sb compounds. For cathode #202, after measurements in the DC gun set up, no antimony oxides were detected. The QE deterioration, instead, is mainly attributed to the adsorption of CO_2 and the subsequent formation of cesium carbonate. However, the coexistence of cesium sub-oxide and adsorbed water together with the carbonate is not excluded. Cathode #199, measured after tests in the RF photoinjector, shows a different surface composition: metal antimony and Sb_2O_3 were found. The poor photoemissive properties of cathode #199 as used, are ascribed to these compounds as well as to Cs_3O_{11}. As pointed out in Chap. 4, the environmental conditions in the RF photoinjector are different with respect to the DC gun beam line, therefore different cathode detrimental processes would be dominant in each setup. The pronounced non-uniformity of the QE map of cathode #199 was attributed to the impact of ions (associated to the beam-induced ionization of residual

gases and to the breakdowns), which seems to be a strongly deteriorating effect. Carbon dioxide is also desorbed during the operation of the PHIN RF photoinjector, as shown by the RGA spectra in Sec. 4.2, but no carbon was detected on the surface of the cathode tested in the RF gun (cathode #199). One possible explanation is associated to the different vacuum systems of the two setups. The PHIN photoinjector vacuum system (Sec. 4.8), in fact, is equipped with Non Evaporable Getter (NEG) coating and NEG cartridge, that have a higher capability of pumping CO_2.

5.2.3 Analysis of cesium telluride cathodes

As already mentioned in Chap. 3, Cs_2Te cathodes produced at CERN show in general a QE$\sim$10% or more when illuminated with UV laser beam. Moreover, they were able to deliver the beam (at 2.3 nC/bunch, 350 ns/train) in the PHIN RF photoinjector for long time, leading to 1/e lifetime values $\sim$ 300 hours (Chap. 4 and literature (41)).

To investigate the different performance with respect to Cs_3Sb cathodes, two co-deposited Cs_2Te cathodes were analysed with the XPS: cathode #203 (as newly produced and after beam tests in the RF photoinjector) and cathode #198 (after usage in the RF gun). The material characterization of these cathodes and its relationship with their photoemissive properties, will be discussed in this section.

Measurements on cathode #203 (Cs_2Te) as newly produced

Figure 5.11 shows the QE maps of cathode #203 (Cs_2Te) as newly produced and after the beam tests in the RF photoinjector. Cathode #203 presented a high quantum efficiency surface as grown, with peak QE $\sim$12%.

The XPS wide range spectrum shown in Fig. 5.12, together with the relative elemental composition, was taken on the cathode surface as newly produced. The signal associated with the copper substrate gives a contribution to the probed volume composition. During the XPS analysis on Cs_3Sb cathodes, no copper was detected neither on the cathode as newly produced nor for the used ones. Moreover, differently from cathode #202 (Cs_3Sb) as grown (Sec. 5.2.2), no oxygen contamination was found on cathode #203 as newly produced. The calculated Cs to Te ratio is 2.1, in agreement with the expected stoichiometry for the Cs_2Te compound.

The XPS measurements taken with high resolution in the Te 3d energy region are displayed in Fig. 5.13. The doublet pair structure is typical of the 3d core levels. The

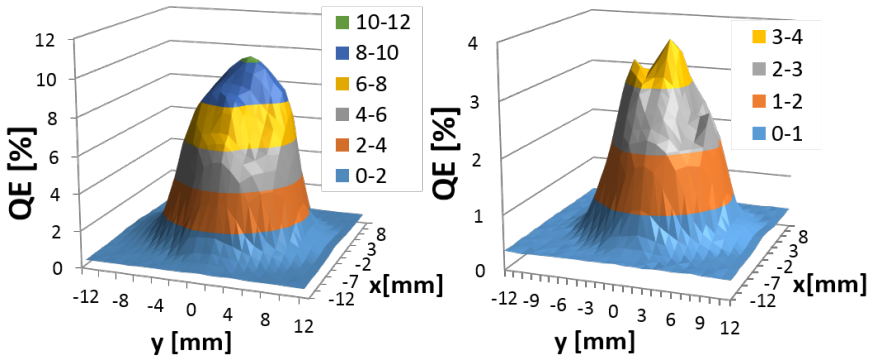

Figure 5.11: QE maps of cathode #203 (Cs_2Te): (a) as newly produced, (b) after beam tests in the PHIN RF photoinjector

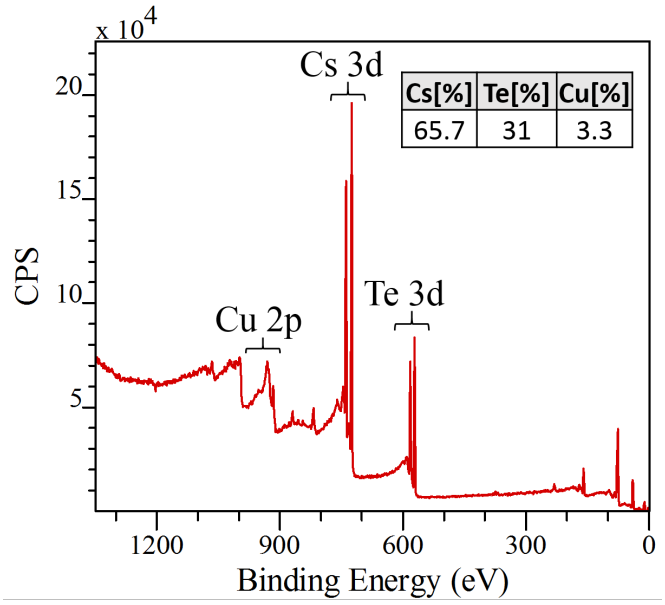

Figure 5.12: XPS measurements of cathode #203 (Cs_2Te) as newly produced: wide range spectrum and relative elemental surface composition

peaks model was obtained following the same procedure as for the Sb 3d core levels (Sec. 5.2.2) and cross-checking the resulting Te 3d spin-orbit shift (10.39 eV).

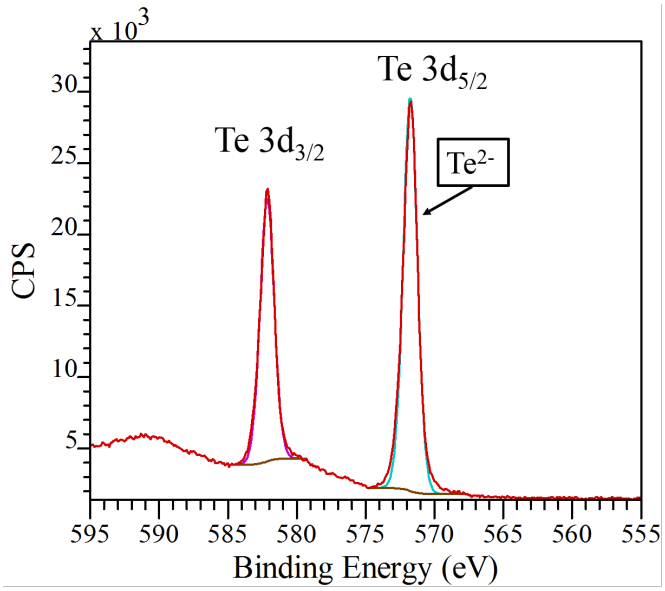

Figure 5.13: XPS measurement on cathode #203 as newly produced: high resolution spectrum of Te 3d region with peaks model

The spectrum is well fitted with a single component at 571.8 eV (only the most intense peak, Te $3d_{5/2}$, will be discussed) and FWHM∼1.2 eV. Given the good photoemissive properties of cathode #203, the reasonable attribution of this peak (labelled as Te^{2-}) is to the tellurium as bound in the Cs_2Te compound. The Te^{2-} peak position is in agreement with the XPS analysis done on Cs_2Te by other authors (35, 128). Moreover, the attribution of the Te peak to the telluride chemical state is consistent with the calculated Cs to Te ratio.

Figure 5.14 displays the doublet pair originated by electrons from the 2p core levels of copper, that sticks out from a high level background associated to the Auger components of cesium[1]. During the production of cathode #203, 30 nm of Cs and 7 nm of Te were evaporated. For a uniformly deposited film, the resulting thickness would be

[1]During XPS measurements, in addition to photoelectrons, Auger electrons can be emitted because of the relaxation of the excited ions remaining after photoemission. In the Auger process, the outer electron falls into the inner orbital vacancy and a second electron, whose kinetic energy is given by the difference between the energy of the initial ion and the double charged final ion, is simultaneously emitted. The Auger series are identified by specifying the initial and final vacancies levels (KLL, LMM, MNN and NOO series (118))

higher than the escape depth of the photoelectrons excited in the substrate (electron mean free path $\sim$ 1 nm (117)). Therefore, the copper contribution is attributed to a non-homogeneous coverage of the substrate surface. Nonetheless, the use of UV laser (λ=266 nm) as probing beam, result in very good photoemissive properties.

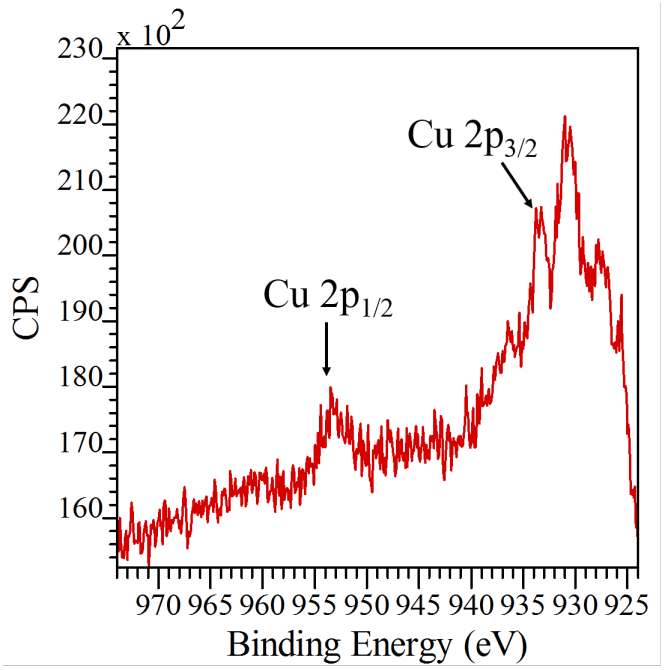

Figure 5.14: XPS measurement on cathode #203 as newly produced: high resolution spectrum of Cu 2p region which is partly overlapping with the Cs MNN Auger lines

Measurements on cathode #203 (Cs_2Te) after beam tests in the PHIN RF photoinjector

The surface of cathode #203 was probed also after beam tests in the PHIN RF photoinjector (more details can be found in (129)). During these tests for long trains (2.3 nC/bunch and 1200 ns/train, 2 nC/bunch and 1600 ns/train), a stainless steel thin vacuum window has been installed to separate the Faraday cup from the rest of the vacuum system. This setup upgrade avoided a strong pressure increase, attributed to the Faraday Cup heating, observed in previous tests (129). The background pressure, apart from the bursts related to breakdowns, was P$\leq 10^{-9}$ mbar for the whole duration of the measurements.

The QE map of cathode #203 after usage in the PHIN photoinjector is displayed in Fig. 5.11 (b). The maximum QE value has decreased from 12% to 4%. Moreover, the QE map is characterized by a strong non-uniformity likely due to the deteriorating effect of ions impinging on the cathode surface, as already noticed for other cathodes, both Cs_2Te and Cs_3Sb, used in the RF photoinjector (Sec. 4.2.6).

The wide range XPS spectrum, taken on the used cathode surface, is shown in Fig. 5.15. The measured Cs to Te ratio is 3.09, higher than the cathode as newly produced. The intensity of Te 3d peaks as well as Cs 3d peaks (discussed later), instead, has decreased compared to the cathode as grown. This implies that the surface is covered with a contamination layer. Therefore, the higher Cs to Te ratio, is explained by the formation of diverse compounds on the top layer being probed, as clarified in the following paragraphs.

As highlighted in Fig. 5.15, oxygen was detected. Moreover the copper contribution has increased by more than two times (relative composition from 3.3% to 8.7%). The stronger signal originated by the Cu substrate, clearly visible in Fig. 5.16, is consistent with the damage due to the impact of high energy particles, that could locally remove the top layer, leading to macroscopic uncovered substrate areas.

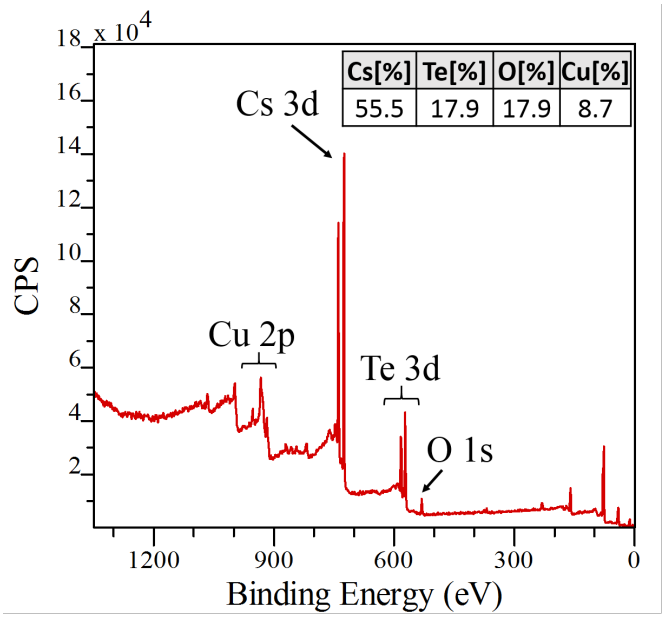

Figure 5.15: XPS measurements on used cathode #203 (Cs_2Te): wide range spectrum and relative elemental surface composition

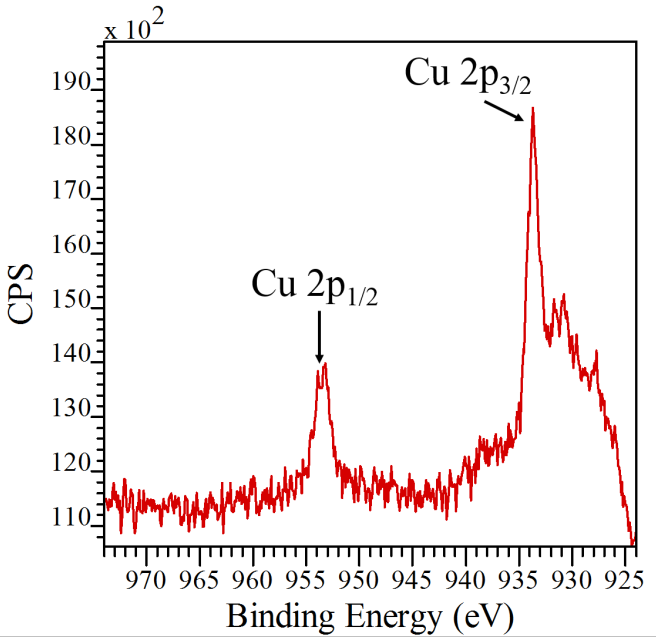

Figure 5.16: XPS measurement on used cathode #203 (Cs_2Te): high resolution spectrum of Cu 2p region which is partly overlapping with the Cs MNN Auger lines

The high resolution XPS spectrum in the region of tellurium peaks with the result of an accurate fitting procedure is shown in Fig. 5.17. The proposed peaks model assumes that two different chemical states of tellurium contribute to the broad peak at 572.4 eV. The peak at 571.8 eV, labelled as Te^{2-}, is attributed to the telluride state as found on the cathode as grown. The most reasonable attribution of the peak at higher binding energy (572.7 eV) is to metallic tellurium (Te^0), in agreement with measurements done in the same XPS setup on tellurium film deposited on a copper sample. Metallic Te was also found by other authors (35) during XPS studies of Cs_2Te photocathodes exposed to oxygen. Moreover, some publications (130) reported the formation of metallic tellurium on Cs_2Te cathodes during the operation in an RF photoinjector. Part of the tellurium is oxidized (TeO_3), as visible from the presence of the component at 576.8 eV attributed to Te^{6+} (in agreement with data in literature (118)).

The oxygen contribution is clearly visible in the XPS spectrum taken with high resolution in the O 1s region (Fig. 5.18), which was not observed on cathode #203 as newly produced. The broad (FWHM ∼2 eV) O 1s peak at 531.2 eV is attributed to the coexistence of two different chemical states of oxygen: as bound in TeO_3 and as

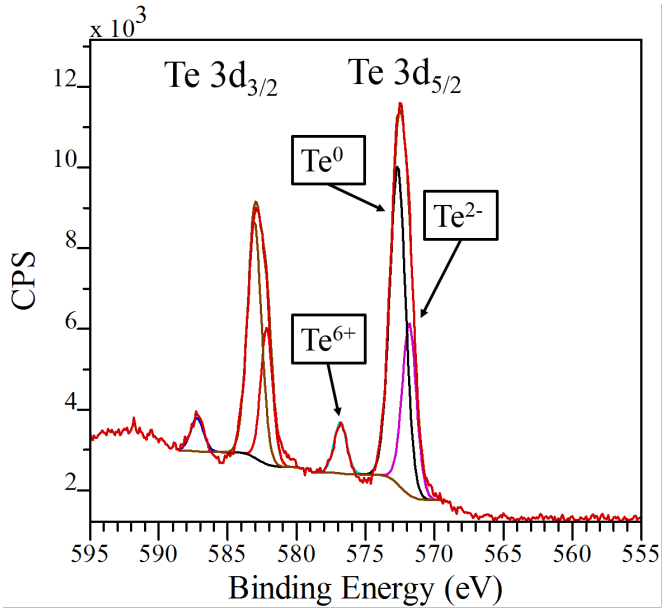

Figure 5.17: XPS measurements on used cathode #203 (Cs_2Te): high resolution spectrum of Te 3d region with peaks model

bound with cesium. The same oxides formation is reported for low O_2 exposure (10 L[1] range) of cesium telluride cathodes by other authors (132). These authors attributed the cesium oxide to Cs_2O_2.

As already explained in Sec. 5.2.2, the Cs photoemission peaks do not show important chemical shifts. According to the results above, on cathode #203 as used, a cesium oxide was formed during the studies in the RF photoinjector. The intensity of the Cs doublet pair, in fact, has decreased compared to the measurements on the as grown surface, displayed in red in Fig. 5.19, and the peaks are slightly wider (FWHM=1.5 eV).

The less pronounced plasmons structure is also an indication of non-identical composition due to the formation of different Cs chemical states. This feature is normally associated with lower QE surface (133), as for cesium antimonide cathodes.

Following this discussion, the QE decrease of cathode #203 after usage is ascribed to the oxidation of both elements, cesium and tellurium, and the formation of metallic tellurium as a consequence of these chemical reactions. The influence of the ions and electrons bombardment in the formation of these different compounds is not excluded.

[1]The unit Langmuir (L) corresponds to an exposure of 10^6 torr during one second (131)

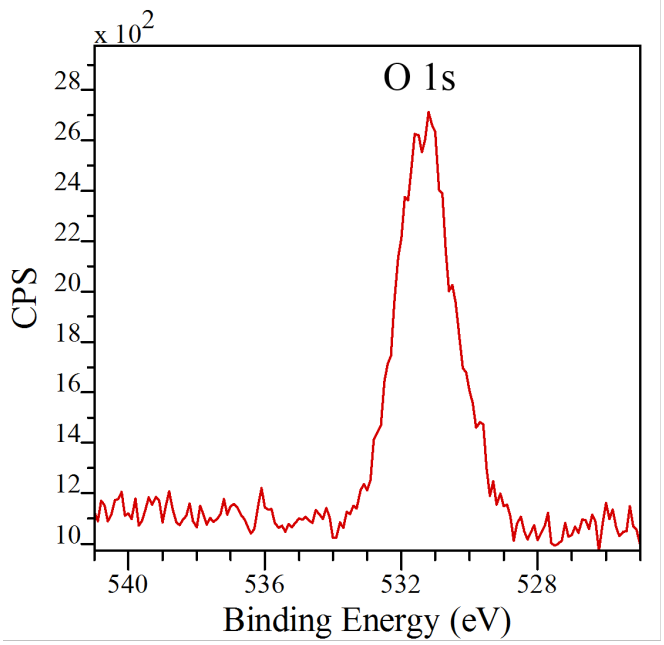

Figure 5.18: XPS measurement on used cathode #203: high resolution spectrum of O 1s region

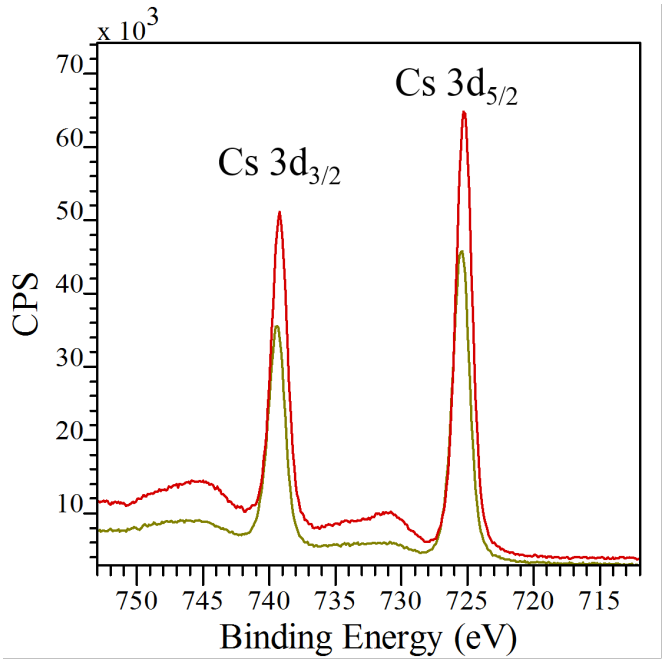

Figure 5.19: XPS high resolution spectra of Cs 3d region on cathode # 203 (Cs_2Te) as newly produced (red line) and as used (green line)

Measurements on cathode #198 (Cs_2Te) after tests in the PHIN RF photoinjector

Cathode #198 was analysed with XPS after the tests performed in the PHIN RF photoinjector (Sec. 4.2). Its degraded photoemissive properties after usage were discussed already in Sec. 4.2.6: the QE map which originally showed a flat top (Fig. 4.21 (a)), exhibits instead, for the cathode as used, peaks and craters (Fig. 4.21 (b)). Moreover the maximum QE value has decreased from 14% to 4%.

Figure 5.20 shows the XPS wide range spectrum together with the relative elemental composition of the used cathode #198. The measured Cs to Te atomic ratio is 1.4, lower than what it should be for an optimal stoichiometric ratio of the compound Cs_2Te. As displayed in Fig. 5.20, also copper and oxygen were detected on the surface. The copper signal (8.1%, clearly visible in Fig. 5.21) is associated with the substrate contribution, as already explained in previous paragraphs. The deposited layer could have been partially removed due to ions bombardment of the cathode surface during the photoinjector operation. Otherwise, the copper signal could be the result of a non-uniform coverage of the photoemissive film already on the as grown stage (as for cathode # 203). The unavailability of XPS analysis on the same cathode as newly produced, does not allow to favour one explanation over the other.

Figure 5.22 shows the XPS spectrum measured with high resolution in the region of tellurium 3d peaks on the same cathode surface. The experimental data are fitted by assuming the coexistence of two different compounds in the broad peak at 571.5 eV. The most reasonable assignation to the low binding energy (570 eV) peak is to Te^{2-} as bound in Cs_2Te. The peak at 572 eV (labelled as Te^{x-}) is attributed to a Te-rich phase with unknown stoichiometry. The presence of a compound with different stoichiometry, is justified by the manifold Cs-Te phase diagram (134). Other authors (35) reported a Te $3d_{5/2}$ peak at similar binding energy as the Te^{-x} peak, for low level of cesiation during the production of cesium telluride cathodes. On cathode #198, this alkali-deficient phase could have been produced during the deposition or be the result of the chemical changes that the cathode surface undergoes during the operation in the RF photoinjector. The unavailability of the XPS analysis on the same cathode as grown, does not allow to determine the validity of one explanation over the other.

The component labelled as Te^{4+}, well apart peak at 575.9 eV, is attributed to the tellurium state as bound in the compound TeO_2, in agreement with data in lit-

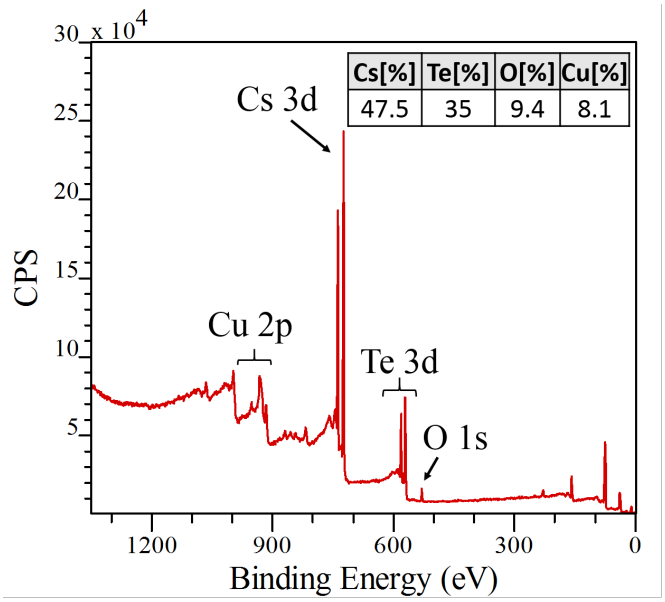

Figure 5.20: XPS measurements of used cathode #198 (Cs_2Te): wide range spectrum and relative elemental surface composition

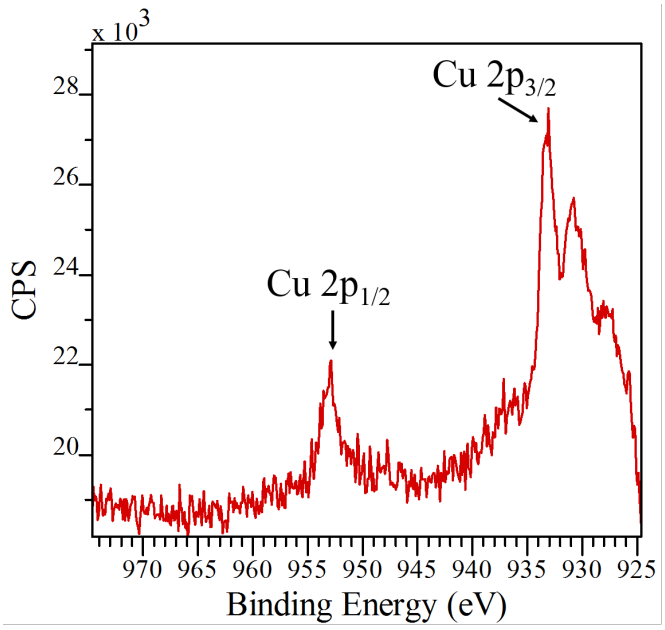

Figure 5.21: XPS measurements of used cathode #198 (Cs_2Te): high resolution spectrum of Cu 2p region which is partly overlapping with the Cs MNN Auger lines

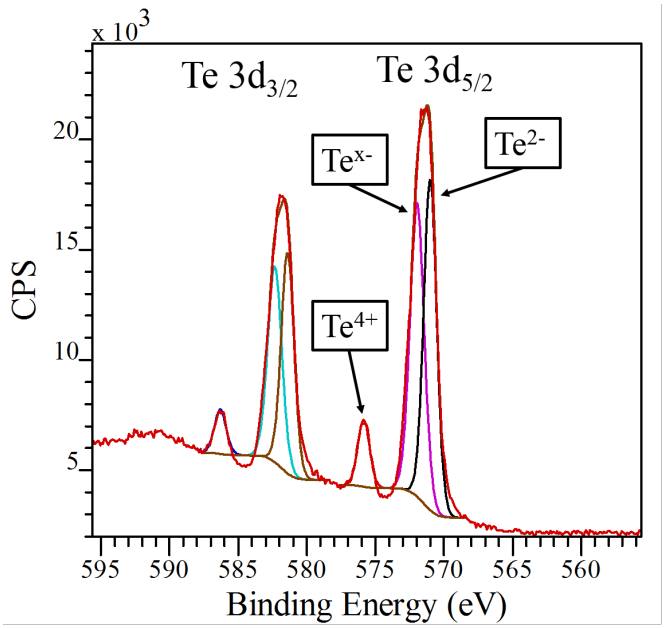

Figure 5.22: XPS measurements of used cathode #198 (Cs_2Te): high resolution spectrum of Te 3d region with peaks model

erature (118). In comparison with the peaks model proposed for cathode #203, the Te peak related to the oxide is at ∼1 eV lower binding energy than the O 1s peak (Fig. 5.23). Moreover, the relative oxygen composition is half with respect to the measurements on cathode # 203. These remarks suggest that the photoemissive layer of cathode #198 has reacted with oxygen forming a different oxide than cathode #203. The formation of the tellurium dioxide TeO_2 is also reported by Soriano et al. (132) for Cs_2Te exposed to a high oxygen dose (10^2 L).

It is not excluded that oxygen as bound in cesium oxide contributes to the broad peak (FWHM=1.8 eV) labelled as O 1s in Fig. 5.23, in addition to the oxygen bound to the tellurium dioxide. The formation of Cs_2O_2 was in fact observed in parallel to the oxidation of tellurium by Soriano et al. (132). The XPS measurements taken with high resolution in the region of Cs 3d core levels (Fig. 5.24) show two peaks characterized by a width of a FWHM=1.6 eV and a plasmons structure not well pronounced. A detailed study of this spectrum is limited by the small chemical shifts of the photoelectron peaks related to different Cs chemical states. Moreover, the same measurements on the same cathode as grown are not available for comparison.

Both the analysed cesium telluride cathodes (#203 and #198) show, after usage,

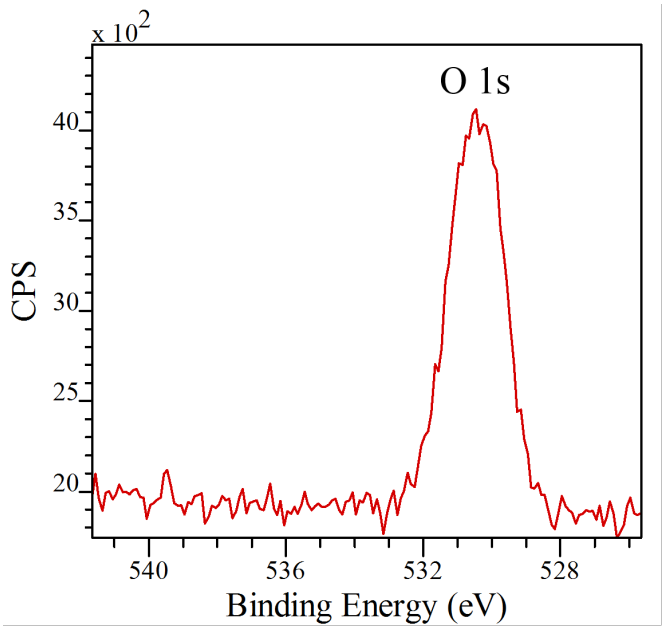

Figure 5.23: XPS measurements of used cathode #198 (Cs_2Te): high resolution spectrum of O 1s region

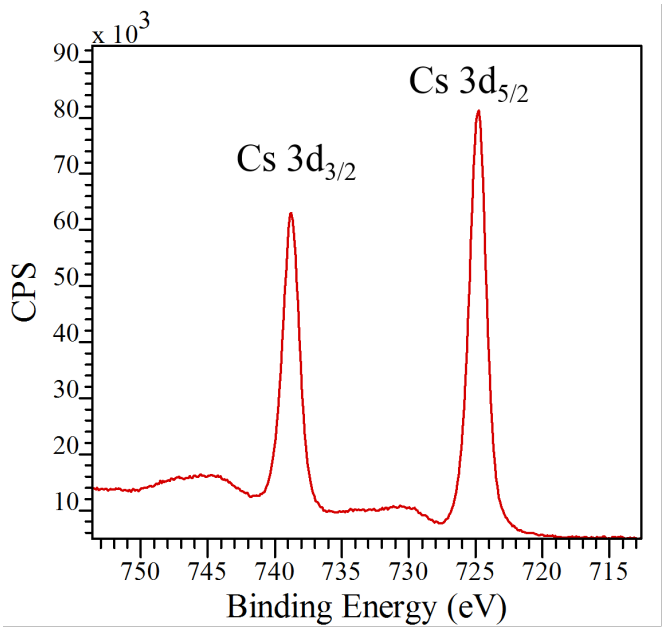

Figure 5.24: XPS measurements of used cathode #198 (Cs_2Te): high resolution spectrum of Cs 3d region

an average QE of 3% and are characterized by a mixture of different compounds. The XPS studies, however, highlighted different chemical compositions. The used cathode #203 has a stronger oxygen contamination (17.9%) than cathode #198 (9.4%), while the copper contribution is similar. Moreover, following the peaks position, different tellurium oxides were assigned to the peaks model proposed for the two different cathodes (TeO_3 for #203, TeO_2 for #198). The degraded photoemissive properties are ascribed to the oxides formation as well as to the presence of metallic Te (on cathode # 203 as used) and the Te-rich phase (on used cathode #198).

5.2.4 Conclusion

These XPS studies suggest that different phases of the Cs-Sb can be produced through the co-deposition process. The variability of the QE values measured while illuminating the Cs_3Sb as grown with a laser beam at λ=532 nm, could be explained as different level of alkali deficiency. For the Cs_2Te cathode as newly produced, instead, only one compound was found with a stoichiometry very close to the optimal one (taking into account the uncertainty in the determination of the sensitivity factors). Different Cs-Te phases may or may not be produced during the co-deposition of cesium telluride cathodes, but the lack of cesium is less detrimental than for Cs_3Sb, considering the different optimal stoichiometry. Moreover, high QE values can be routinely obtained for co-deposited Cs_2Te cathodes probed with UV laser beam.

Following the XPS analysis carried out, Cs-Te compounds seem to have a different reactivity to residual gas exposure than Cs-Sb compounds. The XPS analysis on the Cs_3Sb cathode as grown highlighted water vapour contamination together with the presence of cesium sub-oxide pollution. The Cs_2Te cathode studied with XPS as newly produced, instead, did not show any oxygen or oxide related contamination even if it was produced and stored in the same UHV systems as cesium antimonide cathodes.

Cathode #202 (Cs_3Sb), during lifetime measurements in the DC gun setup, was contaminated by cesium carbonate, whose formation was attributed to the reaction of Cs with CO_2. No carbon or carbon based compounds were detected on the Cs_2Te cathodes. The CO_2 poisoning effect of cesium telluride cathodes was tested by other authors showing a much slower QE degradation than for oxygen exposure (35). This seems to suggest that cesium telluride cathodes are less affected by exposure to CO_2.

However, those cathodes were not used in the DC gun setup and the PHIN photoinjector vacuum system could be more effective in pumping the CO_2.

After tests in the PHIN RF photoinjector, both cathode materials showed oxidation. Cathode #199 (Cs_3Sb) was polluted by cesium sub-oxide and Sb_2O_3, while on the Cs_2Te cathodes a mixture of cesium oxide (attributed to Cs_2O_2) and different tellurium oxides (TeO_3 for cathode #203 and TeO_4 for cathode #198) was found. The poor photoemissive properties are partially ascribed to the oxidation. In addition to the oxides, different phases were found on the used cathodes. Metallic tellurium (on cathode #203) and metallic antimony (on cathode #199) were detected. For cathode #203 (Cs_2Te), the tellurium was formed during the degradation process, as it was not found on the same cathode surface as newly produced. The same explanation cannot be confirmed for cathode #199 due to the unavailability of XPS analysis on the film as grown. It is not excluded that high energy ions hitting the cathode surface are also involved in changing the chemical composition, e.g. through preferential sputter of some elements or through chemical reaction with the ions species. Moreover, electrons impact might induce superficial reactions with the residual gases.

5. X-RAY PHOTOELECTRON SPECTROSCOPY STUDIES OF PHOTOCATHODES

Chapter 6

Conclusions and outlook

Cesium antimonide photocathodes, used in combination with green laser beams, are promising candidates for the generation of high brightness electron beams. In this PhD work, a thorough experimental investigation of the use of this photocathode material in high charge RF photoinjectors was conducted. An extensive characterization of the main Cs-Sb photocathode features was carried out in the PHIN high charge RF photoinjector as well as in the DC gun beam line at the CERN photoemission laboratory. Despite the difficulties due to the very stringent requirements for the manipulation of this cathode material, a systematic study of the correlation of its photoemissive properties with the surface chemical composition, as measured with the XPS analysis, was conducted at different stages of the cathode life. These studies include also a close comparison with the performance of Cs_2Te cathodes.

The operational lifetime measurements performed in the PHIN RF photoinjector (Chap. 4), suggest that the alkali antimonide cathodes are less robust than the cesium telluride. However, the beam production with Cs_3Sb was influenced by non optimal operating conditions (malfunctioning of some equipments, e.g. the klystron) that could strongly influence the cathode deterioration inducing strong RF breakdowns. Therefore, more tests are required to further investigate the cesium antimonide performance in an RF photoinjector. In addition, more cathodes need to be studied by XPS analysis before and after operation in the PHIN photoinjector in order to further validate the conclusions regarding the observed performance of both Cs_2Te and Cs_3Sb.

Possible mechanisms of degradation of the cathode photoemissive properties have been identified (Chap. 4). The XPS analysis allowed to investigate their impact on

the cathode surface composition. The chemical poisoning process is mainly attributed to the formation of oxides for both Cs_3Sb and Cs_2Te cathodes. Moreover, cesium carbonate was formed on the surface of the cesium antimonide cathode tested in the DC gun setup. The "radiation damage" deteriorating effect is well represented by the non-uniform QE maps of cathodes tested in the PHIN RF photoinjector, which is not observed for measurements done in the DC gun beam line. The bombardment of ions (associated to the beam-induced ionization of residual gases and to the RF breakdowns) is likely to produce local damages such as removal of the deposited film.

Despite the high QE routinely obtained with the co-deposition process for Cs_2Te cathodes, some limitations have been identified for the production of Cs_3Sb cathodes. The variability of the final QE values was explained as different level of Cs-deficiency in the compounds produced during the deposition process. In order to optimize the production process, more Cs_3Sb photocathodes need to be produced and characterized.

The current preparation chamber has some restrictions mainly related to the unavailability of a load lock system for introducing substrates and the fact that the evaporators setup is part of the same vacuum sector (Chap. 3). This implies the venting of the whole preparation chamber during both the introduction of new substrates and the dispensers replacement. Given the high capacity of the CERN-made Sb and Te dispensers, the limitation is mainly related to the low capacity of the used commercial Cs dispensers. Different solutions for upgrading the preparation chamber were studied and designed (103), but their implementation requires major modifications of the laboratory facility due to space constraints. An improvement of the evaporators setup, however, would be also effective in mitigating the issue related to the unavailability of a separated vacuum sector for the evaporators. Therefore, an upgraded evaporation setup was recently designed to increase the availability of cesium (135). Two different solutions were proposed. The first proposal allows to accommodate two instead of one Cs dispenser (from SAES Getters S.p.A.) that can be heated together during the deposition of the other element (tellurium or antimony). The second solution is similar but makes use of a different type of Cs dispenser (from Alvatec) characterized by a higher volume and therefore higher cesium capacity. The first solution was already partially implemented and will be tested in the near future.

Given the valuable information provided by the XPS analysis, this technique should be introduced in the standard CERN procedure of characterization of photocathodes

as grown, together with the QE mapping performed in the DC gun setup. The development of a dedicated UHV transport vessel, or even better an in-situ characterization setup, could be considered to allow more material characterization techniques, such as Scanning Electron Microscope (SEM), to get information on the morphology of the cathode surface, and X-Ray Diffraction (XRD), to investigate the crystallography structure of the deposited films. This would help optimizing the co-deposition process.

Moreover, a collaborative work with the ASTeC team at Daresbury Laboratory (UK) was initiated. The adaptation of the ASTeC UHV cathode suitcase to the CERN cathode preparation setup will allow the transport of the co-deposited cathodes and their loading in the ASTeC UHV Multiprobe Surface Analysis System, where the cathodes can be characterized using diverse techniques: XPS, AFM (Atomic Force Microscopy), SEM as well as QE measurements.

These activities will help continuing the development of Cs_3Sb cathodes as well as Cs_2Te for high charge photoinjector applications. As a matter of fact, both cathode materials are still interesting candidates for the CLIC drive beam photoinjector option. Cesium antimonide cathodes give a higher contribution to the dark current (Chap. 4), which can cause more frequent RF breakdowns. Moreover, the average quantum efficiency (about 3.5% at λ=532 nm) of the co-deposited Cs_3Sb cathodes, for which the production process is not yet optimized, is lower than the average QE of cesium telluride cathodes (about 15% at λ=266 nm). On the contrary, the use of Cs_2Te cathodes in combination with a UV laser beam has to face both the difficulties of the UV laser beam transport and the limited efficiency of the 4^{th} harmonic conversion stage. Therefore, the use of Cs_2Te results in a more strict QE requirement (Table 1.1): QE>3% instead of QE>0.5%(for $CsSb_3$ cathodes) for producing the same electron beam current. Moreover, to overcome the limitation of the generation of the UV long train time structure (Chap. 1), an R&D program dedicated to the development of different frequency conversion schemes would be needed. In this respect, some studies and tests using multi-crystal systems have already started at CERN.

The Cs_3Sb cathode material has been deeply investigated in this work. Another possible photocathode candidate, known for having high QE in the visible range as introduced in Chap. 2, is K_2CsSb. In order to be able to produce a three-components compound, a new design of the deposition setup was recently developed (135). However, with this design, one of the two available thickness monitors will be measuring both the

potassium and the cesium vapour deposition rate. The feasibility of producing K_2CsSb cathodes, with a modified co-deposition process, will be investigated in the future.

Major steps have been performed towards the development of photocathodes for new generation photoinjectors. The full implementation of this new and delicate technology remains however an objective which goes beyond the current status of the research activity for the CLIC project. Given the specifications (Table 1.1), in fact, a 1 GHz gun, designed for the CLIC parameters, as well as the associated development of the laser setup are required to fully validate the feasibility of a photoinjector for the CLIC drive beam.

List of Figures

LIST OF FIGURES

List of Tables

LIST OF TABLES

Bibliography

[1] **CLIC study project website**. http://clic-study.org/.

[2] O.S. Bruning et al, editor. *LHC Design Report*. CERN, 2004. DOI:10.5170/CERN-2004-003-V-1.

[3] M. Aicheler et al., editor. *A multi-TeV linear collider based on the CLIC technology: CLIC Conceptual Design Report*. CERN, 2012. CERN-2012-007.

[4] T. Behnke et al, editor. *The International Linear Collider Technical Design Report*. FERMILAB, 2013.

[5] P. Urschutz et al. **Beam dynamics and first operation of the sub-harmonic bunching system in the CTF3 injector**. In *Proceedings of EPAC06*, Edinburgh, Scotland, 2006.

[6] M. Csatari Dival. **Fast phase switching within the bunch train of the PHIN photoinjector at CERN using fiber-optic modulatros on the drive laser**. *Nucl. Inst. Meth. Phys. Res. A*, **659**:1–8, 2011.

[7] M. Petrarca et al. **Study of the Powerful Nd:YLF Laser Amplifiers for the CTF3 Photoinjectors**. *IEEE Journal of Quantum Electronics*, **47**(3), March 2011.

[8] E.A. Khazanov. **Development of Harmonics (2nd and 4th) Generation Stages for High Average Power Long Burst Operation Mode as Specified for Optional CLIC Drive Beam Photoinjector**. Technical report, 'Institute of Applied Physics RAS (https://edms.cern.ch/document/1560209/1), 2011.

[9] A.H. Sommer. *Photoemissive Materials*. John Wiley and Sons,Inc., New York, 1986.

[10] Hamamatsu Photonics K.K. *Photomultiplier Tubes, Basics and Applications*. Hamamatsu Phononics K.K., 2007.

[11] W.E. Spicer. **Photoemissive, Photoconductive and Optical Absorption Studies of Alkali-Antimony Compounds**. *Phys. Rev.112,1*, **112**:114–122, 1958.

[12] W.E. Spicer et al. **Modern Theory and Applications of Photocathodes**. *SLAC-PUB-6306*, August 1993. SLAC/SSRL-0042.

[13] D.H. Dowell et al.. **Quantum efficiency and thermal emittance of metal photocathodes**. *Phys. Rev. ST Accel. Beams*, **12**:074201, 2009.

[14] D.H. Dowell et al.. **Results from the average power laser experiment photocathode injector test**. *Nucl. Instr. Meth.Phys. Res. A*, **356**:167–176, 1995.

[15] G. Suberlucq. **Technological challenges for high brightness photoinjectors**. In *Proceedings of EPAC04*, Lucerne, Switzerland, 2004.

[16] G. Suberlucq et al. **Photocathodes tested in the dc gun of the CERN photoemission laboratory**. *Nucl. Instr. Meth. Phys. Res. A*, **A340**:146–156, 1994.

[17] J.L. McCarter et al. **Performance study of K_2CsSb photocathode inside a DC high voltage gun**. In *Proceedings of PAC11*, New York,NY,USA, 2011.

[18] J. Buon. **Beam phase space and emittance**. In *CERN Accelerator School Fifth General Accelerator Physics Course*, **1**, page 89. S.Turned Ed., Geneva, 1994.

[19] M. P. Stockli. **Measuring and Analyzing the Transverse Emittance of Charged Particle Beams**. In *AIP Conference Proceedings*, Batavia, Illinois (USA), 2006.

[20] D. Sertore. **Photocathode for high brightness electron beams**, 2013. Presentation at:1st Topical Workshop on Laser Based Particle Sources.

[21] F. Stephan et al. **Detailed characterization of electron sources yielding first demonstration of European X-ray Free-Electron Laser beam quality**. *Phys. Rev. ST Accel. Beams*, **13**:020704, Feb 2010.

[22] D.H. Dowell et al. **Cathode R &D for future light sources**. *Nucl. Instr. Meth. Phys. Res. A*, **622**(3):685 – 697, 2010.

[23] F. Zhou et al. **Experimental characterization of emittance growth induced by the nonuniform transverse laser distribution in a photoinjector**. *Phys. Rev. ST Accel. Beams*, **5**:094203, Sep 2002.

[24] D. Xiang et al. **First Principle Measurements of Thermal Emittance for Copper and Magnesium**. In *Proceedings of PAC07*, Albuquerque, New Mexico (USA), 2007.

[25] M. Krasilnikov. **Impact of the cathode roughness on the emittance of an electron beam**. In *Proc. FEL 06*, Berlin, Germany, 2006. THPPH013.

[26] O. Mete et al. **Production of long bunch trains with 4.5 μC total charge using a photoinjector**. *Phys. Rev. ST Accel. Beams*, **15**:022803, 2012.

[27] J.W. Wang et al. **Field Emission and RF Breakdown in High-Gradient Room-Temperature Linac Structures**. *SLAC PUB 7684*, October 1997.

[28] S. Doebert. **RF breakdown in high-frequency accelerators**. *SLAC-PUB-10463*, May 2004.

[29] W. Wuensch. **High-gradient breakdown in normal conducting RF cavities**. In *Proc. EPAC 02*, Paris, France, 2004.

[30] A. Degiovanni. *High gradient proton LINAC for medical applications*. PhD thesis, EPFL, 2014.

BIBLIOGRAPHY

[31] S. Lederer et al. **Investigations on the increased lifetime photocahtodes at FLASH and PITZ**. In *Proceedings of PAC09*, Vancouver,BC,Canada, 2009.

[32] J. Smedley. USPAS Course on Cathodes Physics (http://uspas.fnal.gov/materials/12UTA/UTA-Cathode.shtml).

[33] X.J. Wang et al. **Mg cathode and its thermal emittance**. In *Proc. of LINA2002*, Gyeongju, Korea, 2002.

[34] R.A. Powell et al.l. **Photoemission Studies of Cesium Telluride**. *Phys. Rev. B*, **8**:3987, 1973.

[35] A. di Bona et al. **Auger and X-ray photoemission spectroscopy study on Cs_2Te photocathodes**. *J. Appl. Phys.*, **80**:5, 1996.

[36] P. Michelato. **Photocathodes for RF photoinjectors**. *Nucl. Instr. Meth. Phys. Res. A*, **393**:455–459, 1997.

[37] H. Trautener. *Spectral Response of Cesium Telluride and Rubidium Telluride Photocathodes for the Production of Highly Charged Electron Bunches*. PhD thesis, Universitat in Mainz, 1999.

[38] S.H. Kong et al. **Cesium telluride photocathodes**. *J. Appl. Phys.*, **77**:11, 1995.

[39] J. Teichert et al. **Free-electron laser operation with a superconducting radio-frequency photoinjector at ELBE**. *Nucl. Instr. Meth.Phys. Res. A*, **743**:114–120, 2014.

[40] E. Chevallay. **Experimental Results at the CERN Photoemission Laboratory with Co-deposition Photocathodes in the Frame of the CLIC Studies**. *CTF3 Note 104*, 2012.

[41] C. Hessler et al. **Lifetime studies of Cs_2Te Cathodes at the PHIN RF Photoinjector at CERN**. In *Proc. IPAC 12*, New Orleans, Louisiana (US), 2012. TUPPD066.

[42] W.H.McCarroll. **Chemical and structural characteristics of the potassium-cesium-antimony photocathode**. *J. Phys. Chem. Solids*, **26**:191–195, 1964.

[43] A.R.H.F. Ettema et al. **Electronic structure of Cs_2KSb and K_2CsSb**. *Physical Review B*, **66**:115102, 2002.

[44] B. Bennecer et al. **Optical properties of the alkali antimonide semiconductors Cs_3Sb, Cs_2KSb, CsK_2Sb and K_3Sb**. *J. Phys. Chem. Solids*, **71**:314–322, 2010.

[45] W. E. Spicer. **Photoemission and Related Properties of the Alkali-Antimonides**. *J. Appl. Phys.*, **31(12)**, December 1960.

[46] K.L. Jensen et al. **Theory of photoemission from cesium anitmonide using an alpha-semiconductor model**. *J. Appl. Phys.*, **104**:044907, 2008.

[47] P. Michelato et al. **Alkali photocathode development for superconducting rf guns**. *Nucl. Instr. Meth.Phys. Res. A*, **340**:176, 1994.

[48] R.L. Sheffield et al. **The Los Alamos Photoinkector Program**. *Nucl. Instr. Meth. Phys. Res. A*, **272**:222–226, 1988.

[49] S.H. Kong et al. **Photocathodes for free electron lasers**. *Nucl. Instr. Meth. Phys. Res. A*, **358**:272–275, 1995.

[50] A. H. Sommer. **A new Alkali Antimonide Photoemitter with high sensitivity to visible light**. *Applied Physics Letters*, **3**:62, 1963.

[51] C. Ghosh et al. **Preparation and study of properties of a few alkali antimonide photocathodes**. *J. Appl. Phys.*, **49(8)**, August 1978.

[52] A. di Bona et al. **Development, operation and analysis of bialkali antimonide photocathodes for high-brightness photo-injectors**. *Nucl. Instr. Meth.Phys. Res. A*, **385**:385, 1997.

[53] J. Smedley et al. **K_2CsSb cathode development**. In *American Institute of Physics Conference Series*, **1149**, pages 1062–1066, 2009.

[54] T. Vecchionet et al. **A low emittance and high efficiency visible light photocathode for high brigthenss accelerator-based X-ray light sources**. *Apl. Phys. Let.*, **99**(3):034103, 2011.

[55] T.Rao et al. **Photocathodes for the energy recovery linacs**. *Nucl. Instr. Meth.Phys. Res. A*, **557**:124–130, 2006.

[56] P. Michelato et al. **Multialkali Thin Photocathodes for High Brightness guns**. In *Proc. EPAC 94*, page 1456, London, UK, 1994.

[57] P. Michelatol et al. **R & D activity on high QE alkali photocathodes for RF guns**. In *1995 IEEE Particle Accelerator Conference*, Dallas, TX, USA, 1995.

[58] J. Smedley et al. **High efficiency visible photocathode development**. In *Proc. IPAC 11*, San Sebastian, Spain, 2011. THPC136.

[59] S. Schubert et al. **Bi-alkali antimonide photocahtodes for high brightness accelerators**. *Apl Materials 1*, **1**:032119, 2013.

[60] N. Chanlek. *Quantum efficiency lifetime studies using the photocathode preparation experimental facility developed for the ALICE accelerator*. PhD thesis, The University of Manchester, 2011.

[61] C. Hernandez-Garcia et al. **A high average current DC GaAs photocatode gun for ERLs and FELs**. In *Proc. PAC 05*, Knoxville,Tennessee (US), 2005.

[62] M. Steigerwald et al. **The new polarized beam injection at MAMI**. In *Proc. EPAC 98*, 1998. MOP02E.

[63] W.E. Spicer et al. **The III-V Photocathode: a Major Detector Development**. *Pub. Astron. Soc.*, **84**:110, 1972.

[64] W.E. Spicer. **Negative Affinity 3-5 Photocathodes: Their Physics and Technology**. *Appl. Phys.*, **12**:115–130, 1977.

[65] N. Chanlek et al. **The degradation of quantum efficiency in negative electron affinity GaAs photocathodes under gas exposure**. *J. Phys. D: Appl. Phys.*, **47**, 2014.

[66] R. Alley et al. **The Stanford Linear Accelerator polarized electron source**. *Nucl. Instrum. Meth. Phy. Res. A*, **A365**:1–27, 1995.

[67] N. Chanlek et al. **Gallium Arsenide preparation and QE lifetime studies using the ALICE photocathode preparation facility**. In *Proc. IPAC 10*, Kyoto, Japan, 2010. TUPEC018.

[68] D.A. Orlov et al. **Long term operation of high quantum efficiency GaAs(Cs,O) photocathodes using multiple recleaning by atomic hydrogen**. *J. Appl. Phys.*, **106**, 2009.

[69] R. Ganter et al. **Nanosecond field emitted and photo-field emitted current pulses from ZrC tips**. *Nucl. Inst. Meth. Phys. Res. A*, **565**(2):423 – 429, 2006.

[70] Z. M. Yusof et al. **Schottky-Enabled Photoemission in a rf Accelerator Photoinjector: Possible Generation of Ultralow Transverse Thermal-Emittance Electron Beam**. *Phys. Rev. Lett.*, **93**:114801, Sep 2004.

[71] P. Bloch. **Preliminary Investigation of the Two Photon Photoelectric Effect**. *J. Appl. Phys.*, **35(7)**, 1964.

[72] A. Lorusso. **Overview and development of metallic photocathodes prepared by laser ablation**. *Applied Physics A. Material Science and Processing*, **110**:869–875, 2013.

[73] L. Cultrera. **Pulsed laser deposition of MG thin films on Cu substrates for photocathode applications**. *Appl. Surf. Sci.*, **248**:397–401, 2005.

[74] MicroMagnetics Inc. **Magnetron Sputtering Technology**.

[75] J. Smedley et al. **Sputter growth of alkali antimonide photocathodes: an in operando materials analysis**. In *Proc. IPAC 15*, Richmond,VA (US), 2015. TUPHA003.

[76] E. Chevallay. **Procedure: Mechanical Movements of the Cathodes at the Photoemission Laboratory**. Technical report, CERN (https://edms.cern.ch/document/1265255/1), 2013.

[77] E. Bravin. **Transverse beam profiles**. CERN Accelerator School Course on Beam Diagnostics. DOI:10.5170/CERN-2009-005.

[78] P. Odier. **New Wide Band Wall Current Monitor**. In *Proc. DIPAC 2003*, Mainz, Germany, 2003.

[79] J. Durand et al. **A 10 GHz Wall Current Monitor**. *PS/LP/Note 95-09*, 1995.

[80] R. Jones et al. **Introduction to beam instrumentation and diagnostics**. CERN Accelerator School: Advanced Accelerator Physics Course. DOI: 10.5170/CERN-2014-009.23.

[81] K.H. Bernhardt. **Vacuum technology compendium**. Pfeiffer Vacuum GmbH, 2010.

[82] G.J. Peter et al. **Partial pressure gauges**. CERN Accelerator School and ALBA Synchrotron Light Facility: Course on Vacuum in Accelerators. DOI: 10.5170/CERN-2007-003.195.

[83] G. Suberlucq. **Development et production de photocathodes pour le CLIC Test facility**. *CLIC Note 299*, 1996.

[84] T. Vecchione et al. **Effect of Roughness on Emittance of Potassium Cesium Antimonide Photocathodes**. In *Proceedings of IPAC2012*, New Orleans, Louisiana, USA, 2012.

[85] R.J. Reid. **Cleaning for vacuum service**. *OPEN-2000-276*, pages 139–153, 1999.

[86] E.S. Gadelmawla et al. **Roughness parameters**. *J. Mat. Proc. Tech.*, **123**:133, 2002.

[87] S. Mistry. PhD thesis on Study of surface properties of metallic photocathodes for use in NCRF guns (in preparation).

[88] R. Valizadeh et al. **The preparation of atomically clean metal surfaces for use as photocathodes in normally conducting RF guns**. In *Proc. IPAC 14*, Dresden, Germany, 2014. MOPRI047.

[89] L. Ferreira. **Electropolishing (applied to Copper, Niobium, Titanium)**. EIROforum Science-Business WAMAS Workshop on Advanced Materials and Surfaces.

[90] J. Teichert et al. **Report on Photocathodes**, 2004. CARE Note-2004-033-PHIN.

[91] L. Norgard. **Controlled Heating System**, 1991. BSc thesis at CERN.

[92] I. Martini et al. **Studies of Cs3Sb Cathodes for the CLIC Drive Beam Photoinjector Option**. In *Proc. IPAC 13*, Shanghai, China, 2013. MOPFI058.

[93] P. della Porta et al. **Alkali Metal Generation adn Gas Evolution from Alkali Metal Dispensers**. Technical report, 'SAES Getters, 1968.

[94] L. Schulz. **Sputter-ion pumps**. CERN Accelerator School: Vacuum Technology. DOI:10.5170/CERN-1999-005.37.

[95] N. Chauvin. **Space-Charge Effects**. *CERN Accelerator School Ion Souces*, page 21, 2012.

[96] J. Grames et al. **Ion back-bombardment of GaAs photocathodes inside the DC high voltage electron guns**. In *Proceedings of PAC 2005*, Knoxville, Tennessee, USA, 2005.

[97] R.P. Fliller III et al. **Progress on using NEA cathodes in an RF gun**. In *Proceedings of PAC2005*, Knoxville, Tennessee, USA, 2005.

[98] Y. Luo et al. **PARMELA Simulations of a PWT Photoinjector**. *SLAC-PUB-10084*, July 2003.

BIBLIOGRAPHY

[99] M. Huning. **On using NEA cathodes in an RF gun**. In *Proceedings of EPAC04*, Lucerne, Switzerland, 2004.

[100] R. Barday et al. **Polarized electron source operation at average currents of several milliamperes**. In *AIP Conf. Proc.*, **915**, pages 1019–1024, 2007.

[101] E. Chevallay et al. **Production of a high average current electron beam with Cs-Te photocathodes**. *CTF3 Note 020*, 2001.

[102] O. Mete et al. **PHIN photoinjector as the CLIC drive beam source**. In *Journal of Physics: Conference Series 347*, 2012.

[103] C. Hessler et al. **Recent Development at the High-charge PHIN Photoinjector and the CERN Photoemission Laboratory**. In *Proc. IPAC 14*, Dresden, Germany, 2014. MOPRI042.

[104] T.P. Wangler. *Principles of the RF Linear Accelerators*. John Wiley and Sons,Inc., New York, 1998.

[105] D.Egger. **The Status of the Design of the PHIN Spectrometer Line Diagnostics for the Time Resolved Energy Measurements and First results from 2009**. *CTF3 Note 099*, 2010.

[106] O. Mete. *Study and Experimental Characterization of a Novel Photo Injector for the CLIC Drive Beam*. PhD thesis, EPFL, 2011.

[107] C. Benvenuti et al. **Nonevaporable getter films for ultrahigh vacuum applications**. *J. Vac. Sci. Technol. A*, **16**:148, 1998.

[108] C. Travier. **An introduction to photo-injector design**. *Nucl. Instr. Meth. Phys. Res. A*, **340**(1):26–39, 1994.

[109] A. G.Mathewson. **Vacuum Technical Note: Separation of N_2 and CO in a residual gas spectrum**, 1986. LEP-VA/AM/sm.

[110] J.R.J. Bennett et al. **Outgassing from Stainless Steel and the Effect of the Gauges**. *Vacuum*, **73**:149–153, 2004.

[111] H.F. Dylla et al. **Conditioning of Ion Sources for Mass Spectrometry of Plasmas**. *J. of Vac. Sci. and Tech.*, **A 1**:1297, 1983.

[112] J.H. Han. **Secondary Electron Emission in a Phothocathode RF Gun**. *Phys. Rev. ST Accel. Beams*, **8**(033501), 2005.

[113] J. Li et al. **Emission Studies of Photocathode RF Gun at PITZ**. In *Proceedings of ICAP2012*, Rostock-Warnemnde, Germany, 2012.

[114] J. H. Han et al. **Dark Current and Multipacting in the Photocathode RF guns at PITZ**. In *Proceedings of PAC 2005*, Knoxville, Tennessee, USA, 2005.

[115] C. Hessler et al. **Recent Results on the Performance of Cs_3Sb Photocathodes in the PHIN RF-Gun**. In *Proc. IPAC 15*, Richmond,VA (US), 2015. TUPJE039.

[116] S. Hofmann. *Auger and X-ray Photoelectron Spectroscopy in Materials Science*. Springer, 2013.

[117] B. Feuerbaher et al., editor. *Photoemission and the Electronic Properties of Surfaces*. John Wiley and Sons, 1978.

[118] J. F. Moulder et al. *Handbook of X-ray Photoelectron Spectroscopy*. Physical Electronics, inc, 1995.

[119] I. Martini et al. **X-ray Photoemission Spectroscopy Studies of Cesium Antimonide Photocathodes for Photoinjector Applications**. *Physics Procedia.*, **77**:34–41, 2015.

[120] J. Sangster et al. **The Cs-Sb (Cesium-Antimony) System**. *J. of Phase equilibria*, **4**(18):382–386, 1997.

[121] L. Soriano et al. **Interaction fo cesium-potassium antimonide photocathode materials with oxygen: an x-ray photoelectron spectroscopy study**. *J. Appl. Phys.*, **32**:4737–4744, 1993.

[122] C.W. Bates et al. **X-ray photoemission studies of superficially oxidized cesium antimonide photoemitters**. *Appl. Phys. Lett.*, **38**(5):387–389, 1981.

[123] A. Spitzer et al. **An XPS study of the water adsorption on Cu(110)**. *Surface Science*, **160**:353–361, 1985.

[124] J.H. Linn et al. **An XPS study of the water adsorption/desorption characteristic of transition metal oxide surfaces: microelectronic implications**. *Appl. Surf. Science*, **20**:154–166, 1984.

[125] P. Vishnu Kamath et al. **Electron Spectroscopic Studies of Oxygen and Carbon Dioxide Adsorbed on Metal Surfaces**. *J. Phys. Chem.*, **88**:464–469, 1984.

[126] F. Solymosi. **The Bonding Structure and Reactions of CO_2 Adsorbed on Clean and Promoted Metal Surfaces**. *J. Mol. Catal.*, **65**:337–358, 1991.

[127] I. Martini et al. **Surface Characterization at CERN of Photocathodes for Photoinjector Applications**. In *Proc. IPAC 15*, Richmond,VA (US), 2015. TUPJE040.

[128] S. Lederer et al. **XPS investigation on Cs_2Te photocathodes of FLASH and PITZ**. In *Proc. PAC 09*, Vancouver, (Canada), 2009. MO6RFP054.

[129] C. Hessler et al. **Study of the performance of Cs_2Te cathodes in the PHIN RF photoinjector using long pulse trains**. (Abstract submitted to IPAC16).

[130] S. Lederer et al. **XPS studies of Cs_2Te photocathodes**. In *Proceedings of FEL2007*, Novosibirsk, Russia, 2007.

[131] I. Mills et al., editor. *Quantities, Units and Symbols in Physical Chemistry*. Blackwell Science Ltd, Oxford, 1993. International Union of Pure and Applied Chemistry.

[132] L. Soriano et al. **Oxidation of Cs_2Te with superficial Te clusters studied by XPS**. *Surface Science*, **251/252**:1075–1080, 1991.

[133] L. Soriano et al. **An XPS Study of Cs_2Te Photocathode Materials**. *Surface and Interface Analysis*, **16**:193–198, 1990.

[134] J. Sangster et al. **The Cs-Te (Cesium-Tellurium) System**. *J. of Phase equilibria*, **14**(2):246–249, 1993.

[135] P. Marcin Gach. **Design of a three-deposition setup in the frame of thin film technology for Photoinjector applications (MSc thesis in preparation)**. Cracow University of Technology.

Acknowledgements

First of all I would like to acknowledge Prof. Marco Beghi, for giving me the opportunity of being enrolled in the PhD programme at Politecnico di Milano and for the support he has given throughout these years.
I would like to thank Dr. Christoph Hessler for his supervision during the PhD and for his contribution to the revision of this thesis. My acknowledgements to Dr. Valentin Fedosseev, for the valuable and encouraging discussions, and to Dr. Mikhail Martyanov, for the work he has done on the laser setups.
Je voudrais remercier Eric Chevallay pour le travail qu'il a effectué au laboratoire ainsi que pour sa précieuse aide durant ces trois années.
Moreover, I would like to express my sincere thanks to the CTF3 operators for their prompt troubleshooting (and the useful coffee breaks) during the PHIN runs.
I would like to acknowledge the TE/VSC team for the collaborative work related to the XPS analyses, in particular Holger Neupert and Valentin Nistor, for assistance during the experimental work, and Mauro Taborelli, for valuable discussions.
Moreover, I would like to express my gratitude to the ASTeC/STFC Vacuum Science Group for having welcomed me at Daresbury Laboratory and having allowed the collaborative work.
Further, I would like to acknowledge LA^{3}NET as "*This project has received funding from the European Unions Seventh Framework Programme for research, technological development and demonstration under grant agreement no 289191*".
I am indebted, once again, to Donat Philipp Holzer for reviewing this thesis and supporting me during the writing from far away.
Un doveroso e sentito ringraziamento alla mia famiglia. A mamma, per

avermi insegnato che il duro lavoro paga, a papá, per avermi preparato al mondo. Grazie a Valeria, mia indiscutibile fan fin dagli inizi, e nonna che mi protegge sulla stella piú bella che c'é.
Grazie ad Andrea, che con la sua forza e dolcezza mi supporta quotidianamente sia nella carriera che nella vita.
Un ringraziamento sincero agli amici di sempre, per esserci stati sia nella buona che nella cattiva sorte.
Finally, there are many people I should thank as I can say I have found friends everywhere in these years. I would like to thank the LA^{3}NET fellows, the extremely nice colleagues I met at Daresbury Laboratory, the YCC sailors, Vinx and Gianni for the wonderful trip to NYC, Elena for experiencing together the joys and pains of the PhD student life, the coffee and aperó mates, the "voluntary dinner invitation" group, etc...
Thanks for sharing!